Titre: Title:	Transonic Static Aeroelasticity Using the 2.5D Nonlinear Vortex Lattice Method
Auteur: Author:	Atanas Grozdanov
Date:	2017
Type:	Mémoire ou thèse / Dissertation or Thesis
Référence: Citation:	Grozdanov, A. (2017). Transonic Static Aeroelasticity Using the 2.5D Nonlinear Vortex Lattice Method [Mémoire de maîtrise, École Polytechnique de Montréal]. PolyPublie. https://publications.polymtl.ca/2899/

URL de PolyPublie: PolyPublie URL:	https://publications.polymtl.ca/2899/
Directeurs de recherche: Advisors:	Éric Laurendeau
Programme: Program:	Génie mécanique

UNIVERSITÉ DE MONTRÉAL

TRANSONIC STATIC AEROELASTICITY USING THE 2.5D NONLINEAR VORTEX LATTICE METHOD

ATANAS GROZDANOV
DÉPARTEMENT DE GÉNIE MÉCANIQUE
ÉCOLE POLYTECHNIQUE DE MONTRÉAL

MÉMOIRE PRÉSENTÉ EN VUE DE L'OBTENTION
DU DIPLÔME DE MAÎTRISE ÈS SCIENCES APPLIQUÉES
(GÉNIE MÉCANIQUE)
DÉCEMBRE 2017

UNIVERSITÉ DE MONTRÉAL

ÉCOLE POLYTECHNIQUE DE MONTRÉAL

Ce mémoire intitulé :

TRANSONIC STATIC AEROELASTICITY USING THE 2.5D NONLINEAR VORTEX LATTICE METHOD

présenté par : GROZDANOV Atanas
en vue de l'obtention du diplôme de: Maîtrise ès sciences appliquées
a été dûment accepté par le jury d'examen constitué de :

M. GOSSELIN Frédérick, Doctorat, président
M. LAURENDEAU Éric, Ph. D., membre et directeur de recherche
M. CHITTICK Ian, M.Sc.A., membre

DEDICATION

"Thou shalt not, thou mayest"
To the friends and family I could count on...

ACKNOWLEDGEMENTS

First and foremost, I would like to thank my research supervisor Éric Laurendeau for his guidance during the span of the project and for his timely advice. Throughout my academic journey, his contribution enriched my technical knowledge and I am grateful to him for having given me the chance to work on this passion project.

I also want to send my gratitude to my parents, Ivan and Ludmila, for providing me with support and encouragement during my studies. Their involvement in my projects and my ambitions since an early age taught me to exhibit the perseverance necessary to complete my education.

Finally, I would like to thank the entirety of my laboratory colleagues for their patient help with the technical and psychological challenges I've had to face. Your camaraderie has been more than once essential to my perseverance.

RÉSUMÉ

Ce mémoire traite de l'évaluation aéroélastique d'ailes peu et très flexibles dans le régime subsonique et transsonique.

L'objectif de ce travail est de développer un outil d'aéroélasticité statique pour l'optimisation en phase conceptuelle et préliminaire, capable d'être utilisé en milieu industriel dans lequel les logiciels aérodynamique et de mécanique solide sont en toute probabilité différents. Le grand nombre d'itérations qui doivent être évaluées pour explorer l'espace d'optimisation impose une contrainte de faible coût de calcul.

Pour atteindre cet objectif, une méthode potentielle linéaire *Vortex-Lattice*, combinée avec des données 2.5D RANS à l'aide d'une méthode de couplage alpha modifiée est couplée grâce à une méthode ségrégée avec un modèle d'éléments finis à petites déformations, mais grande déflexions composé de poutres Euler-Bernoulli. Les maillages fluides et solides étant très différents, une méthode d'interpolation conservative est utilisée pour transférer les forces aérodynamiques et les déformations de la structures. Ces transferts d'informations se font de manière consécutive suite aux solutions numériques individuelles du fluide et de la structure. Ce processus est répété itérativement jusqu'à l'atteinte d'une solution convergée.

D'abord, le solveur d'éléments finis développé pour les calculs de structure est décrit. Sa précision est par la suite vérifiée pour des cas géométriquement non linéaires statiques et dynamiques.

En deuxième lieu, la précision du couplage inviscide par méthode ségrégée est vérifiée en comparant les déformations pour le cas subsonique pour des ailes à grand élancement.

En troisième lieu, la précision du couplage visqueux par méthode ségrégée est vérifiée pour le cas subsonique pour des ailes à grand élancement. Cette méthode est par la suite appliquée et validée pour un cas transsonique en comparant avec des solutions 3D RANS numériques publiées précédemment pour le modèle de soufflerie du *Common Research Model*. Les résultats démontrent que la précision est intéressante pour la prédiction des déformations et des distributions de pression, à un coût de calcul approprié pour les phases conceptuelles et préliminaires d'aéronefs.

Finalement, les limites de la méthode et des avenues de recherches sont présentées.

ABSTRACT

This thesis deals with the static aeroelastic evaluation of subsonic and transonic aircraft wings experiencing mild to large deflections.

The objective of the work is to develop a static aeroelastic tool for conceptual and preliminary design optimization, capable of performing this task within an industrial environment where computational solvers are likely to be separate for aerodynamic and structural purposes. The high number of design iterations that are necessary to explore the optimization design space requires that the computational cost of the method be low.

To this end, a linear potential vortex lattice method combined with 2.5D RANS sectional data through a modified alpha coupling method is coupled to a finite element model consisting of linear Euler-Bernoulli beams in a partitioned fashion. There being a significant mismatch between the aerodynamic meshes and the structure meshes, the aeroelastic coupling uses a conservative interpolation method to transfer the aerodynamic forces and structural deflections between fluid and structural solvers. This procedure is repeated iteratively until a converged coupled solution has been obtained.

Firstly, the finite element solver developed for the structural computations is detailed. The accuracy of this solver is subsequently verified for static and dynamic geometrically nonlinear cases.

Secondly, the accuracy of the inviscid partitioned coupling is verified by comparing subsonic deflections for large aspect ratio wings with comparable methods that have previously been published. The results show that the method performs well in predicting the deflections of high aspect ratio wings.

Thirdly, the accuracy of the viscous partitioned coupling is verified for large aspect ratio wings in the subsonic regime. The method is then applied in the transonic flight regime by comparing it with 3D RANS computation results previously published for the Common Research Model wind tunnel model. The results show impressive accuracy in predicting the wing deflections and pressure distributions, at a computational cost that is appropriate for conceptual and preliminary design.

Finally, limitations and possible avenues for research are presented.

TABLE OF CONTENTS

LIST OF TABLES

LIST OF FIGURES

LIST OF ACRONYMS AND ABREVIATIONS

AOA	Angle of Attack
API	Application Programming Interface
C_d	Airfoil Drag Coefficient
C_D	Wing Drag Coefficient
C_l	Airfoil Lift Coefficient
C_L	Wing Lift Coefficient
C_m	Airfoil Pitching Moment Coefficient
C_M	Wing Pitching Moment Coefficient
CFD	Computational Fluid Dynamics
CMDO	Conceptual Multi-Disciplinary Design Optimization
CPS	Conventional Parallel Staggered Procedure
CPU	Central Processing Unit
CRM	Common Research Model
CRM-WT	Common Research Model Wind Tunnel Model
CSS	Conventional Serial Staggered Procedure
DOF	Degree of Freedom
FEM	Finite Element Method
FF	Force Following
GS	Geometric Stiffening
HALE	High-Altitude Long-Endurance
ISS	Improved Serial Staggered Procedure
MDO	Multi-Disciplinary Design Optimization
NL-VLM	Nonlinear Vortex-Lattice Method
NS	Navier-Stokes
PMDO	Preliminary Multi-Disciplinary Design Optimization
RANS	Reynolds Averaged Navier-Stokes
UVLM	Unsteady Vortex-Lattice Method
VLM	Vortex Lattice Method

CHAPTER 1 INTRODUCTION

Following the context of the work, basic concepts and the elements of the problematics are presented to culminate in the research objectives.

1.1 Context

A fundamental practice in engineering is separating the relevant from the irrelevant, which in the early decades of the 20th century meant that aerodynamics and structural analysis were considered separately because the combination of low speeds and highly rigid materials caused small deflections and therefore little interaction between the two (Bisplinghoff *et al.*, 1996). As speeds increased, the interaction of aerodynamic, elastic and inertial forces came to be relevant due to unanticipated structural failures which gave rise to the field of aeroelasticity (figure 1.1), which focused on preventing these static and dynamic aeroelastic phenomena (Collar, 1946). Meanwhile, the aerodynamic properties of the wings were generally designed by assuming a perfectly rigid wing (Fung, 1993).

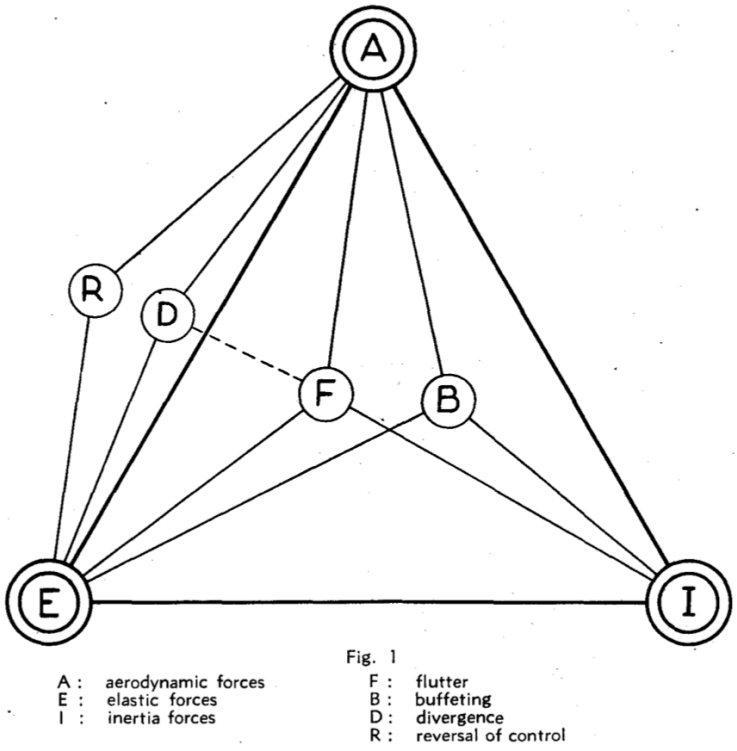

Figure 1.1 The state of aeroelasticity in the 1930s (Source: Collar (1946))

In more recent times, striving to reduce the environmental impact and improve economic performance, aircraft manufacturers have sought to use stronger, yet more flexible materials, which inevitably cause larger lifting surface deflections. This trend has reached very high deflections for recent unconventional aircraft seeking to maximize efficiency for the mission of High-Altitude Long-Endurance (HALE) (Cesnik *et al.*, 2010). With this increase in structural flexibility, the aerodynamic surface that is presented to the airflow in steady flight is altered and influenced by the now significant interaction between elastic forces and aerodynamic forces.

The complexity seen in the sum of all interactions that influence modern aircraft design has been managed by creating three distinct design steps that span the length of an aircraft program : the conceptual, the preliminary and the detailed design phases (Kundu, 2010). Historically, 80% of the life cycle costs of aircraft programs have been incurred because of design decisions made in the conceptual phase. (figure 1.2). These decisions are costly to change once an entire program has passed onto the next design phase and it is therefore desirable to go beyond the traditional use of statistical or low-fidelity computational methods for optimization in the conceptual phase in order to gain greater insight into phenomena that could hinder a program later on (Rizzi, 2011).

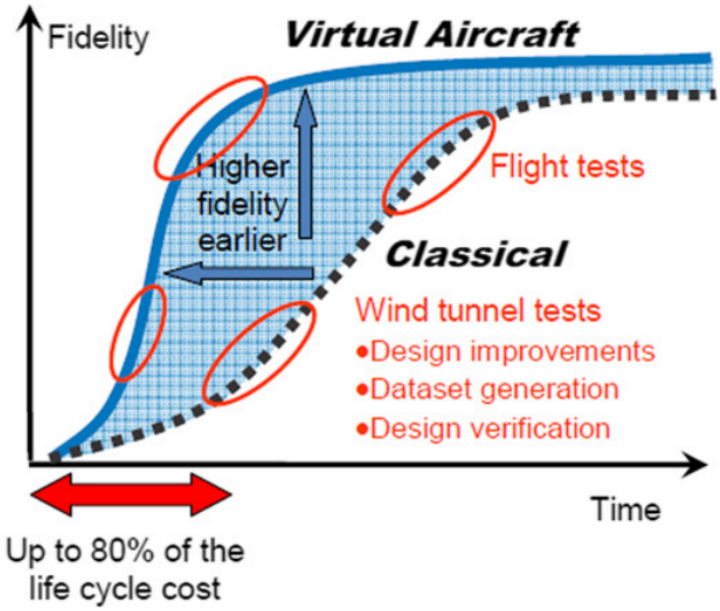

Figure 1.2 Contemporary product development contrasted against Virtual Aircraft approach (Source: Rizzi (2011))

1.2 Basic Concepts

1.2.1 Computational Fluid Dynamics

The mechanics of fluids are governed by three equations describing the conservation of mass, momentum and energy, which are called the Navier-Stokes (NS) equations (Anderson, 2001). This set of equations has no solution for practical problems and it is instead approximated and solved numerically.

Reynolds Averaged Navier-Stokes (RANS)

A practical approximation of the Navier-Stokes equation concerns the exclusive use of average values for the parameters of the flow, thereby disregarding instantaneous fluctuations. This requires the use of a turbulence model to complete the system of equations and provide the Reynolds stress, but reduces the computational cost significantly when compared to direct numerical solution (Versteeg and Malalasekera, 2007).

An established method for solving the RANS equations numerically is the Finite Volume Method (FVM), which requires the discretization of the domain into a mesh of individual cells, within which the obedience of the equations is sought through nonlinear iterative solution algorithms.

Among the methods used to solve the Navier-Stokes equations that are practical for industrial applications, the use of the RANS equations provides the highest fidelity, having the ability to capture detailed flow physics, while being primarily limited by the accuracy and reliability of the turbulence models that are used.

This high-fidelity comes at a significant computational cost and as such, the quality of the solution is dependent on the quality of the mesh generation, the resolution of which is a compromise between precision and computation time. When balancing these two requirements, a two-dimensional solution around an airfoil running on a single CPU requires mere hours, whereas the solution time is measured in days for three-dimensional solutions around a wing (Jameson, 2004). The acceleration of three-dimensional solutions through computational parallelism can reduce the solution time, but remains too costly for optimization.

Linear Potential Flow

By considering the flow as inviscid, incompressible and irrotational, the remaining continuity equation simplifies to become the Laplace equation for velocity potential Φ(Anderson, 2001).

$$\nabla^2\Phi = 0 \tag{1.1}$$

The equation governing the flow is then a linear and elliptic partial differential equation which can easily be solved for elementary singularities of unknown strengths. An arbitrary velocity field can be produced by the superposition of the velocity potentials of a number of such singularities. Linear potential methods such as the Vortex-Lattice Method (VLM) and the doublet-lattice Method (DLM), are able to obtain the flow around complex geometries by distributing singularities over their surface.

Suitable linear combinations of this superposition have to be determined based on the boundary conditions that are established, which for these potential methods is normally a non-penetration boundary condition, requiring the absence of a normal velocity component at the surface of bodies and lifting surfaces. The addition of a Kutta condition is required to obtain a unique solution (Katz and Plotkin, 1991).

The assumptions made in the development of linear potential theory significantly reduce the computational cost of obtaining the flow around an object (Table 1.1), as it simply requires the solution of a linear system obtained from a single equation with a single unknown flow parameter. This advantage is counter-balanced by the methods' inability to capture the flow physics in boundary layers and shock waves, the presence of which is significant in the optimization of the airflow around airfoils and wings.

Table 1.1 Comparison between RANS and Linear Potential (Source: Parenteau (2016))

	RANS	**Linear Potential Methods**
Governing Equations	RANS Equations	Linearized Potential Flow
Viscosity	Yes	No
Compressibility	Yes	No (can use compressibility corrections)
Lift Coefficient	Yes	Yes (with Kutta Condition)
Shockwave Prediction	Yes	No
CPU Time(Jameson, 2004)	Multiple Days	5 sec. - 1 min.

Viscous Potential Methods

In order to overcome the limitations of linear potential methods, they have recently been coupled with sectional viscous data obtained from 2D RANS computations (Van Dam, 2002; Gallay and Laurendeau, 2016). In the study of airflow around aircraft wings, this methodology has demonstrated the ability to capture viscous boundary-layer physics including stall and delivers the three-dimensional pressure field around the wing's actual geometry, rather than its potential discretization surface, which is a flat surface in the case of the VLM.

These methods were initially limited to unswept wings due to the 2D RANS sectional data preventing the capture of three-dimensional effects, but the addition of a periodic source term to account for cross flow in the RANS computations using an infinite swept wing assumption (Bourgault-Côté *et al.*, 2017) has added the capability of capturing these effects to the viscous potential methods (figure 1.3). Furthermore, the pressure distribution around the wing has been found to correlate very well with experimental cases in subsonic and transonic flight regimes (figure 1.4), while retaining the low computational cost of linear potential methods (Gallay and Laurendeau, 2016).

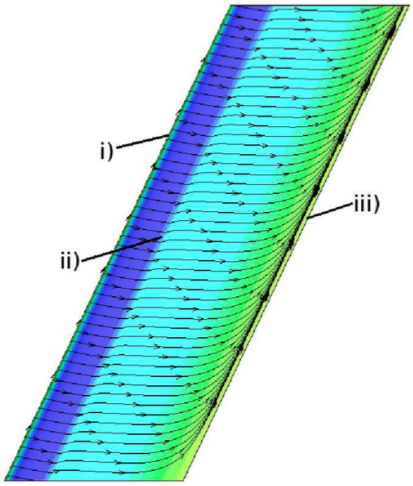

Figure 1.3 Effects captured with the infinite swept wing RANS : i) stagnation line, ii) oblique shock waves, iii) trailing-edge effects (Source: Gallay *et al.* (2014))

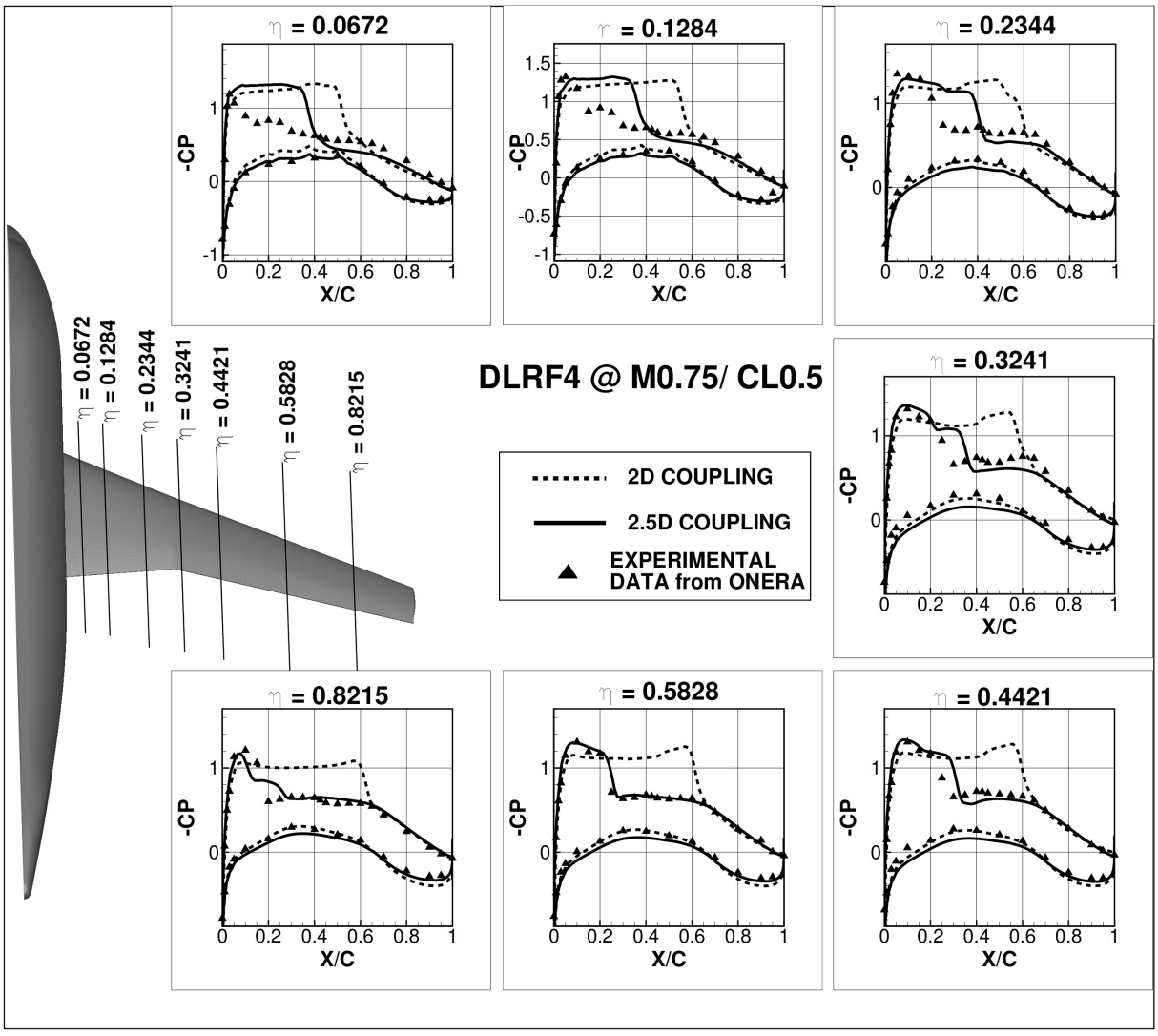

Figure 1.4 Pressure distributions along the nondimensional span η for the DLRF4 at $Mach = 0.75$ and $C_L = 0.5$ (Source: Gallay and Laurendeau (2016))

1.2.2 Computational Structural Analysis

Mechanics of Solids

The materials commonly used in the manufacturing of aeronautical structures are considered to be linearly elastic. These materials therefore obey Hooke's law of elastic deformation that states that the deformation δ that a spring experiences is equal to the force that is applied F over the rigidity k (Hooke, 1678).

$$F = k\delta \tag{1.2}$$

For a linear, homogeneous and isotropic material experiencing axial stresses, Hooke's law expresses the relationship between the strain ϵ_x of the material and its stress σ_x as proportional with the use of constant E named *the modulus of elasticity* or *the Young modulus* (Timoshenko, 1951).

$$\epsilon_x = \frac{\sigma_x}{E} \tag{1.3}$$

The axial stress produces additional strains ϵ_y and ϵ_z along the transverse directions proportionally to the *Young modulus* combined with an additional constant ν named *the Poisson coefficient*.

$$\epsilon_y = -\nu\frac{\sigma_x}{E} \qquad \epsilon_z = -\nu\frac{\sigma_x}{E} \tag{1.4}$$

These relationships can be extended to include stresses and strains along axial and transverse directions.

$$\epsilon_x = \frac{\sigma_x - \nu(\sigma_y + \sigma_z)}{E} \tag{1.5}$$

$$\epsilon_y = \frac{\sigma_y - \nu(\sigma_z + \sigma_x)}{E} \tag{1.6}$$

$$\epsilon_z = \frac{\sigma_z - \nu(\sigma_x + \sigma_y)}{E} \tag{1.7}$$

These equations govern the behavior of linear isotropic materials and their obedience dictates the deformation that an object will undertake when subjected to external forces.

Beam Equations

For a constant section beam that is straight and made of an isotropic material, the deflections can be found analytically and the solutions for combinations of loadings and boundary conditions are listed in common textbooks on the subject (Young and Budynas, 1989).

Finite Element Method

For complex geometries, finding an analytical solution can be difficult or impossible. For this reason, the geometries are approximated, discretized, loaded and solved numerically. The method that has dominated the field of structural mechanics is the Finite Element Method (FEM), which is well documented in multiple texts (Cook *et al.*, 2002; Zienkiewicz and Taylor, 2000). This method uses a discretization containing multiple elements and the different element types can be combined to form structural topologies.

The element topology can greatly affect the computational cost, as well as the precision of the solutions. Moreover, the different element types lend themselves to particular cases and it is understood that fewer higher order elements are required to obtain the same precision in bending as lower order elements (Cook *et al.*, 2002; Zienkiewicz and Taylor, 2000). Analytical solutions to simple topologies are also available as elements which can provide inexpensive precision if the modeling is appropriate for the structural component.

Volumetric Models

When the behavior of a structure is completely unknown, a volumetric FEM model (figure 1.5) can be made of an object that will integrate the stiffness of the object in three dimensions. This method resolves the stress field of the object and thereby provides the appropriate deflections, but will require a high number of elements for the stress field to converge on an appropriately precise solution and is therefore computationally expensive.

Stick Models and Shell Models

When the structural component possesses only one significant dimension, beam elements can be used, forming a stick model (figure 1.6), that will use the well known analytical beam equations instead of integrating the stiffness numerically, providing the stress field implicitly. These elements will provide an exact solution if the loading is only on the beam extremities and they can be used to approximate beams that have curvature and changing sections by refining the discretization.

Similarly, if the structural component possesses only two significant dimensions, analytical models applying to thin shells or plates can be used to account for the transverse direction and remove a dimension of discretization. These elements will provide good precision for in-plane deformation, but may present exaggerated stiffness in out-of-plane bending (Cook *et al.*, 2002).

Aircraft Structures

The need for high rigidity and low weight, as well as structural redundancy, has meant that aircraft structures are primarily built from large planar components (skin, ribs) that are stabilized and supported by beams (spars, stiffeners, uprights). For this reason, aircraft structures that are optimal are limited by stability requirements rather than exclusively by strength requirements. Furthermore, the geometry of the components rarely has a third significant dimension (figure 1.7) and the FEM models that are used to obtain the deformation and internal forces of the structures are based on the combination of beam and shell elements. In the analysis of these structures, the FEM is primarily used to obtain the forces and the deflections, while the stress field and the stability limits of the structure are then determined by additional methods applying to beams and shell structures. (Abdo *et al.*, 2005; DeBlois and Abdo, 2010; Bruhn, 1973; Niu, 1997).

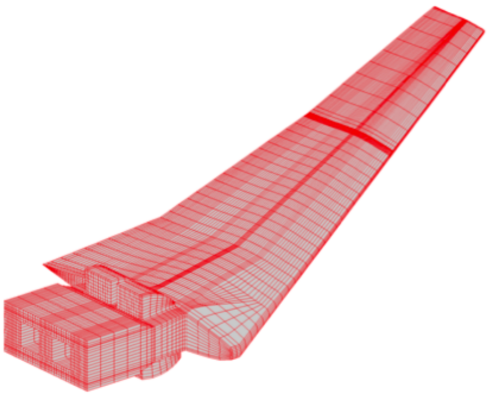

Figure 1.5 Volumetric Model of the Hirenasd Wing (Source: Chwalowski *et al.* (2011))

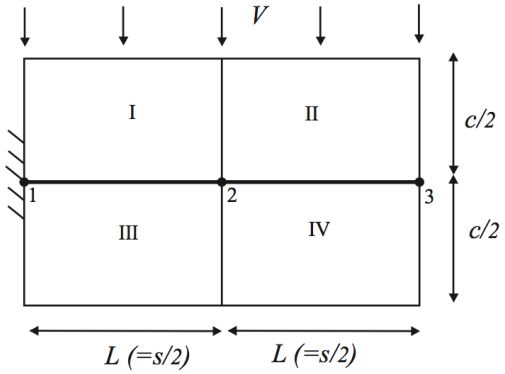

Figure 1.6 Stick Model of two beam elements (Source: Wright and Cooper (2007))

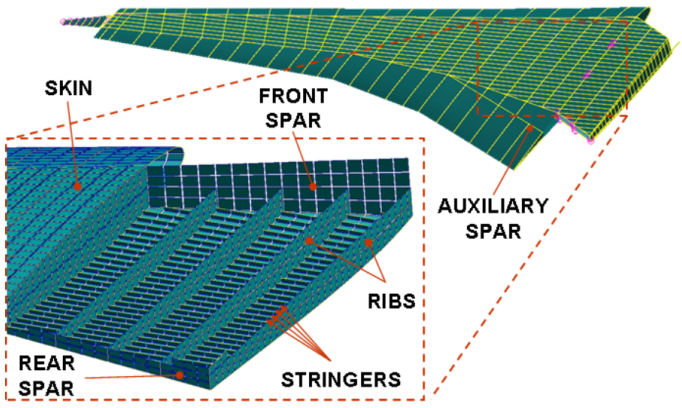

Figure 1.7 Shell Model of a Wing Structure (Source: DeBlois and Abdo (2010))

1.2.3 Computational Static Aeroelasticity of Three-Dimensional Wings

Static aeroelasticity being the interaction between steady flow aerodynamics and solid mechanics, the two systems of equations have to be solved together and the coupling methodology varies, as well as the type of models that are used.

Coupling of Aerodynamic and Structural Computations

A partitioned or segregated coupling algorithm (figure 1.8) uses two independent solvers for the aerodynamics and the structure that will share only the essential boundary conditions, in this case forces and displacements. The benefit of this group of algorithms is the possibility of using existing solvers that are highly specialized and validated for their field. However, iteration is required to balance the forces at the boundary between the two computational domains, which adds to the computational cost. A variety of methods have demonstrated their applicability for both steady and unsteady regimes (Bijl *et al.*, 2006; Farhat and Lesoinne, 2000; Piperno and Farhat, 2001).

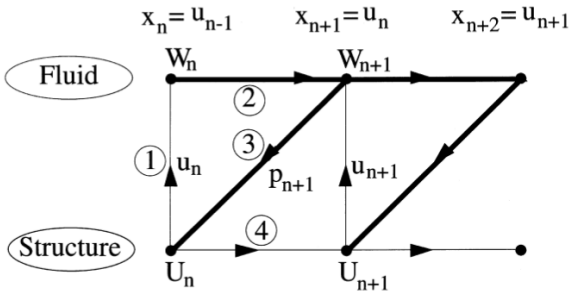

Figure 1.8 Partitioned Coupling Procedure (Source: Farhat and Lesoinne (2000))

A monolithic solution of the aeroelastic solution has to couple the essential, as well as the natural boundary conditions, which implies that fluid and solid stresses be shared as well. This methodology has the benefit that the boundary forces are always balanced and the linear solution is obtained in a single iteration. However, there is significant difficulty in building a monolithic aeroelastic solver and the direct solution of both systems can lead to convergence problems (Hubner *et al.*, 2004; Walhorn and Dinkler, 2005)

1.3 Elements of the Problematics

As mentioned previously, it is desirable to go beyond low-fidelity of aerodynamic tools during the conceptual design phase to enable the decision making and optimization. The VLM coupled with 2.5D RANS has the precision to be applicable to both conceptual design and preliminary design phases and has the capacity to provide a three dimensional pressure distribution. However as shown in figure 1.9, the preliminary design phase replaces stick FEM models with global FEM models, where it is unlikely to be possible to use a monolithic methodology due to the use of established and certified FEM solvers and the inclusion of additional models relevant to design optimization (Abdo *et al.*, 2005; DeBlois and Abdo, 2010; Piperni and Deblois, 2013).

MDO Level	Fidelity	Aerodynamics	Structures	Propulsion
CMDO	L0	Knowledge-based aerodynamics	Knowledge-based weight prediction	Fixed architecture, scaled engine model
	L1	Quasi-3D methods (3D VLM / Panel method + 2D High-Fidelity CFD)	Beam or thin-shell models	Variable architecture, generic rubber engine
	L1.5	Disciplinary L2 Surrogate Models		Surrogate model(s) from Engine supplier(s)
PMDO	L2	Mid-to-High Fidelity CFD (3D TSD to RANS)	Global FEM	Real engine model (fixed)
	L2.5	Disciplinary L3 Surrogate Models		
DMDO	L3	RANS	Detail FEM	

[a]CFD = computational fluid dynamics; 3-D = three-dimensional; 2-D = two-dimensional; VLM = vortex-lattice method; RANS = Reynolds-averaged Navier–Stokes simulation; FEM = finite element method.

Figure 1.9 MDO levels and their use of tools (Source: Piperni and Deblois (2013))

Furthermore, the trend in high-fidelity static aeroelasticity is to go towards 3D RANS coupled with volumetric FEM models (Schuster *et al.*, 2012), which is too computational expensive to allow for the rapid iteration that is necessary for optimization.

Therefore, there is a need for a segregated static aeroelastic methodology that combines low cost higher accuracy aerodynamics with a nonlinear FEM model enabling rapid iteration for conventional wings and for wings having higher flexibility.

1.4 Research Objectives

The goal of this research project is to develop a static aeroelastic tool suitable for the conceptual and preliminary design of aircraft having low or high structural flexibility and operating in both subsonic and transonic flight regimes.

1. Develop an aeroelastic framework that combines the finite element method with the vortex lattice method and assess the accuracy of the finite element solver that is developed.

2. Develop an inviscid segregated static aeroelastic algorithm coupling a vortex lattice method and the nonlinear finite element method, and assess the accuracy of the method in the subsonic regime.

3. Develop a viscous segregated static aeroelastic algorithm coupling 2.5D RANS sectional data with a vortex lattice method and a nonlinear finite element method, and assess the accuracy of the method in the subsonic and transonic regimes.

1.5 Impact

To the best knowledge of the author, this is the first use of the 2.5D NL-VLM method for numerical simulation of aeroelastic phenomena. It was presented at the 2017 IFASD conference (Grozdanov and Laurendeau, 2017).

1.6 Plan of Thesis

This thesis is divided into four portions : a literature review, development of the aeroelastic framework, partitioned use of the VLM in the subsonic regime and the partitioned use of the VLM coupled with the 2.5D RANS sectional data in the transonic regime.

The literature review covers the Vortex Lattice Method, the development of the viscous 2.5D method, the finite element method, as well as partitioned solution algorithms and interpolation schemes. The final section of the literature review explores the different approaches in static aeroelasticity.

The third chapter describes the aeroelastic framework that is developed and then presents a variety of test cases that verify the accuracy of the finite element solver that is developed in steady and unsteady cases of large deflections.

The fourth chapter focuses on the implementation of a partitioned aeroelastic solver combining a vortex lattice method with a nonlinear finite element method. This solver is compared to established solvers to verify the accuracy of the method.

The fifth chapter covers the extension of the partitioned aeroelastic solver into the transonic regime by coupling it with 2.5D RANS sectional data. The results of the method are compared to high-fidelity RANS computations as well as wind-tunnel data to verify the accuracy of the solver.

CHAPTER 2 LITERATURE REVIEW

2.1 Aerodynamic Modeling

2.1.1 Circulation and the Generation of Lift

In the first decade of the previous century, Kutta (1902) and Joukowsky (1910) found that they were able to determine the lift produced by exposing a spinning infinite circular cylinder to a velocity field $\vec{V}$ by relating it to the circulation Γ, defined as the curvilinear integral of the velocity tangential to the segments $\vec{ds}$ along the contour C containing the cylinder.

$$\Gamma = -\oint_C \vec{V} \cdot \vec{ds} \tag{2.1}$$

The expression that they found using potential theory related the lift per unit span L' to the density ρ_∞, the far field velocity U_∞ and the circulation Γ caused by the rotation of the cylinder, this lift force being perpendicular to the far field velocity U_∞ and the cylinder's axis.

$$L' = \rho_\infty U_\infty \Gamma \tag{2.2}$$

2.1.2 Biot-Savart Law

Potential theory focused significantly on electromagnetics in the 19th century and two scientists, Biot and Savart produced the following relationship for the induced current, or velocity $d\vec{V}$ in the of case of aerodynamics, by a straight vortex filament $\vec{dl}$ of strength Γ at a point situated at a radius $\vec{r}$ (DuBois, 1896; Anderson, 2001).

$$d\vec{V} = \frac{\Gamma}{4\pi} \frac{\vec{dl} \times \vec{r}}{|\vec{r}|^3} \tag{2.3}$$

Using this equation, a variety of potential method were developed that computed the lift produced by a wing geometry by finding the potential around the geometry with incompressible inviscid assumptions, including the lifting line method (Prandtl, 1923) for straight planar wings, the Vortex-Lattice Method for thin airfoils and panel methods for bodies and thick airfoils (Katz and Plotkin, 1991).

2.1.3 Vortex Lattice Method

The Vortex-Lattice Method (VLM) as described by Katz and Plotkin (1991) uses a discretization of vortex-rings on the midplane of a wing (figure 2.1). A bound vortex is positioned at the quarter chord of each panel and a non-penetration boundary condition is imposed at the collocation point which is positioned at three quarters of the panel under a small angle of attack assumption.

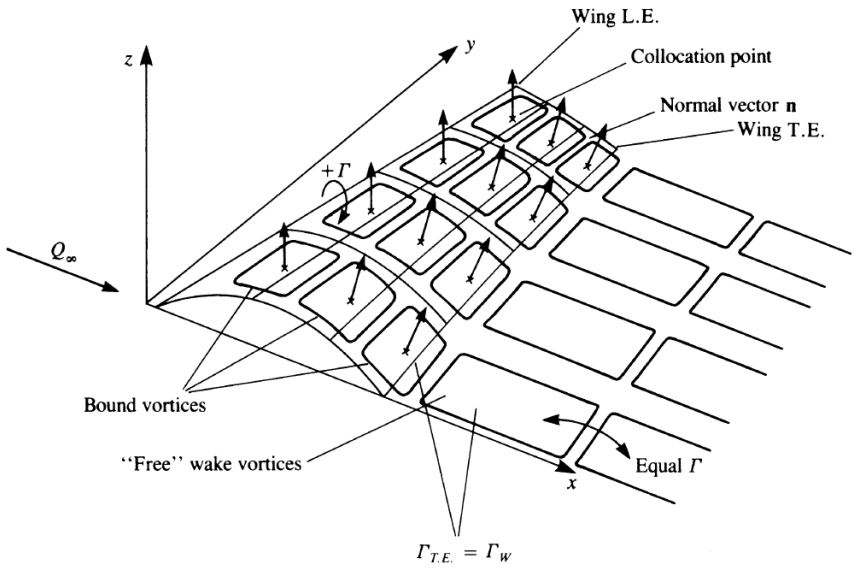

Figure 2.1 Representation of a thin lifting surface with camber (Source: Katz and Plotkin (1991))

All four vortices that form a vortex-ring share the same strength and the induced velocity at any point can be computed with the Biot-Savart law. The influence of each panel on the others is assembled into an influence matrix A that forms the following linear system with the vortex-ring strengths Γ_i as unknowns and the non-penetration boundary condition as a known variable on the right-hand side by the dot product of the far field velocity $\vec{U_\infty}$ and the normal vector of each panel $\vec{n_i}$.

$$\begin{pmatrix} A_{1,1} & A_{1,2} & \cdots & A_{1,m} \\ A_{2,1} & A_{2,2} & \cdots & A_{2,m} \\ \vdots & \vdots & \ddots & \vdots \\ A_{m,1} & A_{m,2} & \cdots & A_{m,m} \end{pmatrix} \begin{pmatrix} \Gamma_1 \\ \Gamma_2 \\ \vdots \\ \Gamma_m \end{pmatrix} = \vec{U_\infty} \cdot \begin{pmatrix} \vec{n_1} \\ \vec{n_2} \\ \vdots \\ \vec{n_m} \end{pmatrix} \tag{2.4}$$

2.1.4 VLM/RANS Coupling

Efforts to extend the applicability of linear potential methods were made by coupling 2D viscous data by way of either the circulation or the angle of attack (α) as a coupling parameter.

Van Dam (2002) developed an α method producing the algorithm that follows, where the effective angle of attack of each section is found by equating the viscous and inviscid lift coefficients (figure 2.2) through an iterative process until the prescribed tolerance ϵ is met.

This algorithm had the inconvenience of causing numeric issues near the stall, where the viscous lift curve slope $Cl_{\alpha v}$ becomes 0, impeding this algorithm because of the presence of this slope in the denominator of the equation used to compute the effective angle of attack.

Algorithm 1 Van Dam α method (Van Dam, 2002)

1: Solve the *Finite Step Method* to calculate $Cl_{inviscid}$
2: **for** Every Span-Wise Section i **do**
3: Compute the section's effective angle of attack α_e, taking into account the wing's angle of attack α_{3D} and the section's angle of attack correction α_{2D}:

$$\alpha_e(i) = \frac{Cl_{inviscid}(i)}{Cl_{\alpha v}} - \alpha_{2D}(i) + \alpha_{3D} \tag{2.5}$$

4: Obtain the viscous lift at the effective angle of attack by interpolating the sectional viscous data:
$\alpha_e(i) \Rightarrow Cl_{visc}(\alpha_e(i))$
5: Obtain the section's angle of attack correction α_{2D}:
$\alpha_{2D}(i) = \alpha_{2D}(i) + \frac{Cl_{visc}(\alpha_e(i)) - Cl_{inviscid}(i)}{Cl_{\alpha v}}$
6: **end for**
7: Repeat Steps 1-6 until $|Cl_{visc} - Cl_{inviscid}| < \epsilon$

Following this development, Gallay and Laurendeau (2014; 2016) modified the method by using the theoretical lift curve slope of 2π instead. They demonstrated that this method has the capacity to capture stall and post-stall for various clean and high-lift configurations of wings in subsonic and transonic regimes. Furthermore, they demonstrated the capacity of this coupling to capture 3D cross-flow effects for swept wings by computing the 2D databases with an infinite swept wing assumption that is detailed by Bourgault-Côté *et al.* (2017), henceforth referred to as 2.5D RANS computations.

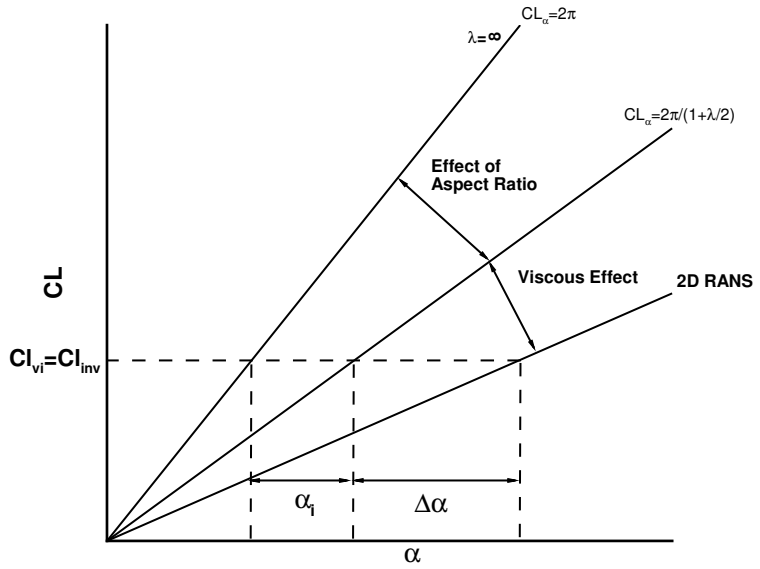

Figure 2.2 Coupling algorithm

Algorithm 2 Van Dam modified α method (Gallay *et al.*, 2014)

1: Solve the VLM to find the $Cl_{inviscid}$ of each section.

2: **for** Every Span-Wise Section i **do**

3: Compute the section's effective angle of attack α_e, taking into account the wing's angle of attack α_{3D} and the section's angle of attack correction α_{2D}:

$$\alpha_e(i) = \frac{Cl_{inviscid}(i)}{2\pi} - \alpha_{2D}(i) + \alpha_{3D}$$

4: Obtain the viscous lift at the effective angle of attack by interpolating the sectional viscous data:
$\alpha_e(i) \Rightarrow Cl_{visc}(\alpha_e(i))$

5: Obtain the section's angle of attack correction α_{2D}:
$\alpha_{2D}(i) = \alpha_{2D}(i) + \frac{Cl_{visc}(\alpha_e(i)) - Cl_{inviscid}(i)}{2\pi}$

6: **end for**

7: Repeat Steps 1-6 until $|Cl_{visc} - Cl_{inviscid}| < \epsilon$

Parenteau (2016) recently found that the coupling method developed by Gallay and Laurendeau (2016) caused variations in the lift curve slope of the computed wings due to the sweep angle (ϕ) being taken into account twice, preventing the sectional data from being independent from sweep considerations.

This involved examination of the effect of sweep in the coupling determined that there was the necessity to express the effective stripwise angle of attack as cosine of the effective angle of attack normal to the sweep line. He then corrected the viscous coupling algorithm to use the stripwise angle of attack instead, which is presented as algorithm 3.

The results obtained using 8 viscous sections demonstrated an impressive ability to obtain the viscous lift, moment and drag curves, as well span loading well into the nonlinear range and even into post-stall, and reinforced the importance of using 2.5D RANS instead of 2D RANS. He further examined which sweeps provided the best correlation with 3D RANS data and found that the best results were obtained by running the 2.5D RANS computations with the quarter-chord sweep of the wing.

Algorithm 3 Coupling algorithm for swept 2.5D RANS CFD data (Parenteau, 2016)

1: Solve the VLM to find the $Cl_{inviscid}$ of each section.
2: **for** Every Span-Wise Section i **do**
3: Compute the section's effective angle of attack α_e, taking into account the wing's angle of attack α_{3D} and the section's angle of attack correction α_{2D}:

$$\alpha_e(i) = \frac{Cl_{inviscid}(i)}{Cl_\alpha} - \alpha_{2D}(i)cos(\phi) + \alpha_{3D} \tag{2.6}$$

4: Obtain the viscous lift at the effective angle of attack by interpolating the sectional viscous data:
$\alpha_e(i) \Rightarrow Cl_{visc}(\alpha_e(i))$
5: Obtain the section's angle of attack correction α_{2D}:
$\alpha_{2D}(i) = \alpha_{2D}(i) + \frac{Cl_{visc}(\alpha_e(i)) - Cl_{inviscid}(i)}{Cl_\alpha}$
6: **end for**
7: Repeat Steps 1-6 until $|Cl_{visc} - Cl_{inviscid}| < \epsilon$

2.2 Structural Modeling

The complexity of aircraft structures implies that their mechanical properties are complex functions of their geometric coordinates and it is impractical or impossible to derive analytical expressions to characterize them (Bisplinghoff *et al.*, 1996).

For this reason, methods such as the finite difference method (Southwell, 1935) and the finite element method have been developed that subdivide the domain of the structure, generating a discretization that provides an approximation for the solution of the governing differential equations. The fidelity of this discrete approximation to the continuous solution is limited by the finite capacity of digital computers (Zienkiewicz and Taylor, 2000).

2.2.1 Finite Element Method

The finite element method was initially introduced informally (Turner, 1956) to approximate the behavior of complex aircraft structures by the discretization of a mechanical continuum into elements of arbitrary triangular or quadrilateral shape, as shown in figure 2.3. It was later formalized as the *Finite Element Method* by Clough (1960) and subsequently underwent development under two separate methodologies, methods of *weighed residuals* (Galerkin, 1915) and the more formal *variational methods* (Courant, 1943).

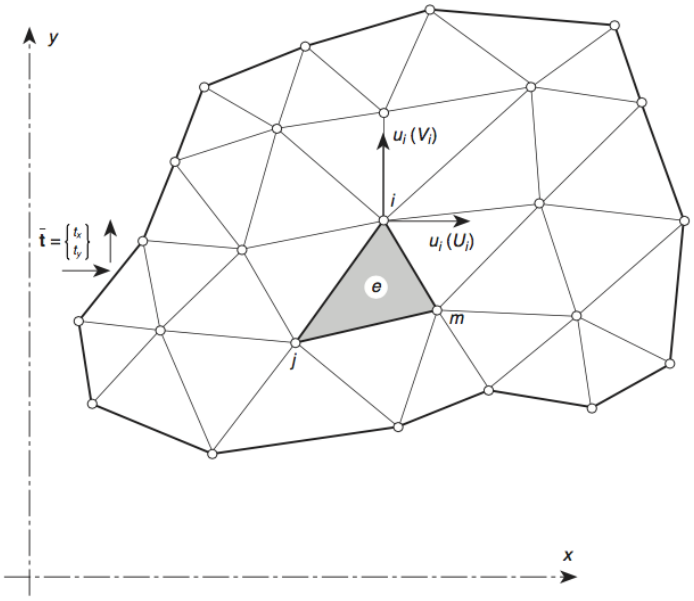

Figure 2.3 A plane stress region divided into finite elements (Source : (Zienkiewicz and Taylor, 2000))

It was later found that when using the Galerkin weighing methodology (Galerkin, 1915), the two methods obtained identical derivations, which completed the establishment of the modern formulation of the method (Prager and Synge, 1947; Zienkiewicz and Cheung, 1964), where it is considered that the finite element method is the application of the Rayleigh-Ritz variational methods (Rayleigh and Spottiswoode, 1871; Ritz, 1909) within domain subdivisions (Zienkiewicz and Taylor, 2000).

Within the context of mechanics of solids, the displacement u in the continuum is approximated by a discrete set of displacements $\vec{\mathbf{u}}$ that are interpolated by shape functions N as follows.

$$u = N\vec{\mathbf{u}} \tag{2.7}$$

The strain ϵ of the continuum is then approximated by a linear operator S,

$$\epsilon = Su \tag{2.8}$$

and the stresses σ obtained by multiplying the strains by a matrix of elastic constants D.

$$\sigma = D\epsilon \tag{2.9}$$

With these variables, the solution by the finite element method within the domain Ω having a boundary Γ_t is obtained by the minimization of the potential energy given by

$$\Pi = \frac{1}{2}\int_{\Omega} \epsilon^{\top} D\epsilon d\Omega - \int_{\Gamma_t} t^{\top} u d\Gamma - \int_{\Omega} b^{\top} u d\Omega \tag{2.10}$$

where t are the traction forces on the boundary and b are the body forces.

This minimization takes the form of the following linear system

$$K_t u = f \tag{2.11}$$

where the tangent stiffness matrix K_t is obtained by the assembly of the element stiffness matrices K_i, defined in equation 2.12, and the applied forces f obtained by the assembly of the forces f_i applied on the elements, as defined in equation 2.13.

$$K = \sum K_i \qquad \text{where} \qquad K_i = \int_{\Omega_i} (SN)^\top D(SN) d\Omega \tag{2.12}$$

$$f = \sum f_i \qquad \text{where} \qquad f_i = \int_{\Omega_i} N^\top b d\Omega + \int_{\Gamma_t^i} N^\top t d\Gamma \tag{2.13}$$

Among the body forces considered, an element mass matrix is defined (equation 2.14) in order to take into account the mass distribution and the contribution of inertia (Cook *et al.*, 2002).

$$M = \int_{\Omega_i} \rho N^\top N d\Omega \tag{2.14}$$

2.2.2 Geometric Nonlinearity

When a structure experiences large deflections over a large enough span, the deformation the material experiences locally can still be considered as small with the nonlinearity appearing because of the rigid body rotation of the element (Reddy, 2014). This assumption is the foundation of the co-rotational formulation (Hsiao *et al.*, 1987; Hsiao and Tsay, 1990; Hsiao, 1992; Hsiao *et al.*, 1999) that obtains a nonlinear solution by considering the material as linear, convecting the position of the nodes and recomputing the tangent stiffness matrix K_t according to the displacements that have accumulated.

In the co-rotational formulation, when the geometric nonlinearity becomes important, the internal forces of each element $\mathbf{F}_i^{int}$ are computed in the element's local convected coordinate system and the total internal forces are assembled, instead of computing them in the global referential system.

2.3 Aeroelastic Coupling

2.3.1 Partitioned Aeroelastic Coupling

The development of partitioned schemes is summarized by Farhat and Lesoinne (2000), where they describe four different coupling schemes in the time domain.

The first is called the *conventional serial staggered procedure* (CSS)(figure 2.4) and consists of serial aerodynamic and structural computations sharing information only once at every time step and is therefore loosely coupled. Furthermore, it was determined that the use of this algorithm reduces the order of the coupled solution to 1 regardless of the order of the two solvers involved.

By repeating the procedure iteratively for every timestep until convergence, a strongly coupled solution can be obtained that preserves the order of the two independent solvers, yet incurs a significant additional computational cost.

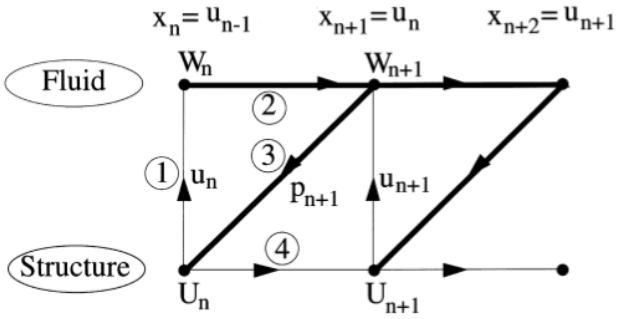

Figure 2.4 Conventional Serial Staggered Procedure (Source : (Farhat and Lesoinne, 2000))

The third method is called the *conventional parallel staggered procedure* (CPS)(figure 2.5) and consists of parallel aerodynamic and structural computations that share boundary conditions at the end of every iteration. This method has the advantage that the two solvers can be run in parallel, but just like the CSS method, reduces the coupled system order to 1.

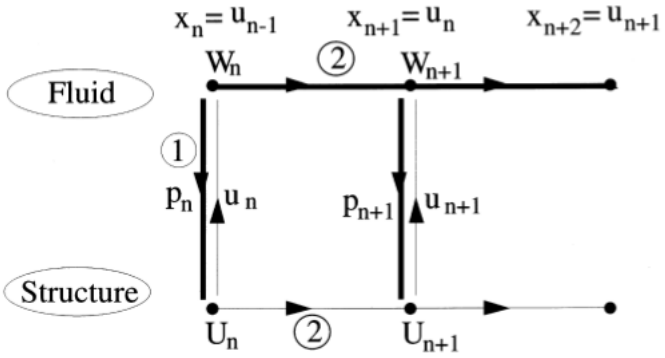

Figure 2.5 Conventional Parallel Staggered Procedure (Source : (Farhat and Lesoinne, 2000))

The fourth and final method introduced is called the *improved serial staggered procedure* (ISS)(figure 2.6) which is in essence a prediction correction scheme that provides the same benefits as strong coupling, but only requires one additional computation per timestep.

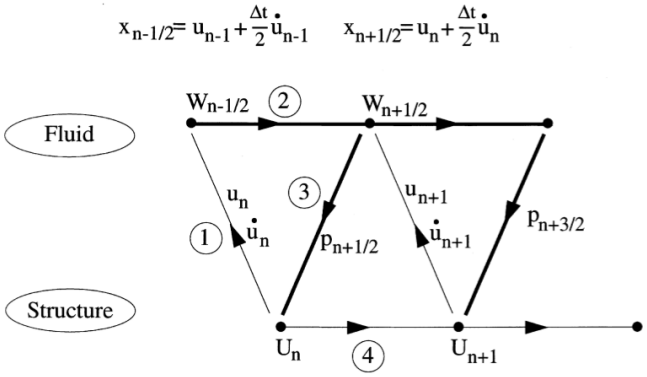

Figure 2.6 Improved Serial Staggered Procedure (Source : (Farhat and Lesoinne, 2000))

Following these initial development of partitioned coupling methods, many authors developed higher order coupling schemes that offer better performance in their range of applications (Van Zuijlen and Bijl, 2005; Bijl *et al.*, 2006) and have demonstrated the usefulness and practicability of adopting the partitioned approach.

2.3.2 Interpolation of Boundary Conditions

The coupling of fluid-structure problems requires that boundary conditions be shared between the two systems. When the fluid and structure have non-matching meshes, projection or interpolation methods are necessary to transfer the information between the two systems, whether they are solved monolithically or in a segregated fashion.

Within an aeroelastic context, Maman and Farhat (1995) developed an algorithm to match fluid and structure boundary conditions by pairing boundary fluid cells to structure cells that were in direct contact and using Gaussian integration in order to interpolate the displacements and forces.

An alternate approach revolves around the use of splines, proposed by Hounjet and Meijer (1995), who specifically favored volume spline interpolation, which extended the use of planar splines in three dimensions and had the advantage of managing non-smooth and non-planar data that was exact at the support points.

Preferring to utilize the topology of finite element structures in order to interpolate fluid data, Farhat *et al.* (1998) offered a conservative approach that utilized the finite element's own shape function to interpolate fluid forces and structural deflections.

A linearized version of this method is presented by De Boer *et al.* (2007), referred to as the intersection method that uses the ratio of overlapping areas to obtain interpolation weights for a pair of fluid and structure cells.

Methodologies that are not dependent on topology have been developed around radial basis functions, summarized by Beckert and Wendland (2001), where data points are each assigned a radial basis function ball, with the interpolation weight decreasing as a function of the distance to the center of the ball. By overlapping the data point balls, each point receives a weighted quantity from the other points based on the radial basis function at the specific distance. By varying the radius, the amount of data points that contribute to the interpolation can be increased and decreased.

The choice of interpolation method was studied by De Boer *et al.* (2006) who demonstrated that the simplest approach which pairs fluid data points with their closest structural points suffered from first order accuracy, while Gaussian integration methods, intersection methods and radial basis methods benefited from second order accuracy, with these methods differing mostly in terms of computational cost. Methods that require a search algorithm in particular are penalized as the number of data points is increased.

2.4 Computational Static Aeroelasticity

2.4.1 Static Subsonic Aeroelasticity

The standard tool to study the subsonic aeroelasticity of wings has been the doublet-lattice method, developed by Albano and Rodden (1969), which provided a linearized formulation based on potential doublets that allows the aeroelastic behavior of the wings to be studied in the frequency domain.

An important assertion was proposed and tested by Van Schoor and von Flotow (1990) stating that the doublet-lattice method could not be used for wings having large aspect ratios due to the significant nonlinearities introduced by the large deflections. This was later reiterated by Patil and Hodges (2004), who found important changes to aeroelastic properties due to geometric nonlinearities in the structural model for high aspect ratio wings, seeing an almost 50% decrease in flutter speeds.

Later on, Drela (1999) created a software application for preliminary aircraft design called ASWING which combined the vortex-lattice method with a nonlinear beam model and provided static and dynamic properties. Shortly thereafter, the use of the unsteady vortex-lattice UVLM method enabled the study of transient time response, which Hall (1999) combined with beam theory to study the active control of an aircraft having a high aspect ratio wing. Similarly, Cattarius (1999) combined the UVLM with beam modeling within the commercial solver ABAQUS to analyze store flutter on a fighter aircraft.

More recently, Wang *et al.* (2006) applied the method to the study of High Altitude Long Endurance aircraft to obtain the dynamic response including structural nonlinearities. This methodology was also applied by Murua *et al.* (2012) when creating and using the unified framework for Simulation of High Aspect Ratio Planes (SHARP) to highlight the importance of including nonlinear structural modeling. Similarly, Mauermann (2010) and Ting *et al.* (2014) studied the transient dynamic response experienced by a flexible aircraft in a wake vortex encounter and the longitudinal trim characteristics of flexible aircraft, respectively.

2.4.2 Transonic Static Aeroelasticity

In order to take into account aerodynamic nonlinearities that appear in transonic flight regime, aeroelastic computations are often coupled with three-dimensional CFD.

By solving the Euler equations with CFD and combining them with a finite element model for the structure, Raveh *et al.* (2000) modeled a transport aircraft undergoing symmetric maneuvers at Mach 0.85 to find static aeroelastic deflections. Farhat *et al.* (2001) studied high-G maneuvers of a fighter aircraft using a Euler CFD solver with a corotational finite element method and his improved serial staggered procedure for time integration, obtaining the transient response to an aggressive 5g pullup maneuver. This methodology was used by Maute *et al.* (2001) in order to conduct sensitivity analysis for the optimization of flexible wings, as well as by Geuzaine *et al.* (2003) to predict the aeroelastic properties of a fighter aircraft at subsonic, transonic and supersonic flight conditions. The application of this procedure to high-aspect ratio wings at transonic flight speeds was pursued by Garcia (2005) using a geometrically nonlinear finite element beam model for static cases, demonstrating that nonlinearities reveal greater susceptibility to static aeroelastic problems.

Recently, the Aeroelastic Prediction Workshop (Schuster *et al.*, 2012) was created in order to further the development of transonic aeroelastic methods and provide experimental data to researchers. A trend that has become obvious in static and dynamic transonic aeroelasticity is the overwhelming use of high-fidelity three-dimensional RANS computations in the time domain (Schuster *et al.*, 2013; Chwalowski *et al.*, 2011; Prananta *et al.*, 2012; Acar and Nikbay, 2013) despite the computational costs associated.

CHAPTER 3 DEVELOPMENT OF AN AEROELASTIC FRAMEWORK

3.1 Framework

The fluid computations of the 2.5D RANS database that is necessary for the NL-VLM method are performed using a mesh generation tool and a FVM solver provided by the research laboratory, called NSGRID and NSCODE respectively.

The NSGRID mesh generation tool (Hasanzadeh *et al.*, 2016) was developed to generate two-dimensional structured meshes around airfoils and can produce multiple blocks that enable parallelization of the solution. It uses smoothing algorithms to maximize orthogonality of the fluid cells, especially at the airfoil surface, which plays an important role in ensuring the quality of the mesh and the ensuing convergence rate, an important factor since the database can easily contain hundreds of solution points.

The FVM Solver, NSCODE (Levesque *et al.*, 2015), is a two-dimensional steady and unsteady aerodynamic solver that operates on 2D structured meshes and is cell-centered. A variety of solution methods are available, such as explicit Runge-Kutta, pointwise implicit and implicit LUSGS. It is capable of using multiple blocks solved in parallel, multigrid acceleration and even chimera meshes. Finally, the solver has an API in python, which facilitates its integration with the VLM and FEM C++ codes developed for this work.

In order to complete the aeroelastic framework, the author developed a finite element solver which is detailed in the remainder of this chapter, as well as the inviscid and viscous coupling procedures detailed in chapters 4 and 5 respectively, and collaborated with Parenteau (2016) in the development of the vortex-lattice method solver.

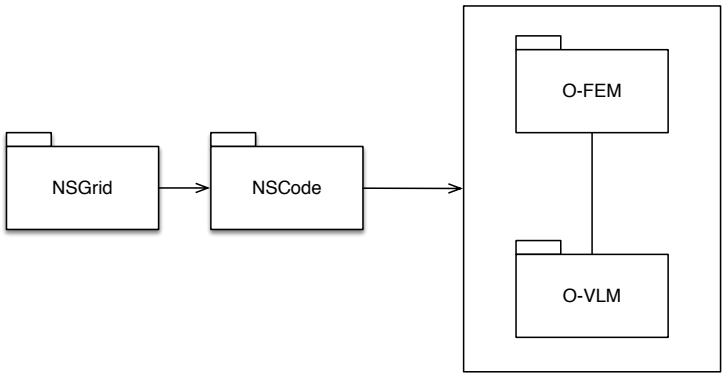

Figure 3.1 Aeroelastic Framework

3.2 Object Oriented Vortex Lattice Method Solver

A dedicated object-oriented vortex-lattice solver (OVLM) was written in the laboratory in C++ with a full API in Python using the *Boost Python Library*. The code is further described and its validation thoroughly performed by Parenteau (2016).

This dedicated VLM was written conjointly with a dedicated object-oriented finite-element solver called Object-Oriented Finite Element Modeler (OFEM) and exposes a variety of geometric modification functions, enabling the transfer of natural or essential boundary conditions with other scripts or the finite element solver.

3.2.1 Object Oriented Finite Element Solver

This solver is implemented as a class library in C++ and exposed in python using the Boost Python C++ library, which is chosen to facilitate interactive scripting, enabling its use in python scripts alongside the other tools that have been developped in the laboratory. A particular advantage of this implementation is that the same instance of the library and any objects that are created persist throughout multiple computations, preventing the use of operating system interrupts (Pacheco, 2011).

The capabilities of the solver are intended to mimic the commercial software Nastran (MSC, 2010), but it provides a full api and access to every component of the solver, including shape functions and jacobians. The elements that are available in OFEM alongside their Nastran equivalents are listed in table 3.1 below and are available for steady and unsteady, linear and nonlinear problems.

Table 3.1 Elements available in OFEM and their equivalents in Nastran

Nastran	OFEM
CROD	Rod
CBEAM, CBAR	Bar
CELAS	Spring
CQUAD4, CSHEAR	Membrane4

3.3 FEM bar element

Euler-Bernoulli bar elements having axial, lateral and rotational degrees of freedom are used throughout this thesis and are well documented in several established textbooks (Cook *et al.*, 2002; Zienkiewicz and Taylor, 2000). As shown in figures 3.2 below, their linear implementation connects two nodes (n_k and n_{k+1}) and offers a force-moment pair ($\vec{\mathbf{F}}_{fem_k}$ and $\vec{\mathbf{M}}_{fem_k}$) at each node with corresponding nodal displacements and nodal rotations.

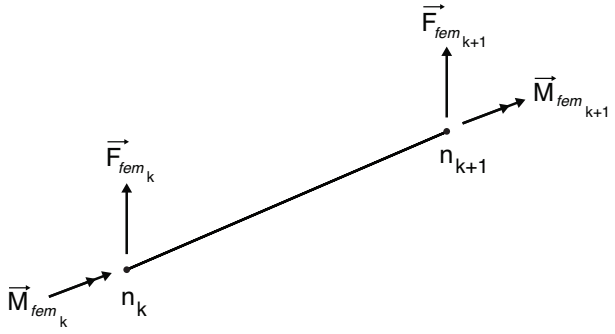

Figure 3.2 Forces applied onto the bar element

As shown in figure 3.3 below, each bar element has a coordinate system with vector axes $\vec{\mathbf{x}}$, $\vec{\mathbf{y}}$ and $\vec{\mathbf{z}}$ that is tied to it's geometric center x_{center_k}. It also has another pair of coordinate systems at each node it connects to. For linear solutions, the three coordinate systems are interchangeable, but this is not the case for nonlinear solutions where the displacements and rotations cause the nodes to be convected.

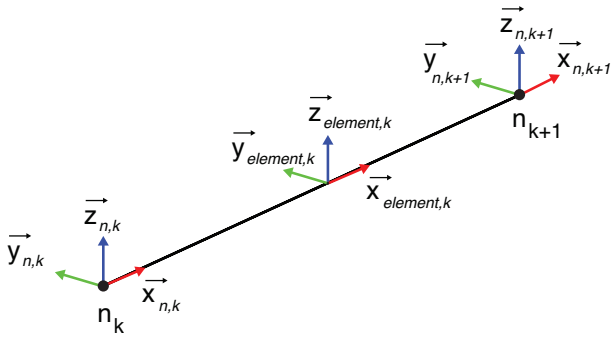

Figure 3.3 Coordinate systems of the bar element

The initial orientation of the element's coordinate systems is provided by an *up* vector which is given at construction by the user or is assumed to be aligned with the z axis if none is given.

3.3.1 Stiffness Matrices

The stiffness matrix of Euler-Bernoulli bars whose material is linear and isotropic can be obtained analytically by the flexibility equations for transverse (u, v, w) and rotational $(\theta_x,\theta_y,\theta_z)$ unit deformations under the assumption of small deformations. This produces the following tangent stiffness matrix K'_t formed by the addition of the stress stiffness matrix K'_σ and geometric stiffness matrix K'_g, all given in the element's local referential (Cook *et al.*, 2002).

$$K'_t = K'_\sigma + K'_g \tag{3.1}$$

$$K'_\sigma = \begin{pmatrix}
\frac{AE}{L} & 0 & 0 & 0 & 0 & 0 & -\frac{AE}{L} & 0 & 0 & 0 & 0 & 0 \\
 & \frac{12EI_z}{L^3} & 0 & 0 & 0 & \frac{6EI_z}{L^2} & 0 & -\frac{12EI_z}{L^3} & 0 & 0 & 0 & \frac{6EI_z}{L^2} \\
 & & \frac{12EI_y}{L^3} & 0 & -\frac{6EI_y}{L^2} & 0 & 0 & 0 & -\frac{12EI_y}{L^3} & 0 & -\frac{6EI_y}{L^2} & 0 \\
 & & & S & 0 & 0 & 0 & 0 & -S & 0 & 0 & 0 \\
 & & & & \frac{2EI_z}{L} & 0 & 0 & 0 & \frac{6EI_y}{L^2} & 0 & \frac{2EI_y}{L} & 0 \\
 & & & & & \frac{4EI_y}{L} & 0 & -\frac{6EI_z}{L^2} & 0 & 0 & 0 & \frac{2EI_z}{L} \\
 & & & & & & \frac{AE}{L} & 0 & 0 & 0 & 0 & 0 \\
 & & & & & & & \frac{12EI_z}{L^3} & 0 & 0 & 0 & -\frac{6EI_z}{L^2} \\
 & & & & & & & & \frac{12EI_y}{L^3} & 0 & \frac{6EI_y}{L^2} & 0 \\
 & & & & & & & & & S & 0 & 0 \\
 & & & & & & & & & & \frac{4EI_y}{L} & 0 \\
 & & & & & & & & & & & \frac{4EI_y}{L}
\end{pmatrix}
\begin{pmatrix} u_1 \\ v_1 \\ w_1 \\ \theta_{x,1} \\ \theta_{y,1} \\ \theta_{z,1} \\ u_2 \\ v_2 \\ w_2 \\ \theta_{x,2} \\ \theta_{y,2} \\ \theta_{z,2} \end{pmatrix}$$

$$K'_g = \frac{P_x}{30L}
\begin{pmatrix}
0 & 0 & 0 & 0 & 0 & 0 & -0 & 0 & 0 & 0 & 0 & 0 \\
 & 36 & 0 & 0 & 0 & 3L & 0 & -36 & 0 & 0 & 0 & 3L \\
 & & 36 & 0 & -3L & 0 & 0 & 0 & -36 & 0 & -3L & 0 \\
 & & & \frac{30J}{A} & 0 & 0 & 0 & 0 & 0 & -\frac{J30}{A} & 0 & 0 \\
 & & & & 4L^2 & 0 & 0 & 0 & 3L & 0 & -L^2 & 0 \\
 & & & & & 4L^2 & 0 & -3L & 0 & 0 & 0 & -L^2 \\
 & & & & & & 0 & 0 & 0 & 0 & 0 & 0 \\
 & & & & & & & 36 & 0 & 0 & 0 & -3L \\
 & & & & & & & & 36 & 0 & 3L & 0 \\
 & & & & & & & & & \frac{30J}{A} & 0 & 0 \\
 & & & & & & & & & & 4L^2 & 0 \\
 & & & & & & & & & & & 4L^2
\end{pmatrix}
\begin{pmatrix} u_1 \\ v_1 \\ w_1 \\ \theta_{x,1} \\ \theta_{y,1} \\ \theta_{z,1} \\ u_2 \\ v_2 \\ w_2 \\ \theta_{x,2} \\ \theta_{y,2} \\ \theta_{z,2} \end{pmatrix}$$

3.3.2 Mass Matrices

For unsteady problems, inertia combines with the stiffness to determine the motion of the structure. A simplification of the mass integration that produces a diagonal matrix is called mass lumping and consists in transferring the mass of the elements to the nodes without taking into account mass distribution or the rotational inertia. The lumped mass matrix M_{Lumped} that is produced is augmented to form the mass matrix $M_{LumpedAugmented}$ for bar elements by adding the rotational inertia of a half bar to the diagonal terms corresponding to rotations (Cook *et al.*, 2002).

$$M_{Lumped} = \begin{pmatrix} \frac{m}{2} & 0 & 0 & 0 & 0 & 0 & 0 & 0 & 0 & 0 & 0 & 0 \\ & \frac{m}{2} & 0 & 0 & 0 & 0 & 0 & 0 & 0 & 0 & 0 & 0 \\ & & \frac{m}{2} & 0 & 0 & 0 & 0 & 0 & 0 & 0 & 0 & 0 \\ & & & J & 0 & 0 & 0 & 0 & 0 & 0 & 0 & 0 \\ & & & & 0 & 0 & 0 & 0 & 0 & 0 & 0 & 0 \\ & & & & & 0 & 0 & 0 & 0 & 0 & 0 & 0 \\ & & & & & & \frac{m}{2} & 0 & 0 & 0 & 0 & 0 \\ & & & & & & & \frac{m}{2} & 0 & 0 & 0 & 0 \\ & & & & & & & & \frac{m}{2} & 0 & 0 & 0 \\ & & & & & & & & & J & 0 & 0 \\ & & & & & & & & & & 0 & 0 \\ & & & & & & & & & & & 0 \end{pmatrix} \begin{pmatrix} u_1 \\ v_1 \\ w_1 \\ \theta_{x,1} \\ \theta_{y,1} \\ \theta_{z,1} \\ u_2 \\ v_2 \\ w_2 \\ \theta_{x,2} \\ \theta_{y,2} \\ \theta_{z,2} \end{pmatrix}$$

$$M_{LumpedAugmented} = \begin{pmatrix} \frac{m}{2} & 0 & 0 & 0 & 0 & 0 & 0 & 0 & 0 & 0 & 0 & 0 \\ & \frac{m}{2} & 0 & 0 & 0 & 0 & 0 & 0 & 0 & 0 & 0 & 0 \\ & & \frac{m}{2} & 0 & 0 & 0 & 0 & 0 & 0 & 0 & 0 & 0 \\ & & & J & 0 & 0 & 0 & 0 & 0 & 0 & 0 & 0 \\ & & & & \frac{ml^2}{24} & 0 & 0 & 0 & 0 & 0 & 0 & 0 \\ & & & & & \frac{ml^2}{24} & 0 & 0 & 0 & 0 & 0 & 0 \\ & & & & & & \frac{m}{2} & 0 & 0 & 0 & 0 & 0 \\ & & & & & & & \frac{m}{2} & 0 & 0 & 0 & 0 \\ & & & & & & & & \frac{m}{2} & 0 & 0 & 0 \\ & & & & & & & & & J & 0 & 0 \\ & & & & & & & & & & \frac{ml^2}{24} & 0 \\ & & & & & & & & & & & \frac{ml^2}{24} \end{pmatrix} \begin{pmatrix} u_1 \\ v_1 \\ w_1 \\ \theta_{x,1} \\ \theta_{y,1} \\ \theta_{z,1} \\ u_2 \\ v_2 \\ w_2 \\ \theta_{x,2} \\ \theta_{y,2} \\ \theta_{z,2} \end{pmatrix}$$

3.4 Finite Elements for Steady Cases

When large rotations occur, a strategy is necessary in order to avoid indeterminate rotations due to the fact that three-dimensional rotations cannot simply be added as vectors (Hsiao *et al.*, 1999; Siemens, 2014).

3.4.1 Quaternions for Large Rotations in Three-Dimensions

The contents of this section are very well summarized by Vince (2011).

If one considers a real in the complex plane, a multiplication by i is equivalent to a rotation of 90 degrees. If one multiplies it by i again, a rotation of 180 degrees has occurred as the real is now negative. A quaternion is simply the extension of this concept to three-dimensional space and is defined by a scalar and three imaginary components

$$q = s + ia + jb + kc \qquad where \qquad s, a, b, c \in \mathbb{R} \tag{3.2}$$

$$i^2 = j^2 = k^2 = ikj = -1 \tag{3.3}$$

and it is common to write a quaternion as a scalar and a vector as follows.

$$q = [s, \vec{\mathbf{v}}]$$

The product of a quaternion is defined as

$$q_a q_b = [s_a, \vec{\mathbf{a}}][s_b, \vec{\mathbf{b}}] = [s_a s_b - \vec{\mathbf{a}} \cdot \vec{\mathbf{b}}, s_a \vec{\mathbf{b}} + s_b \vec{\mathbf{a}} + \vec{\mathbf{a}} \times \vec{\mathbf{b}}] \tag{3.4}$$

, the conjugate is defined as

$$q^* = [s, -\vec{\mathbf{b}}] \tag{3.5}$$

and the inverse as

$$q^{-1} = \frac{q^*}{|q|^2} \tag{3.6}$$

where $|q| = \sqrt{s^2 + \vec{\mathbf{v}}^2}$ is the norm of the quaternion.

The quaternion that represents a rotation of $\boldsymbol{\theta}$ about an axis $\vec{\boldsymbol{v}}$ is given by

$$\mathring{q}_{rot} = [cos\frac{1}{2}\theta, sin\frac{1}{2}\theta\vec{\boldsymbol{v}}] \tag{3.7}$$

and its associated rotation matrix to rotate a point is given by the following matrix.

$$R(\mathring{q}_{rot}) = \begin{pmatrix} 1-2(y^2+z^2) & 2(xy-sz) & 2(xz+sy) \\ 2(xy+sz) & 1-2(x^2+z^2) & 2(yz-sx) \\ 2(xz-sy) & 2(yz+sx) & 1-2(x^2+y^2) \end{pmatrix} \tag{3.8}$$

Multiple rotations can be added together by the quaternion product as follows

$$\mathring{q}_3 = \mathring{q}_2 \cdot \mathring{q}_1, \tag{3.9}$$

and the inverse of a rotation quaternion will perform the opposite rotation. Futhermore, rotations can be interpolated by a ratio t as follows

$$\mathring{q} = \mathring{q}_1 \frac{sin(1-t)\theta}{sin\theta} + \mathring{q}_2 \frac{sint\theta}{sin\theta} \qquad \text{where} \qquad \theta = \frac{\mathring{q}_1 \cdot \mathring{q}_2}{|\mathring{q}_1||\mathring{q}_2|} \tag{3.10}$$

Finally, a rotation quaternion can be obtained from euler rotations r_x, r_y and r_z about the x, y and z axes by using the following equations

$$s = cos(\frac{r_z}{2})cos(\frac{r_y}{2})cos(\frac{r_x}{2}) + sin(\frac{r_z}{2})sin(\frac{r_y}{2})sin(\frac{r_x}{2}) \tag{3.11}$$

$$\boldsymbol{v}_x = cos(\frac{r_z}{2})cos(\frac{r_y}{2})sin(\frac{r_x}{2}) - sin(\frac{r_z}{2})sin(\frac{r_y}{2})cos(\frac{r_x}{2}) \tag{3.12}$$

$$\boldsymbol{v}_y = cos(\frac{r_z}{2})sin(\frac{r_y}{2})cos(\frac{r_x}{2}) + sin(\frac{r_z}{2})cos(\frac{r_y}{2})sin(\frac{r_x}{2}) \tag{3.13}$$

$$\boldsymbol{v}_z = sin(\frac{r_z}{2})cos(\frac{r_y}{2})cos(\frac{r_x}{2}) - cos(\frac{r_z}{2})sin(\frac{r_y}{2})sin(\frac{r_x}{2}) \tag{3.14}$$

$$\Delta q = [s, \boldsymbol{v_x}, \boldsymbol{v_y}, \boldsymbol{v_z}] = [s, \vec{\boldsymbol{v}}] \tag{3.15}$$

and in turn, euler angles r_x, r_y and r_z can be obtained from quaternions as follows

$$r_x = atan(2sa + 2bc, 1 - 2(a^2 + b^2)) \tag{3.16}$$

$$r_y = asin(2sb - 2ca) \tag{3.17}$$

$$r_z = atan(2sc + 2ab, 1 - 2(b^2 + c^2)) \tag{3.18}$$

3.4.2 Internal Forces with Quaternions

As shown in figure 3.4, in order to enable the use of quaternions in the finite element method, every node is given a quaternion tracking its rotation in space ($\overset{\circlearrowleft}{q}_{n,k}$ and $\overset{\circlearrowleft}{q}_{n,k+1}$), every element is given a quaternion at its center ($\overset{\circlearrowleft}{q}_{e}$) to track its rotation and every element also receives supplementary quaternions for each of its nodes ($\overset{\circlearrowleft}{q}_{e,k}$ and $\overset{\circlearrowleft}{q}_{e,k+1}$), as they will include both the nodal quaternion rotation and the element's initial orientation quaternion.

The distinction is necessary because upon construction, each node is assumed unrotated

$$\overset{\circlearrowleft}{q}_{n,k} = [1, \vec{\mathbf{0}}]$$

while the element's nodal quaternions include the element's initial rotation

$$\overset{\circlearrowleft}{q}_{e,k} = \overset{\circlearrowleft}{q}_{e}$$
$$\overset{\circlearrowleft}{q}_{e,k+1} = \overset{\circlearrowleft}{q}_{e}$$

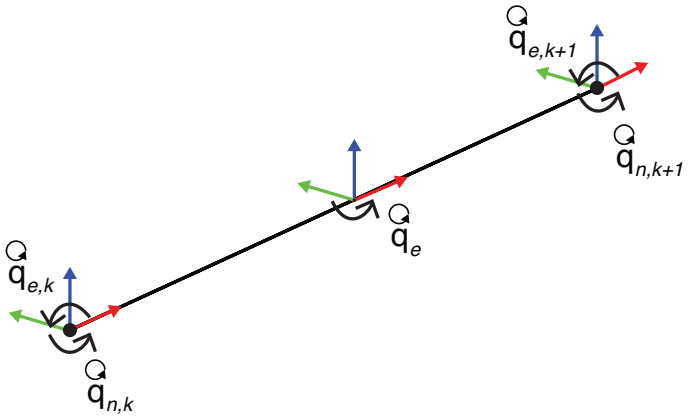

Figure 3.4 Forces to be applied onto the FEM for each column of vortex rings

In order to compute internal forces with the corotational formulation, it is necessary to remove rigid body rotations and to find the deflection of the element with respect to its convected frame of reference.

Internal forces at element tip node

The internal forces are found by considering that, with respect to its convected state, only the second node of the element has experienced a displacement and a rotation as shown in the local referential in figure 3.5 and in the global referential in figure 3.6.

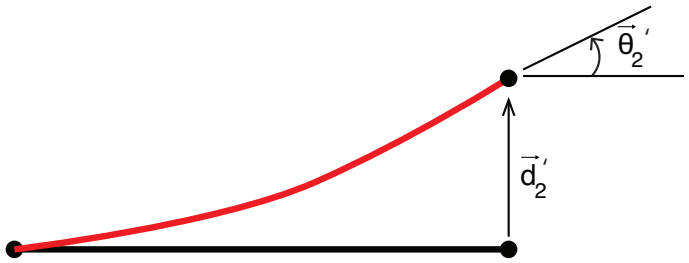

Figure 3.5 Element deformations with tip node approach in the local referential

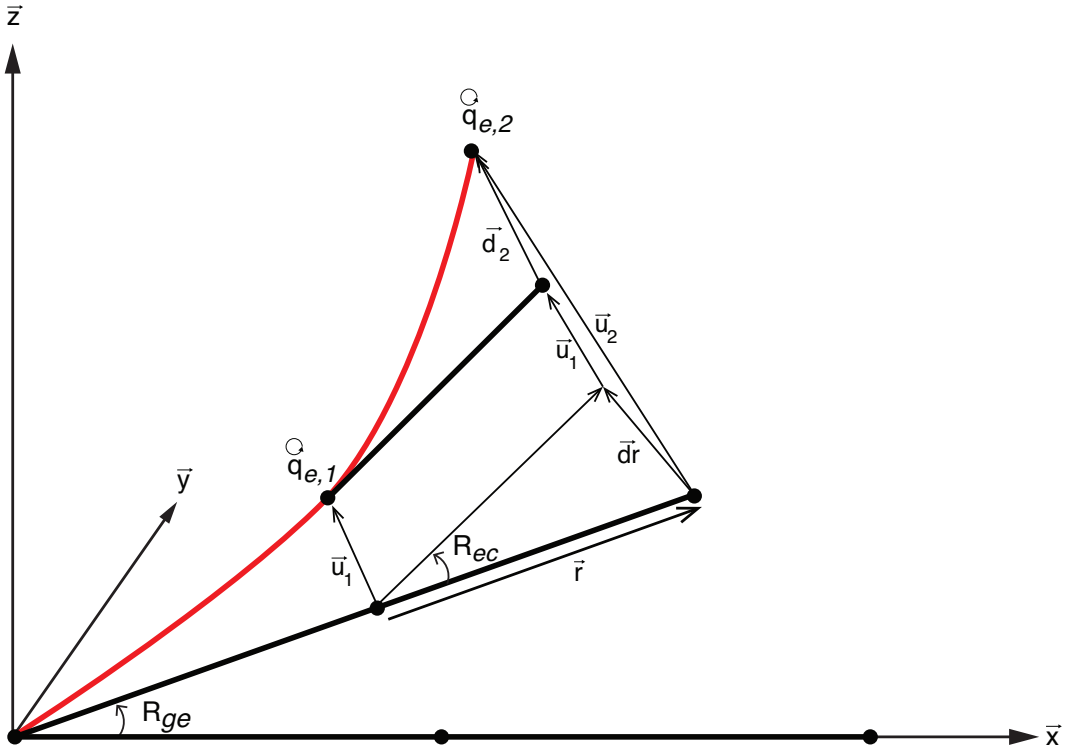

Figure 3.6 Element deformations with tip node approach in the global referential

Starting with an initial solution of the problem, the steps to follow within each element to obtain the internal forces with respect to the tip node are as follows.

1. Obtain the global nodal displacements and rotations $\vec{\mathbf{u}}_1, \vec{\mathbf{u}}_2, \vec{\theta}_1, \vec{\theta}_2$

2. Obtain the rotation matrices necessary to go from global referential to element referential and convected element referential

$$\begin{aligned}
\mathbf{R_{gc}} &= R(\overset{\circlearrowleft}{q}_{1,k} \cdot \overset{\circlearrowleft}{q}_e) \\
\mathbf{R_{cg}} &= R_{cg}^{\top} \\
\mathbf{R_{ec}} &= R(\overset{\circlearrowleft}{q}_{1,k}) \\
\mathbf{R_{ce}} &= R_{ce}^{\top} \\
\mathbf{R_{ge}} &= R(\overset{\circlearrowleft}{q}_e) \\
\mathbf{R_{eg}} &= R_{ge}^{\top}
\end{aligned}$$

3. Find the rotation of the nodes in the element's local convected referential by removing the element rotation from the global nodal rotation quaternions

$$\begin{aligned}
\overset{\circlearrowleft}{q'}_{1,k} &= \overset{\circlearrowleft}{q}_e^{-1} \cdot \overset{\circlearrowleft}{q}_{1,k} \cdot \overset{\circlearrowleft}{q}_e \\
\overset{\circlearrowleft}{q'}_{2,k} &= \overset{\circlearrowleft}{q}_e^{-1} \cdot \overset{\circlearrowleft}{q}_{2,k} \cdot \overset{\circlearrowleft}{q}_e
\end{aligned}$$

4. Find the difference between them, which is the rotational displacement in the element's local referential

$$\overset{\circlearrowleft}{q'}_{rot} = \overset{\circlearrowleft}{q'}_{1,k}^{-1} \cdot \overset{\circlearrowleft}{q'}_{2,k}$$

5. Determine the rotation of node 2 assuming small deformations

$$\begin{aligned}
s &= \overset{\circlearrowleft}{q'}_{rot}.s \\
a &= \overset{\circlearrowleft}{q'}_{rot}.a \\
b &= \overset{\circlearrowleft}{q'}_{rot}.b \\
c &= \overset{\circlearrowleft}{q'}_{rot}.c \\
\vec{\theta}'_2 &= \{atan(2sa + 2bc, 1 - 2(a^2 + b^2)), asin(2sb - 2ca), atan(2sc + 2ab, 1 - 2(b^2 + c^2))\}
\end{aligned}$$

6. Find the displacement of node 2 caused by the rigid body rotation at node 1

$$\vec{\mathbf{r}} = \vec{\mathbf{n}}_{k+1} - \vec{\mathbf{n}}_k$$
$$\vec{\mathbf{dr}} = \mathbf{R_{ec}}\vec{\mathbf{r}} - \vec{\mathbf{r}}$$

7. Find the displacement of node 2 in the convected element's local referential

$$d'_2 = \mathbf{R_{cg}}(\vec{\mathbf{u}}_2 - \vec{\mathbf{u}}_1 - \vec{\mathbf{dr}})$$

8. Find the local forces and moments using the element's stiffness matrix obtained at the tip node

$$\begin{pmatrix} \vec{\mathbf{f}}'_1 \\ \vec{\mathbf{m}}'_1 \\ \vec{\mathbf{f}}'_2 \\ \vec{\mathbf{m}}'_2 \end{pmatrix} = K' \begin{pmatrix} \vec{0} \\ \vec{0} \\ d'_2 \\ \vec{\theta}'_2 \end{pmatrix}$$

9. Rotate the loads to the global referential

$$\vec{\mathbf{f}_1} = \mathbf{R_{gc}}\vec{\mathbf{f}'_1}$$
$$\vec{\mathbf{m}_1} = \mathbf{R_{gc}}\vec{\mathbf{m}'_1}$$
$$\vec{\mathbf{f}_2} = \mathbf{R_{gc}}\vec{\mathbf{f}'_2}$$
$$\vec{\mathbf{m}_2} = \mathbf{R_{gc}}\vec{\mathbf{m}'_2}$$

Internal forces at element center

In contrast to the previous method, the internal forces are found by considering that, with respect to its convected state, both the first and second nodes of the element have experienced a displacement and a rotation as shown in the local referential in figure 3.7 and in the global referential in figure 3.8.

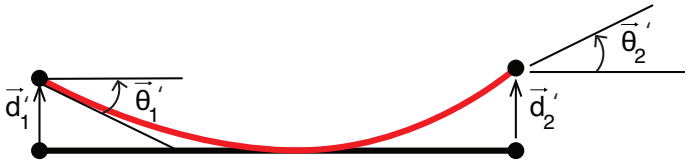

Figure 3.7 Element deformations with element center approach in the local referential

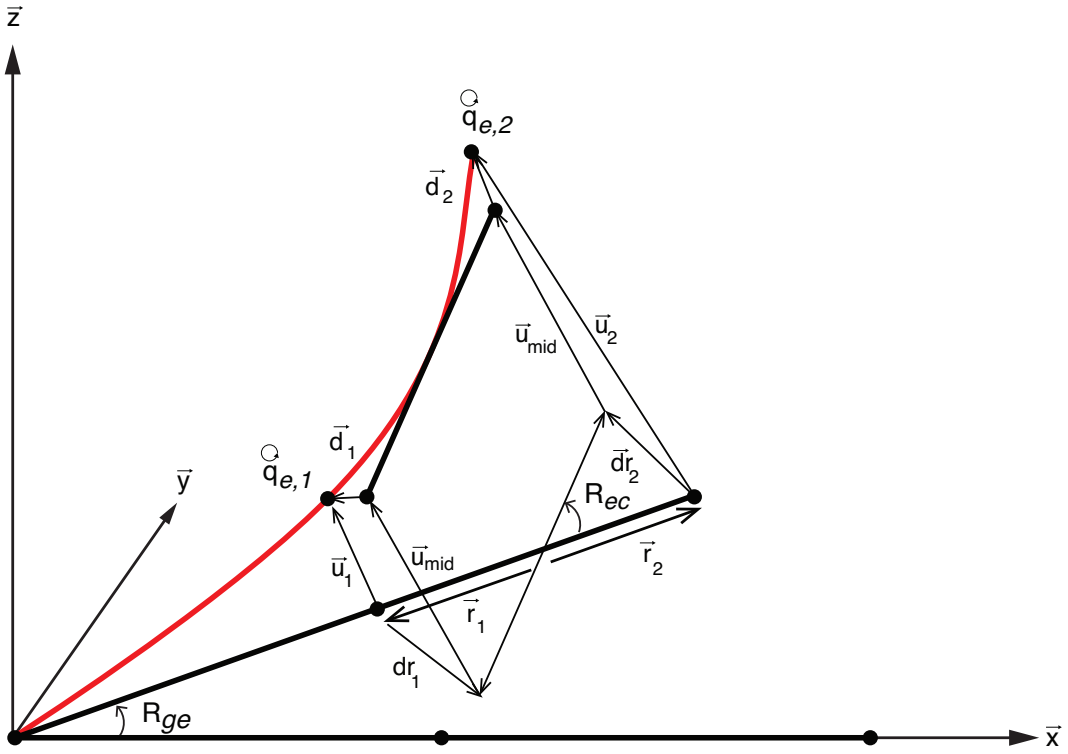

Figure 3.8 Element deformations with element center approach in the global referential

Starting with an initial solution of the problem, the steps to follow within each element to obtain the internal forces with respect to the element center are as follows.

1. Obtain the global nodal displacements and rotations $\vec{\mathbf{u}}_1, \vec{\mathbf{u}}_2, \vec{\theta}_1, \vec{\theta}_2$

2. Find the average of the displacements to obtain the displacement of the element's center

$$\vec{\mathbf{u}}_{mid} = (\vec{\mathbf{u}}_1 + \vec{\mathbf{u}}_2)/2$$

3. Obtain the average of the nodal rotation quaternions using equation 3.10 to obtain the rotation quaternion of the element's center

$$\overset{\circlearrowleft}{q}_{mid} = \overset{\circlearrowleft}{q}_{1,k} \frac{sin(1-0.5)\theta}{sin\theta} + \overset{\circlearrowleft}{q}_{2,k} \frac{sin0.5\theta}{sin\theta} \qquad \text{where} \qquad \theta = \frac{\overset{\circlearrowleft}{q}_{1,k} \cdot \overset{\circlearrowleft}{q}_{2,k}}{|\overset{\circlearrowleft}{q}_{1,k}||\overset{\circlearrowleft}{q}_{2,k}|}$$

4. Obtain the rotation matrices necessary to go from global referential to element referential and convected element referential

$$\begin{aligned}
\mathbf{R_{gc}} &= R(\overset{\circlearrowleft}{q}_{1,k} \cdot \overset{\circlearrowleft}{q}_e) \\
\mathbf{R_{cg}} &= R_{cg}^{\top} \\
\mathbf{R_{ec}} &= R(\overset{\circlearrowleft}{q}_{mid}) \\
\mathbf{R_{ce}} &= R_{ce}^{\top} \\
\mathbf{R_{ge}} &= R(\overset{\circlearrowleft}{q}_e) \\
\mathbf{R_{eg}} &= R_{ge}^{\top}
\end{aligned}$$

5. Find the rotation of the nodes in the element's local convected referential by removing the element rotation from the global nodal rotation quaternions

$$\begin{aligned}
\overset{\circlearrowleft}{q'}_{1,k} &= \overset{\circlearrowleft}{q}_e^{-1} \cdot \overset{\circlearrowleft}{q}_{1,k} \cdot \overset{\circlearrowleft}{q}_e \\
\overset{\circlearrowleft}{q'}_{2,k} &= \overset{\circlearrowleft}{q}_e^{-1} \cdot \overset{\circlearrowleft}{q}_{2,k} \cdot \overset{\circlearrowleft}{q}_e
\end{aligned}$$

6. Find the rotation of node 1 and node 2 in the element's local referential

$$\begin{aligned}
\overset{\circlearrowleft}{q'}_{rot,1} &= \overset{\circlearrowleft}{q}_{mid}^{-1} \cdot \overset{\circlearrowleft}{q'}_{1,k} \\
\overset{\circlearrowleft}{q'}_{rot,2} &= \overset{\circlearrowleft}{q}_{mid}^{-1} \cdot \overset{\circlearrowleft}{q'}_{2,k}
\end{aligned}$$

7. Determine the rotation of node 1 assuming small deformations

$$
\begin{aligned}
s &= \overset{\circlearrowleft}{q'}_{rot,1}.s \\
a &= \overset{\circlearrowleft}{q'}_{rot,1}.a \\
b &= \overset{\circlearrowleft}{q'}_{rot,1}.b \\
c &= \overset{\circlearrowleft}{q'}_{rot,1}.c \\
\vec{\theta'_1} &= \{atan(2sa+2bc, 1-2(a^2+b^2)), asin(2sb-2ca), atan(2sc+2ab, 1-2(b^2+c^2))\}
\end{aligned}
$$

8. Determine the rotation of node 2 assuming small deformations

$$
\begin{aligned}
s &= \overset{\circlearrowleft}{q'}_{rot,2}.s \\
a &= \overset{\circlearrowleft}{q'}_{rot,2}.a \\
b &= \overset{\circlearrowleft}{q'}_{rot,2}.b \\
c &= \overset{\circlearrowleft}{q'}_{rot,2}.c \\
\vec{\theta'_2} &= \{atan(2sa+2bc, 1-2(a^2+b^2)), asin(2sb-2ca), atan(2sc+2ab, 1-2(b^2+c^2))\}
\end{aligned}
$$

9. Find the displacement of node 1 caused by the rotation of the beam

$$
\begin{aligned}
\vec{\mathbf{r_1}} &= \vec{\mathbf{n}}_k - \vec{\mathbf{x}}_{center_k} \\
\vec{\mathbf{dr_1}} &= \mathbf{R_{ec}}\vec{\mathbf{r_1}} - \vec{\mathbf{r_1}}
\end{aligned}
$$

10. Find the displacement of node 2 caused by the rotation of the beam

$$
\begin{aligned}
\vec{\mathbf{r_2}} &= \vec{\mathbf{n}}_{k+1} - \vec{\mathbf{x}}_{center_k} \\
\vec{\mathbf{dr_2}} &= \mathbf{R_{ec}}\vec{\mathbf{r_2}} - \vec{\mathbf{r_2}}
\end{aligned}
$$

11. Find the displacement of node 1 and 2 in the convected element's local referential

$$
\begin{aligned}
d'_1 &= \mathbf{R_{cg}}(\vec{\mathbf{u}}_1 - \vec{\mathbf{u}}_{mid} - \vec{\mathbf{dr_1}}) \\
d'_2 &= \mathbf{R_{cg}}(\vec{\mathbf{u}}_2 - \vec{\mathbf{u}}_{mid} - \vec{\mathbf{dr_2}})
\end{aligned}
$$

12. Find the local forces and moments using the element's stiffness matrix obtained at center of the element

$$\begin{pmatrix} \vec{\mathbf{f}}_{\mathbf{1}}' \\ \vec{\mathbf{m}}_{\mathbf{1}}' \\ \vec{\mathbf{f}}_{\mathbf{2}}' \\ \vec{\mathbf{m}}_{\mathbf{2}}' \end{pmatrix} = K' \begin{pmatrix} d_1' \\ \vec{\theta}_1' \\ d_2' \\ \vec{\theta}_2' \end{pmatrix}$$

13. Rotate the loads to the global referential

$$\begin{aligned} \vec{\mathbf{f}}_{\mathbf{1}} &= \mathbf{R_{gc}} \vec{\mathbf{f}}_{\mathbf{1}}' \\ \vec{\mathbf{m}}_{\mathbf{1}} &= \mathbf{R_{gc}} \vec{\mathbf{m}}_{\mathbf{1}}' \\ \vec{\mathbf{f}}_{\mathbf{2}} &= \mathbf{R_{gc}} \vec{\mathbf{f}}_{\mathbf{2}}' \\ \vec{\mathbf{m}}_{\mathbf{2}} &= \mathbf{R_{gc}} \vec{\mathbf{m}}_{\mathbf{2}}' \end{aligned}$$

3.4.3 Assembly

Both the steady and unsteady solutions of the finite element solver require the assembly of global system matrices, consisting of the global tangential stiffness matrix $[K_t]$ and the mass matrix $[M]$ of the global system. Furthermore, the internal forces also have to be combined into a global internal force vector $\{\vec{F}^{int}\}$.

This operation is repeated for every iteration of the Newton-Raphson method, can be repeated for every iteration of the Explicit and Newmark direct integration methods and is detailed in algorithm 4.

Algorithm 4 Finite Element Solver System Assembly

1: Clear the global system matrices and vectors ($[K_t]$,$[M]$ and $\{\vec{F}^{int}\}$)
2: **for** every finite element i **do**
3: Obtain the stiffness matrix in the element's referential $K'_{t,i}$
4: Obtain the mass matrix in the element's referential M'_i
5: Obtain the rotation matrix $\mathbf{R_{ge,i}}$ associated with the element's orientation in space with respect to the global referential based on the rotation of the center of the element or the tip of the element, depending on which method is used to obtain the internal forces.
6: Obtain the transformation matrix P for the element

$$\mathbf{P} = \begin{pmatrix} \mathbf{R}_{ge,i} & & & \\ & \mathbf{R}_{ge,i} & & \\ & & \mathbf{R}_{ge,i} & \\ & & & \mathbf{R}_{ge,i} \end{pmatrix}$$

7: Add the transformed matrices to the global matrices

$$[K_t] \Leftarrow P^\top K'_{t,i} P$$
$$[M] \Leftarrow P^\top M'_i P$$

8: Add the element's nodal internal forces to the global internal forces vector

$$\{\vec{F}^{int}\} \Leftarrow \vec{\mathbf{F}}_i^{int}$$

9: **end for**

3.4.4 Solution with the Newton-Raphson Method

The Newton-Raphson method (Reddy, 2014) is used to solve for displacements until the magnitude of the displacement increment has met the requested criterion. In this implementation, the translational displacements are added vectorially, while the Euler rotation increments are converted to quaternions by assuming small deflections.

For each iteration, the tangential stiffness, defined as $[K_t] = \frac{\partial F_i}{\partial D_i}$, is used to solve for the incremental displacements $\Delta\vec{\mathbf{D}}_{i+1}$ using the difference of the external forces $\vec{\mathbf{F}}^{ext}$ and the internal forces $\vec{\mathbf{F}}_i^{int}$ (equation 3.19).

$$[K_t]_i \Delta\vec{\mathbf{D}}_{i+1} = \vec{\mathbf{F}}^{ext} - \vec{\mathbf{F}}_i^{int} \tag{3.19}$$

Once the incremental displacements are found, they are added to the displacement vector of the system $\vec{\mathbf{D}}_i$ to obtain the displacement vector $\vec{\mathbf{D}}_{i+1}$ used to compute the tangent stiffness matrix for the next iteration (equation 3.20).

$$\vec{\mathbf{D}}_{i+1} = \vec{\mathbf{D}}_i + \Delta\vec{\mathbf{D}}_{i+1} \tag{3.20}$$

The incremental displacements that are rotations are first converted to an incremental quaternion $\Delta\overset{\circlearrowleft}{q}_i$ using equations 3.11 through 3.15 and then added to the sum of accumulated rotations quaternion $\overset{\circlearrowleft}{q}_i$ through quaternion product (equation 3.21).

$$\overset{\circlearrowleft}{q}_{i+1} = \Delta\overset{\circlearrowleft}{q}_i \cdot \overset{\circlearrowleft}{q}_i \tag{3.21}$$

3.4.5 Load Stepping

In order to improve the integration of the loads, it is possible to use loading steps, whereby the load is dividing into fractions and applied incrementally (equation 3.22), which can avoid instabilities from causing divergence when significant nonlinearities are present (Reddy, 2006).

$$[K_t]\Delta\vec{\mathbf{D}}_{i+1} = \frac{step}{nsteps} \cdot \vec{\mathbf{F}}^{ext} - \vec{\mathbf{F}}_i^{int}$$

The Newton-Raphson method is then run to convergence for each loading step and the next increment applied until the full load has been applied and the last Newton-Raphson procedure has converged.

3.4.6 Force Following

As the Netwon-Raphson iterations proceed, each bar element will be translated and deformed and its referential will be rotated. In order for the forces to follow this journey, they have to be rotated after each iteration by the same increment as the nodes to which they are assigned to, which is done by applying the rotation matrix associated with the nodal incremental quaternion that was found in the previous iteration using the following two equations.

$$\vec{\mathbf{F}}_{node,i} = R(\Delta\overset{\circlearrowleft}{q}_i) \cdot \vec{\mathbf{F}}_{node,i-1} \tag{3.22}$$

$$\vec{\mathbf{M}}_{node,i} = R(\Delta\overset{\circlearrowleft}{q}_i) \cdot \vec{\mathbf{M}}_{node,i-1} \tag{3.23}$$

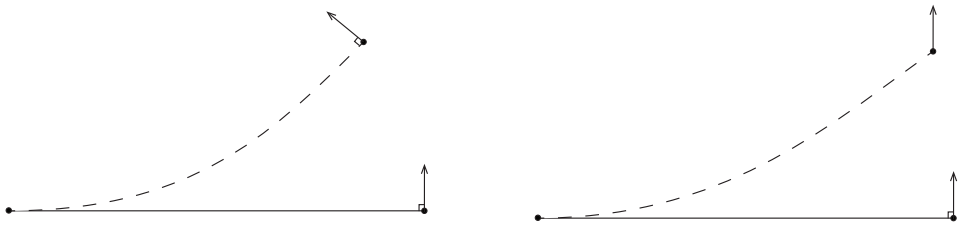

Figure 3.9 With force following (left) and without force following (right)

3.5 A case of tip moments

To verify the finite element solver, a large rotations analysis is performed based on a beam fixed at one end and having a moment exerted at the other (figure 3.10). The moment is increased by increments and the tip rotation angles are compared with the analytical solution, and with numerical results previously published by Siemens (2014) that were obtained with their modern version of MSC.Nastran (MSC, 2010).

Figure 3.10 Beam fixed at one end with a moment exerted at the other

The analytical solution provided by Geradin and Cardona (1988) relates the nondimensional displacements $\overline{x}$ and $\overline{z}$ in relation to the nondimensional moment $\overline{M}$ applied at the tip.

$$\overline{x} = \frac{x}{L} \qquad \overline{z} = \frac{z}{L} \qquad \overline{M} = \frac{ML}{2\pi EI}$$

$$\overline{x} = \frac{sin2\pi\overline{M}}{2\pi\overline{M}} \qquad \overline{z} = \frac{1 - cos2\pi\overline{M}}{2\pi\overline{M}}$$

In order to make a direct comparison with the data obtained with Nastran, it is given the same dimensions as were provided by Siemens. The cross-sectional area of the beam is $A = 0.15in^2$, the length of the beam L is of $12in$, the second moment of inertia I_{zz} is of $2.813e^{-4}in^4$ and the material's Young modulus E and shear modulus G are $2e^7lb/in^2$ and $1e^7lb/in^2$ respectively. Both softwares used a discretization of 12 bar elements.

The results obtained by OFEM are compared with Nastran in table 3.2 and in figure 3.11. It can be observed that the tip angles are in good agreement. However, figure 3.11 conveys a discrepancy between the deflection shape obtained by the two solvers.

Table 3.2 Comparison of the tip rotation angles

M (in-lb)	Tip Angle (deg) Nastran	Tip Angle (deg) OFEM
300	36.7	36.7
600	73.3	73.3
900	110.0	110.0
1200	146.7	146.7
1500	183.3	183.3
1800	220.0	220.0
2100	256.6	256.6
2400	293.3	293.3
2700	330.0	330.0
3000	366.6	366.6

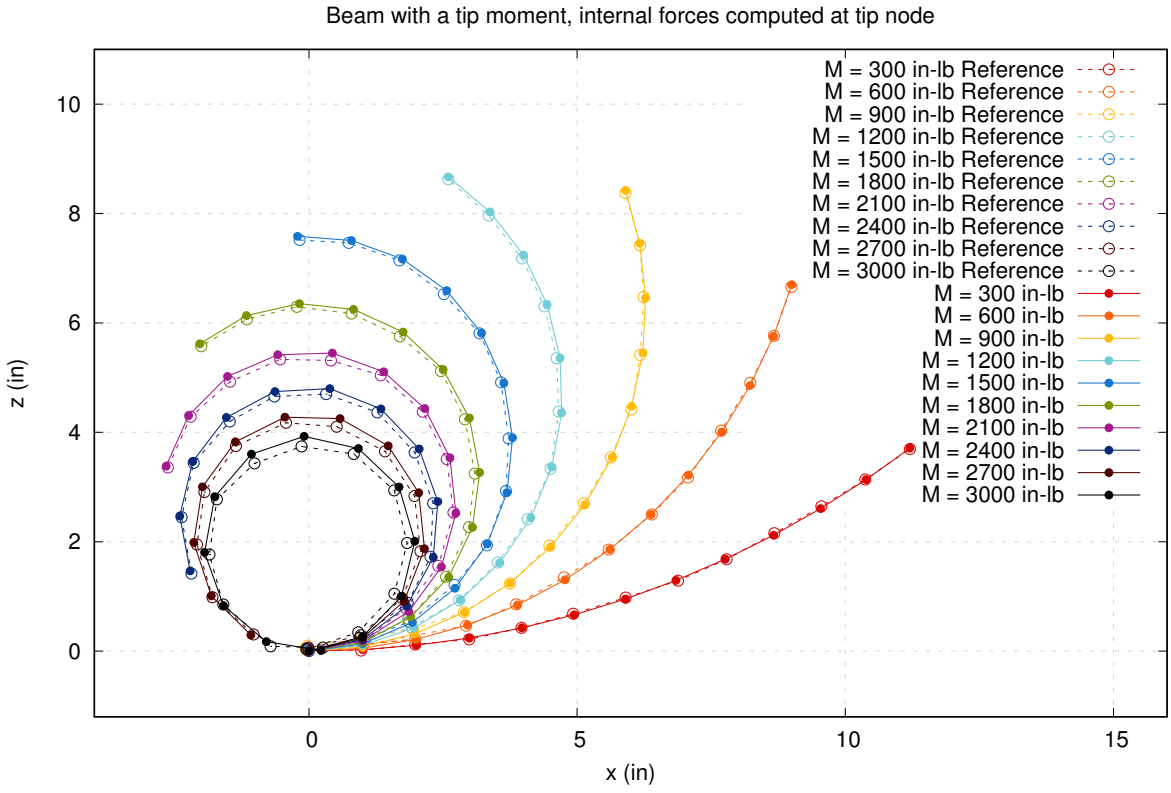

Figure 3.11 Deflection comparison between Nastran and OFEM

The Newton-Raphson method employed converged to below $1.0e^{-12}$ in four iterations on average for this case, yet once the tip displacements Δx_{tip} and Δx_{tip} are compared with the analytical solution in tables 3.3 and 3.4, a significant numeric error presents itself, which combined with the discrepancies when compared to Nastran demonstrate that additional steps are necessary to quantify the accuracy of the OFEM solver.

Table 3.3 Comparison of the tip displacement along the x axis (Internal forces computed at element tip node)

Tip Moment (in-lb)	Δx_{tip} Analytical	Δx_{tip} OFEM	Error (%)
300	-0.80230603306159409	-0.79697606934704357	0.664
600	-3.01761650829059036	-3.00025292628124118	0.575
900	-6.12544216175244571	-6.09896025172512157	0.432
1200	-9.42265627285932794	-9.39963925989504290	0.244
1500	-12.21681222312618331	-12.21345352084835945	0.027
1800	-14.00809397233867415	-14.03477752112003074	-0.190
2100	-14.60653995561400897	-14.65983340019240977	-0.364
2400	-14.15295500310000776	-14.21355761935491024	-0.428
2700	-13.04295305814467021	-13.08161735259765024	-0.296
3000	-11.78355032662915569	-11.77323757061324017	0.087

Table 3.4 Comparison of the tip displacement along the z axis (Internal forces computed at element tip node)

Tip Moment (in-lb)	Δz_{tip} Analytical	Δz_{tip} OFEM	Error (%)
300	3.71009030086515645	3.71177774551786488	-0.045
600	6.68619002011422303	6.69840924477494060	-0.182
900	8.38792189556092005	8.42268752248994446	-0.414
1200	8.60467968632780256	8.66885693016107339	-0.745
1500	7.49506153157441624	7.58397904306088666	-1.186
1800	5.52068731166445126	5.61753795273181122	-1.754
2100	3.29811595526942902	3.38027489833784500	-2.491
2400	1.41685759427615299	1.46675057554380994	-3.521
2700	0.27979959224566653	0.29534125481444090	-5.554
3000	0.01253311591634860	0.01175167939697390	6.234

The tip moment case is pursued once more with the internal forces computed at the element's center (figure 3.12). This method achieves much better agreement with the data obtained with Nastran, as well as with the analytical solution (table 3.5). This suggests that the nonlinearity due to large deflections is more adequately captured with the internal forces computed at the element's center.

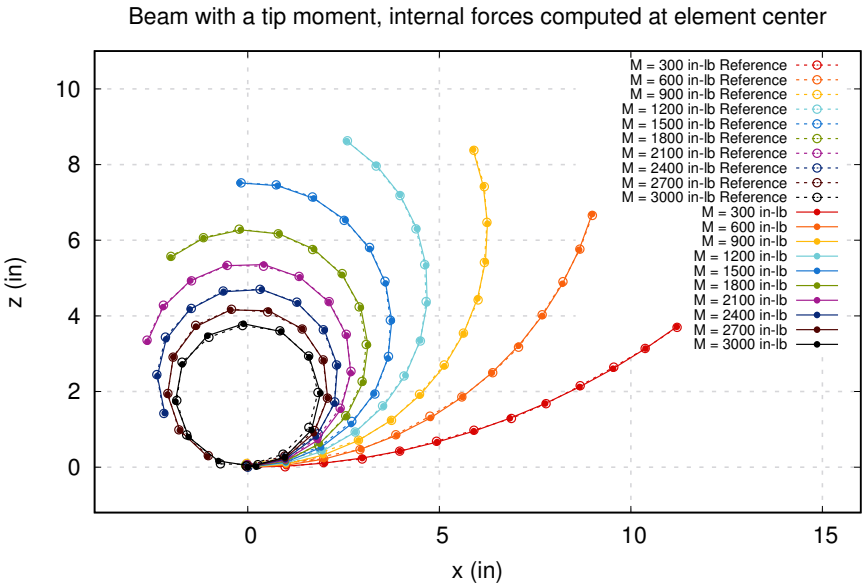

Figure 3.12 Deflections with 12 elements (internal forces computed at element center)

Table 3.5 Comparison of the tip displacement along the x axis (Internal forces computed at element center)

Tip Moment (in-lb)	Δx_{tip} Analytical	Δx_{tip} OFEM	Error (%)
300	-0.80230603306159409	-0.80097926067295777	0.001653
600	-3.01761650829059036	-3.01335829426890278	0.001411
900	-6.12544216175244571	-6.11917351552171329	0.001023
1200	-9.42265627285932794	-9.41776411202355490	0.000519
1500	-12.21681222312618331	-12.21745573531467954	-0.000052
1800	-14.00809397233867415	-14.01668443477094961	-0.000613
2100	-14.60653995561400897	-14.62173353296171996	-0.001040
2400	-14.15295500310000776	-14.16936682582674045	-0.001159
2700	-13.04295305814467021	-13.05302949429603920	-0.000772
3000	-11.78355032662915569	-11.78096448085582004	0.000219

Rotation about the z-axis

In order to verify the ability of the solver to handle three dimensions, the tip moment problem is solved after being rotated about the z-axis by an angle θ as shown in figure 3.13. This quaternion large rotations implementation was tested by rotating the problem about the z axis in increments of 1 degree and verifying that the solution was not altered by this rotation. The solutions are presented in figure 3.14, the potential energy in figure 3.15 and the solution for a rotation of 45 degrees about the z-axis in figure 3.16. It can be seen that the deflections and potential energy are unaffected by the rotation, as the potential energy is the same for every position.

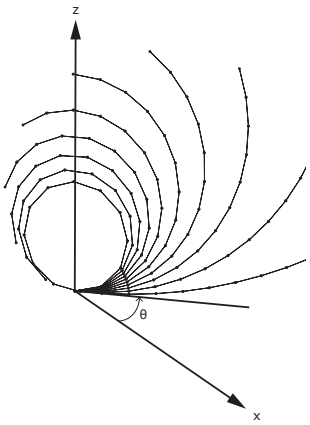

Figure 3.13 Rotation of the problem about the z-axis

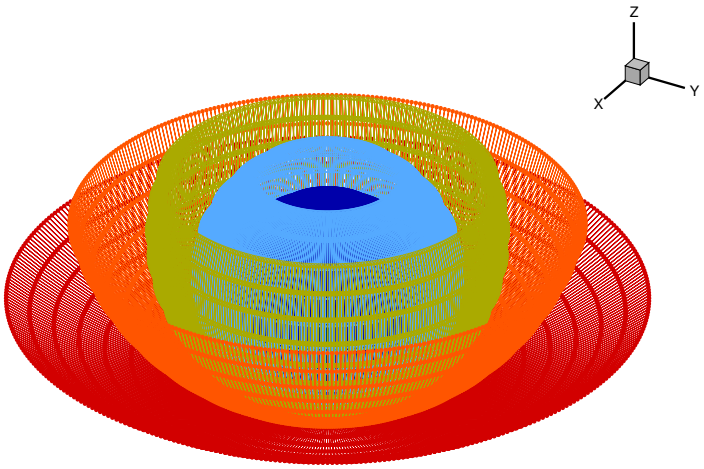

Figure 3.14 Problem computed about the z axis in increments of one degree

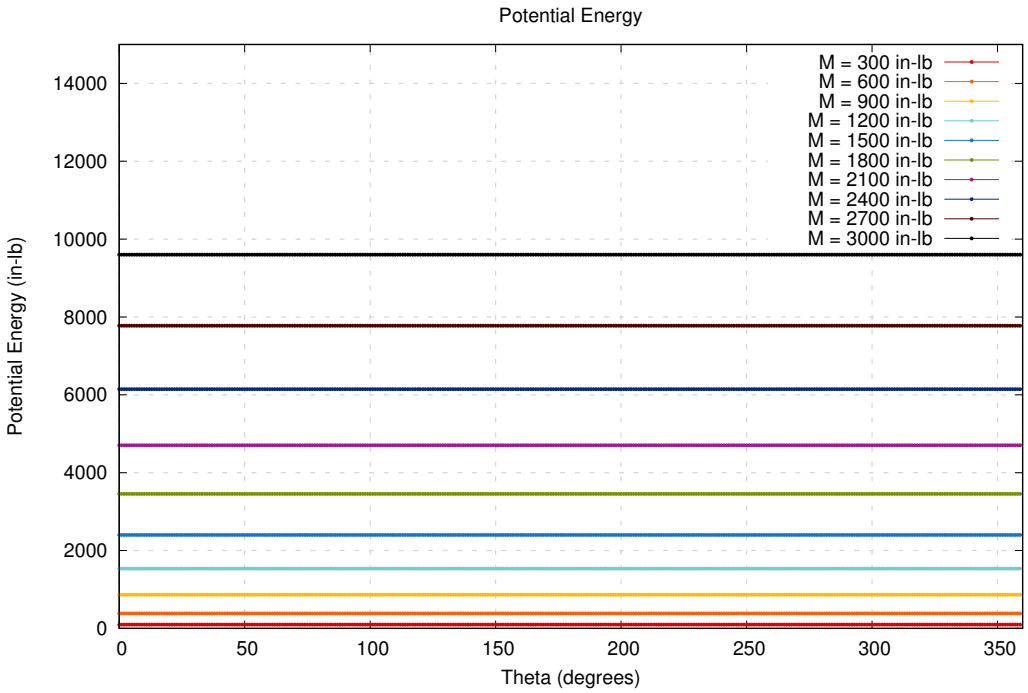

Figure 3.15 Potential energy of the rotated Finite Element Models

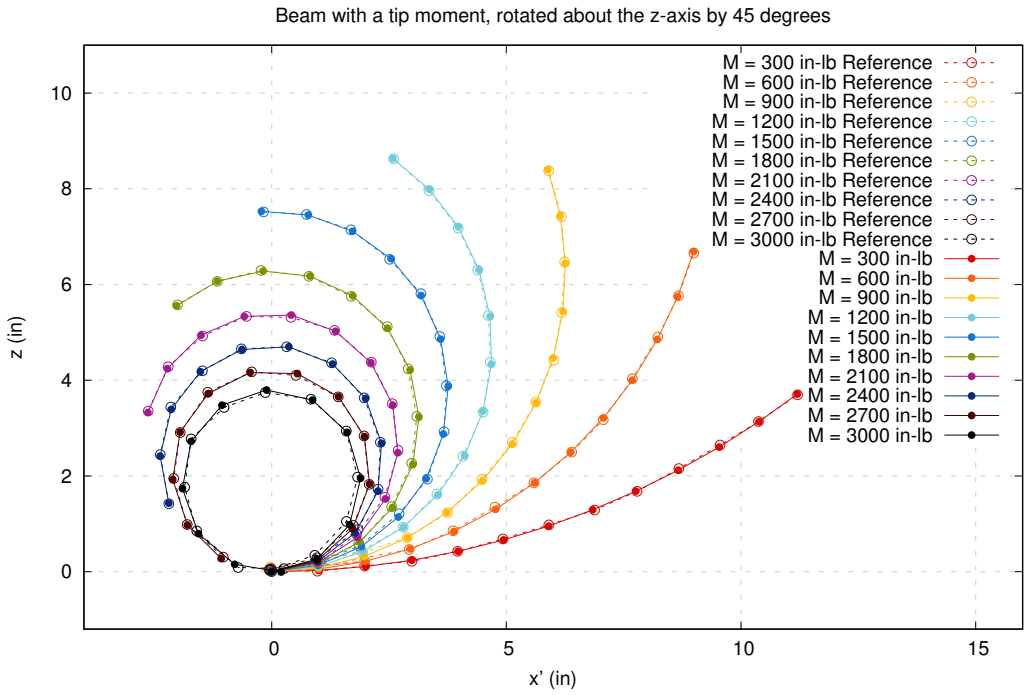

Figure 3.16 Deflections for a rotation of 45 degrees about the z-axis (internal forces computed at element center)

Discretization in Space

To quantify the accuracy of the nonlinear solver when it is computing internal forces at the element tip nodes, a space discretization study is conducted with the number of elements increasing from 2 to 512, the latter being taken as a reference to compute relative errors which are plotted in figures 3.17 against the number of elements, where a quadratic convergence is clearly observed in the displacements along the x and z axe, as is expected. The displacement is shown to converge to the solution obtained with Nastran in figures 3.18, the discrepancy previously observed gradually disappears as the number of elements is increased. However, it must be noted that the solutions having only 2 or 4 elements exhibit problematic behavior at higher loadings. Finally, the tip displacements presented in tables 3.6 and 3.7 demonstrate that the nonlinear solver converges towards the analytical solution quadratically as well.

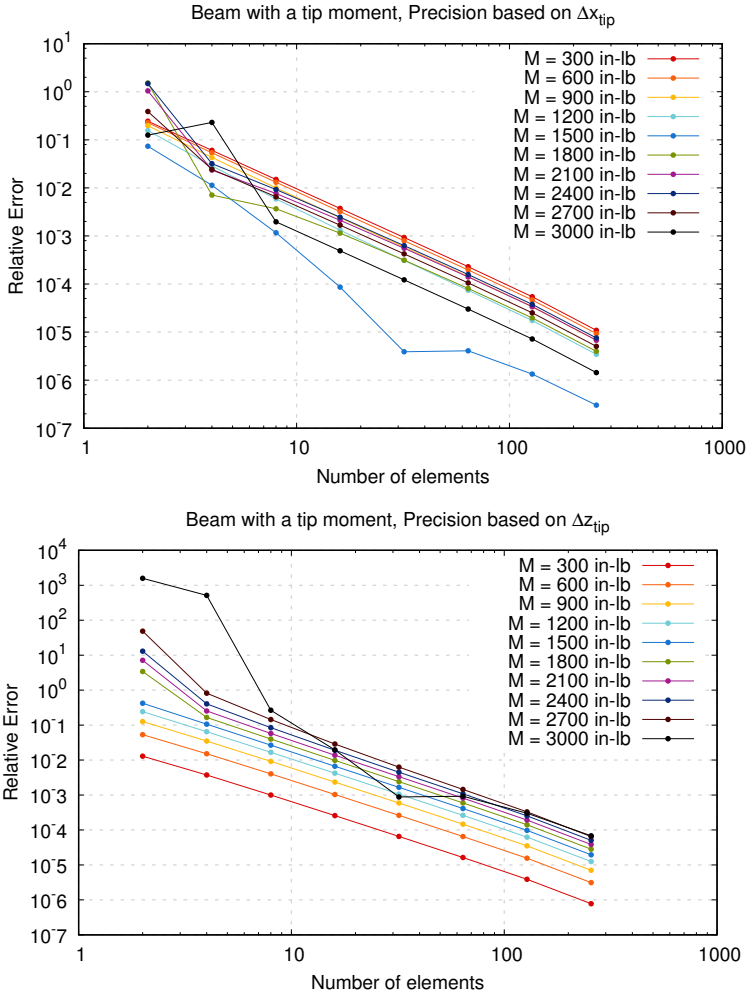

Figure 3.17 Relative error for an increasing number of elements (internal forces computed at element tip node)

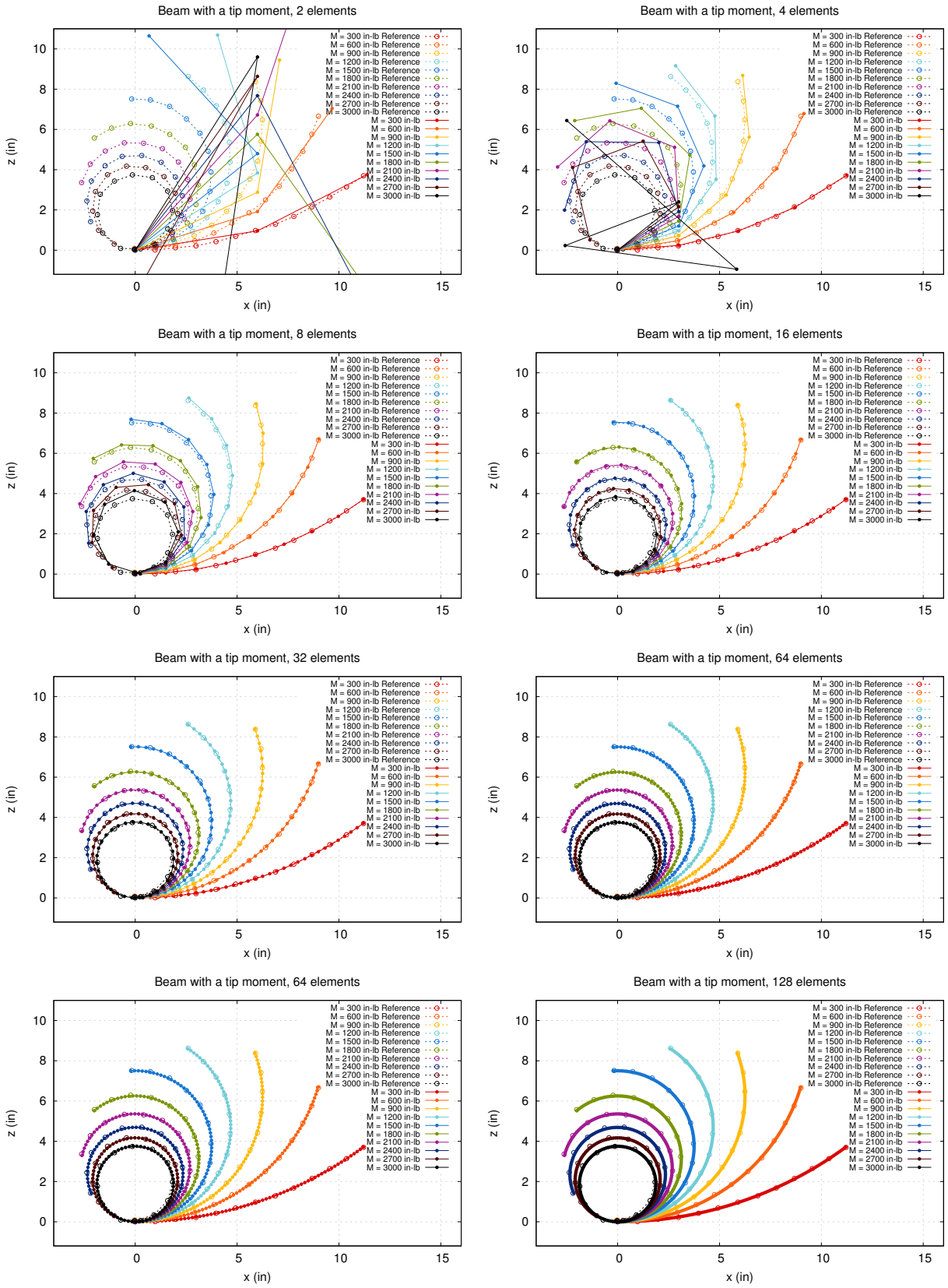

Figure 3.18 Deflections for an increasing number of elements (internal forces computed at element tip node)

Table 3.6 Tip displacement along the x axis for an increasing number of elements (internal forces computed at element tip node)

M (in-lb)	Number of elements	Δx_{tip} Analytical	Δx_{tip} OFEM	Error (%)
300	2	-0.80230603306159409	-0.60635854648693110	24.42303
300	4	-0.80230603306159409	-0.75392325836282681	6.03046
300	8	-0.80230603306159409	-0.79028759369717605	1.49798
300	16	-0.80230603306159409	-0.79931119398549966	0.37327
300	32	-0.80230603306159409	-0.80155855192748571	0.09316
300	64	-0.80230603306159409	-0.80211931681829829	0.02327
300	128	-0.80230603306159409	-0.80225937328476848	0.00581
300	256	-0.80230603306159409	-0.80229437052970476	0.00145
300	512	-0.80230603306159409	-0.80230311773027863	0.00036
1800	2	-14.00809397233867415	7.35546260276353081	152.50866
1800	4	-14.00809397233867415	-14.10740781353639939	0.70897
1800	8	-14.00809397233867415	-14.05950470462462043	0.36700
1800	16	-14.00809397233867415	-14.02417428785781972	0.11479
1800	32	-14.00809397233867415	-14.01251373372464926	0.03155
1800	64	-14.00809397233867415	-14.00924870164510061	0.00824
1800	128	-14.00809397233867415	-14.00838886955209972	0.00210
1800	256	-14.00809397233867415	-14.00816847301842927	0.00053
1800	512	-14.00809397233867415	-14.00811269452734997	0.00013
3000	2	-11.78355032662915569	-10.30538030729483978	12.544351
3000	4	-11.78355032662915569	-14.49716376811051077	23.028827
3000	8	-11.78355032662915569	-11.76032539730358017	0.197096
3000	16	-11.78355032662915569	-11.77775461376861088	0.049184
3000	32	-11.78355032662915569	-11.78210414458795974	0.012272
3000	64	-11.78355032662915569	-11.78318921343234926	0.003064
3000	128	-11.78355032662915569	-11.78346010795640986	0.000765
3000	256	-11.78355032662915569	-11.78352777976468069	0.000191
3000	512	-11.78355032662915569	-11.78354469091044088	0.000047

Table 3.7 Tip displacement along the z axis for an increasing number of elements (internal forces computed at element tip node)

M (in-lb)	Number of elements	Δz_{tip} Analytical	Δz_{tip} OFEM	Error (%)
300	2	3.71009030086515645	3.75802597547172912	1.292035
300	4	3.71009030086515645	3.72400014658408196	0.374919
300	8	3.71009030086515645	3.71380733062283008	0.100187
300	16	3.71009030086515645	3.71104944802551984	0.025852
300	32	3.71009030086515645	3.71033382087569796	0.006563
300	64	3.71009030086515645	3.71015164734952796	0.001653
300	128	3.71009030086515645	3.71010569578629212	0.000414
300	256	3.71009030086515645	3.71009415688232691	0.000103
300	512	3.71009030086515645	3.71009126578027493	0.000026
1800	2	5.52068731166445126	-13.32186109358820048	341.308017
1800	4	5.52068731166445126	6.43685795640846603	16.595227
1800	8	5.52068731166445126	5.74148142602704858	3.999395
1800	16	5.52068731166445126	5.57479877118116285	0.980158
1800	32	5.52068731166445126	5.53407520247289941	0.242504
1800	64	5.52068731166445126	5.52401651160239293	0.060304
1800	128	5.52068731166445126	5.52151737213171590	0.015035
1800	256	5.52068731166445126	5.52089454569992810	0.003753
1800	512	5.52068731166445126	5.52073908496604115	0.000937
3000	2	0.01253311591634860	-19.84172590626161892	158414.389164
3000	4	0.01253311591634860	6.44106722659940978	51292.385338
3000	8	0.01253311591634860	0.00919716767938727	26.617070
3000	16	0.01253311591634860	0.01228833142326371	1.953101
3000	32	0.01253311591634860	0.01254445293630674	0.090456
3000	64	0.01253311591634860	0.01254497984767778	0.094660
3000	128	0.01253311591634860	0.01253720929504422	0.032660
3000	256	0.01253311591634860	0.01253428013431054	0.009289
3000	512	0.01253311591634860	0.01253342457774767	0.002462

The same space discretization study is conducted for the nonlinear solver computing the internal forces at the element centers and it can be readily observed in figures 3.19 that once more, the convergence is quadratic for displacements.

Inspection of the displacements in figures 3.20, as well as the tip displacements in tables 3.8 and 3.9 reveals that this approach exhibits far better behavior however, especially with a low number of elements, where it is able to provide reasonable approximations of the tip displacements even when the topology of the deflection is crude. This suggests that the use of the element's central referential improves the adherence to the small deformations assumptions inherent in linear bar elements, as it achieves better accuracy than the tip node approach.

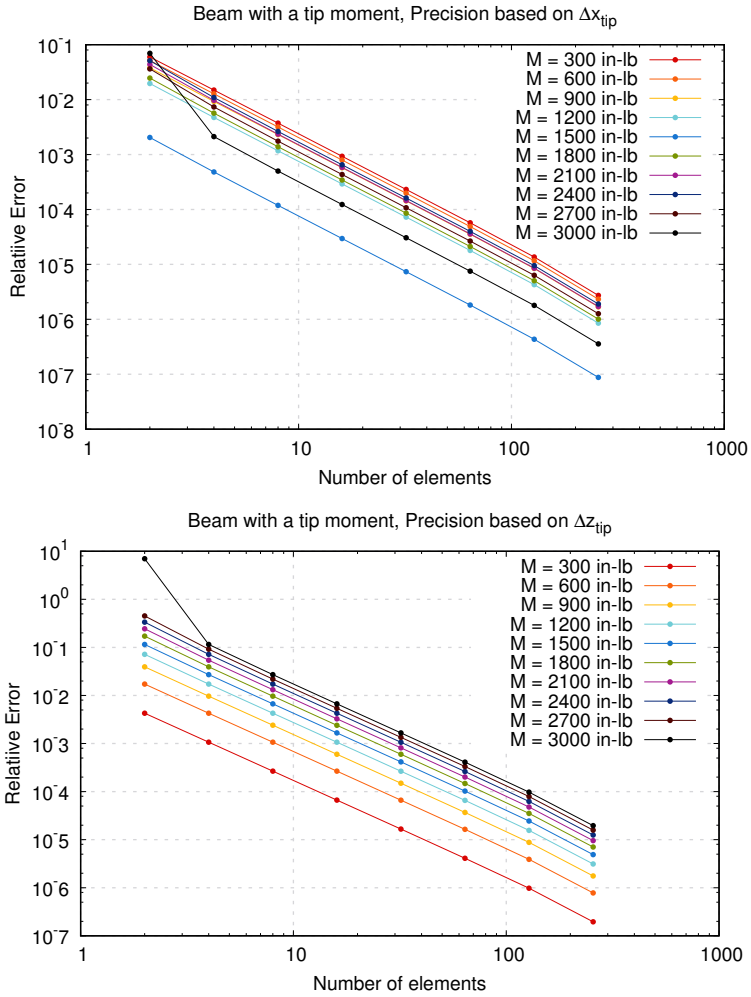

Figure 3.19 Relative error for an increasing number of elements (internal forces computed at element center)

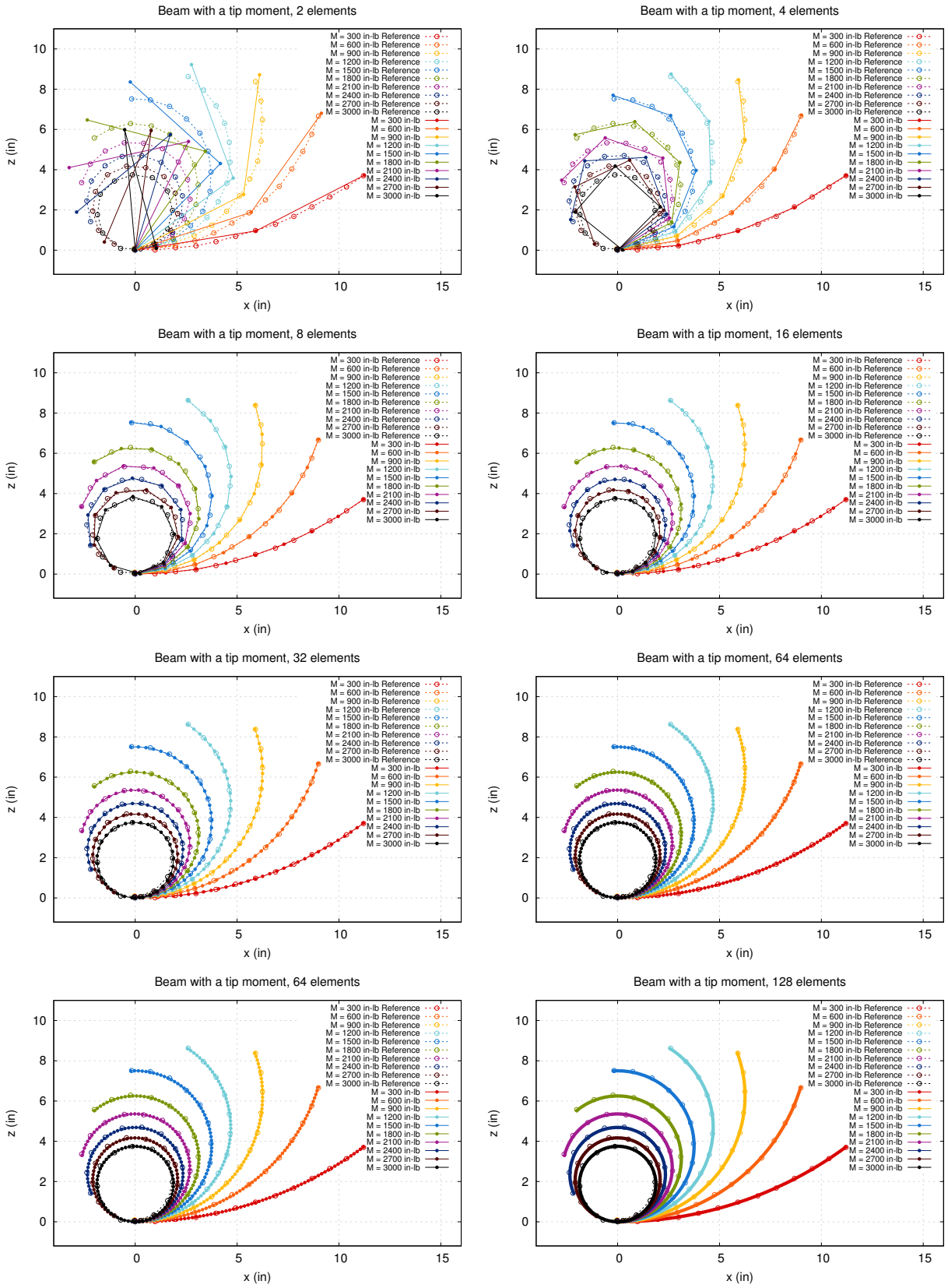

Figure 3.20 Deflections for an increasing number of elements (internal forces computed at element center)

Table 3.8 Tip displacement along the x axis for an increasing number of elements (internal forces computed at element center)

M (in-lb)	Number of elements	Δx_{tip} Analytical	Δx_{tip} OFEM	Error (%)
300	2	-0.80230603306159409	-0.75440321044857106	5.97064220
300	4	-0.80230603306159409	-0.79035715384250105	1.48931688
300	8	-0.80230603306159409	-0.79932048566722191	0.37212077
300	16	-0.80230603306159409	-0.80155975067256235	0.09301717
300	32	-0.80230603306159409	-0.80211946899219200	0.02325347
300	64	-0.80230603306159409	-0.80225939245234923	0.00581331
300	128	-0.80230603306159409	-0.80229437293450612	0.00145332
300	256	-0.80230603306159409	-0.80230311800967535	0.00036333
300	512	-0.80230603306159409	-0.80230530426182589	0.00009083
1800	2	-14.00809397233867415	-15.24306828011023995	4.357830
1800	4	-14.00809397233867415	-14.74787763327143075	0.967632
1800	8	-14.00809397233867415	-14.64090053410012082	0.235241
1800	16	-14.00809397233867415	-14.61507112287277010	0.058406
1800	32	-14.00809397233867415	-14.60866908990650970	0.014576
1800	64	-14.00809397233867415	-14.60707201102423980	0.003642
1800	128	-14.00809397233867415	-14.60667295521036912	0.000910
1800	256	-14.00809397233867415	-14.60657320471701048	0.000227
1800	512	-14.00809397233867415	-14.60654826954086971	0.000056
3000	2	-11.78355032662915569	-10.96330508815971072	6.960934
3000	4	-11.78355032662915569	-11.75862353826387974	0.211538
3000	8	-11.78355032662915569	-11.77767087378427924	0.049895
3000	16	-11.78355032662915569	-11.78210108404502066	0.012298
3000	32	-11.78355032662915569	-11.78318928438445923	0.003063
3000	64	-11.78355032662915569	-11.78346014505376971	0.000765
3000	128	-11.78355032662915569	-11.78352778601037976	0.000191
3000	256	-11.78355032662915569	-11.78354469301902085	0.000047
3000	512	-11.78355032662915569	-11.78354890587229953	0.000012

Table 3.9 Tip displacement along the z axis for an increasing number of elements (internal forces computed at element center)

M (in-lb)	Number of elements	Δz_{tip} Analytical	Δz_{tip} OFEM	Error (%)
300	2	3.71009030086515645	3.72596176494386588	0.42779185
300	4	3.71009030086515645	3.71404927858216194	0.10670839
300	8	3.71009030086515645	3.71107949118088420	0.02666216
300	16	3.71009030086515645	3.71033756383393198	0.00666460
300	32	3.71009030086515645	3.71015211444492321	0.00166609
300	64	3.71009030086515645	3.71010575412524402	0.00041651
300	128	3.71009030086515645	3.71009416417116622	0.00010412
300	256	3.71009030086515645	3.71009126664243105	0.00002603
300	512	3.71009030086515645	3.71009054222543400	0.00000650
1800	2	5.52068731166445126	4.10353012836904441	24.4204322
1800	4	5.52068731166445126	3.47695382374661799	5.4224251
1800	8	5.52068731166445126	3.34159319868982108	1.3182448
1800	16	5.52068731166445126	3.30891064069027196	0.3272985
1800	32	5.52068731166445126	3.30080999867366920	0.0816843
1800	64	5.52068731166445126	3.29878917751335887	0.0204123
1800	128	5.52068731166445126	3.29828424241903706	0.0051025
1800	256	5.52068731166445126	3.29815802681546399	0.0012756
1800	512	5.52068731166445126	3.29812646289887512	0.0003185
3000	2	0.01253311591634860	0.10023311306645870	699.74615
3000	4	0.01253311591634860	0.01397645525310528	11.51620
3000	8	0.01253311591634860	0.01287355470227137	2.71631
3000	16	0.01253311591634860	0.01261703161389661	0.66955
3000	32	0.01253311591634860	0.01255402139696297	0.16680
3000	64	0.01253311591634860	0.01253833771962790	0.04166
3000	128	0.01253311591634860	0.01253442109850470	0.01041
3000	256	0.01253311591634860	0.01253344242448176	0.00260
3000	512	0.01253311591634860	0.01253319717770663	0.00064

Force Loading Discretization

In a final verification for the nonlinear steady solver, the force load stepping procedure is tested by conducting a discretization study. The number of loading steps is increased from 1 to 4096 steps and their impact on the precision of the solution is presented in figures 3.21 where the errors are computed against the solution with 4096 steps. The error is shown not to vary with the number of loading steps in this particular case. However, this demonstrates that the addition of loading steps produces no bias in the computed result. Furthermore, it can be seen in figures 3.22 and 3.23 that the convergence behavior is not altered positively or negatively by the addition of the loading steps, as the number of iterations per step remains at similar orders of magnitude.

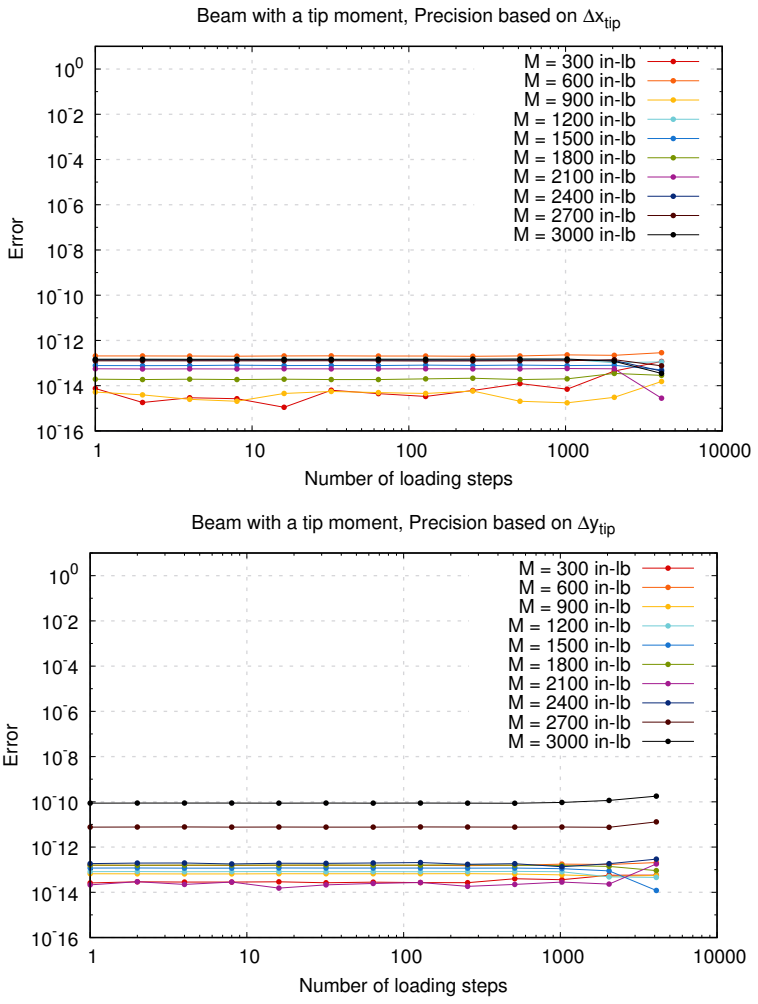

Figure 3.21 Relative error for an increasing number of loading steps (internal forces computed at element tip nodes)

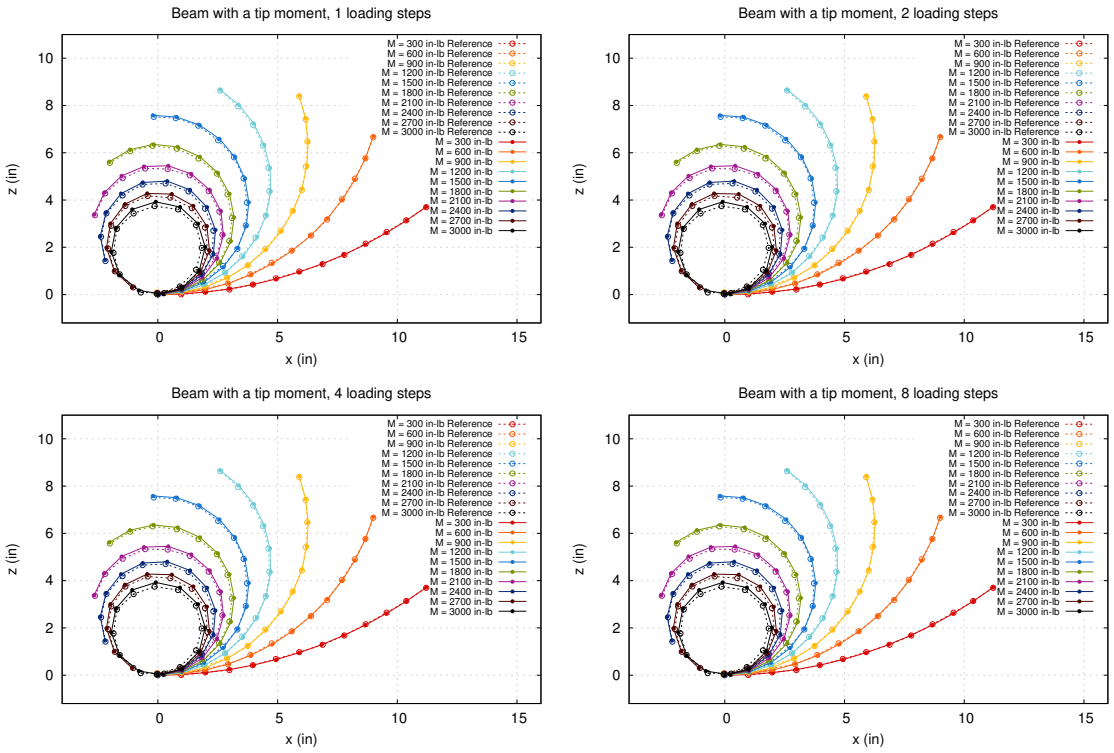

Figure 3.22 Deflections for an increasing number of loading steps

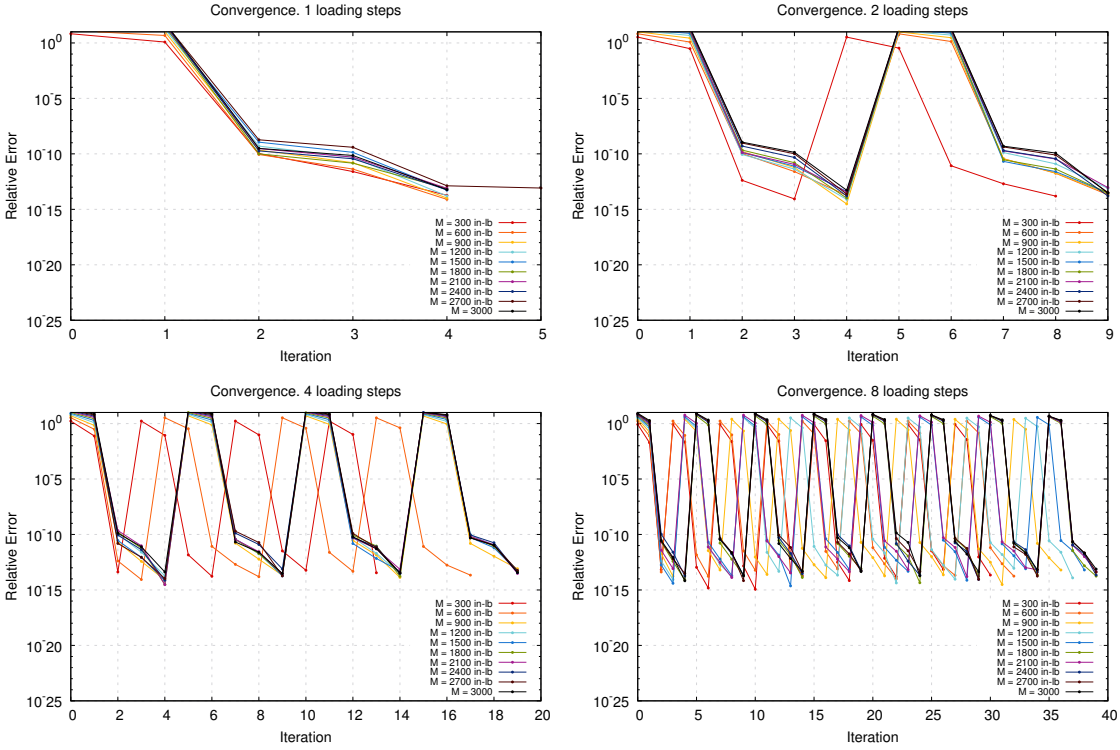

Figure 3.23 Convergence for an increasing number of loading steps

3.6 Finite Elements for Unsteady Cases

The method used in OFEM for unsteady nonlinear solution of finite elements is summarized by Cook *et al.* (2002), although the co-rotational formulation is used with the internal force computations obtained through the quaternion methodology presented at the beginning of this chapter.

Using step by step integration in time is referred to as a direct integration method and relies on the discretization in time with regular timesteps Δt of the equations of motion of the system, which are expressed in matrix form for timestep i as

$$M\ddot{\mathbf{D}}_i + C\dot{\mathbf{D}}_i + \mathbf{F}_i^{int} = \mathbf{F}_i^{ext} \tag{3.24}$$

where M denotes a mass matrix, C a damping matrix, $\dot{\mathbf{D}}_i$ the nodal velocities, $\mathbf{D}_i$ the nodal accelerations, $\mathbf{F}_i^{int}$ the internal forces and $\mathbf{F}_i^{ext}$ the external forces.

3.6.1 Explicit Direct Integration Method

By using the finite difference method in time with a central difference, the acceleration and velocity terms are obtained by

$$\dot{\mathbf{D}}_i = \frac{1}{2\Delta t}(\mathbf{D}_{i+1} - \mathbf{D}_{i-1}) \tag{3.25}$$

$$\ddot{\mathbf{D}}_i = \frac{1}{\Delta t^2}(\mathbf{D}_{i+1} + 2\mathbf{D}_i - \mathbf{D}_{i-1}) \tag{3.26}$$

Once these equations are substituted into the matrix form of the equations of motion, the following explicit direct integration method is formed when neglecting the damping matrix (Cook *et al.*, 2002), where the internal forces are provided in exactly the same manner as in the stationary nonlinear case.

$$\frac{1}{\Delta t^2} M\mathbf{D}_{i+1} = \mathbf{F}_i^{ext} - \mathbf{F}_i^{int} + \frac{2}{\Delta t^2} M \cdot \mathbf{D_i} - \frac{1}{\Delta t^2} M \cdot \mathbf{D}_{i-1} \tag{3.27}$$

The explicit method is a second order method , that is conditionally stable and requires that timesteps be decreased if the number of degrees of freedom is increased (Hughes, 1983).

3.6.2 Newmark Direct Integration Method

A variation on the finite difference equations used in the explicit method are the Newmark equations where a pair of parameters β and γ control the implicit integration (Newmark, 1959).

$$\dot{\mathbf{D}}_{i+1} = \dot{\mathbf{D}}_i + \Delta t(\gamma\ddot{\mathbf{D}}_{i+1} + (1-\gamma)\ddot{\mathbf{D}}_i) \tag{3.28}$$

$$\mathbf{D}_{i+1} = \mathbf{D}_i + \Delta t\dot{\mathbf{D}}_i + \frac{1}{2}\Delta t^2(2\beta\ddot{\mathbf{D}}_{i+1} + (1-2\beta)\ddot{\mathbf{D}}_i) \tag{3.29}$$

Using these equations, it is possible through substitution to obtain the following implicit terms for the acceleration and the velocity of the system.

$$\ddot{\mathbf{D}}_{i+1} = \frac{1}{\beta\Delta t^2}(\mathbf{D}_{i+1} - \mathbf{D}_i - \Delta t\dot{\mathbf{D}}_i) - (\frac{1}{2\beta} - 1)\ddot{\mathbf{D}}_i \tag{3.30}$$

$$\dot{\mathbf{D}}_{i+1} = \frac{\gamma}{\beta\Delta t}(\mathbf{D}_{i+1} - \mathbf{D}_i) - (\frac{\gamma}{\beta} - 1)\dot{\mathbf{D}}_i - \Delta t(\frac{\gamma}{2\beta} - 1)\ddot{\mathbf{D}}_i \tag{3.31}$$

Once these equations are inserted into the matrix form of the equations of motion, the following implicit *Newmark* direct integration method appears with parameters γ and β, along with an effective stiffness matrix K_{eff}.

$$K_{eff}\mathbf{D}_{i+1} = \mathbf{F}_{i+1}^{ext} - \mathbf{F}_i^{int} + M(\frac{1}{\beta\Delta t}\dot{\mathbf{D}}_i + (\frac{1}{2\beta} - 1)\ddot{\mathbf{D}}_i) \tag{3.32}$$

$$K_{eff} = \frac{M}{\beta\Delta t^2} + K_t \tag{3.33}$$

As shown in table 3.10, by varying the parameters β and γ, it possible to confer unconditional stability or fourth order convergence to the time integration (Hughes, 1983). It is important to note, however, that unconditional stability is only guaranteed in the linear unsteady case, not the nonlinear unsteady case. A notable disadvantage of the Newmark methods is that the effective stiffness matrix is typically less sparse than the mass matrix that the explicit method has to solve, conferring it a greater computational cost per timestep.

Table 3.10 Accuracy of Newmark Methods

γ	β	stability	Error
1/2	1/4	Unconditional	second order
1/2	1/6	Conditional	second order
1/2	1/12	Conditional	fourth order

Furthermore, in order to limit the energy imbalance, it is necessary to use equilibrium iterations where the error R_{i+1}^{err} is added to the external forces $\mathbf{F}_{i+1}^{ext}$ and the timestep is repeated, until the energy error W^{err} is under a prescribed tolerance.

$$R_{i+1}^{err} = \mathbf{F}_{i+1}^{ext} - M\ddot{\mathbf{D}}_{i+1} - \mathbf{F}_{i+1}^{int} \tag{3.34}$$

$$W^{err} = \dot{\mathbf{D}}_{i+1}^{\top} R_{i+1}^{err} \Delta t \tag{3.35}$$

3.6.3 Initial Acceleration

For both schemes, if the damping matrix is neglected, the initial acceleration relies on the initial displacement alone. The use of the next displacement will reduce the Newmark schemes to first order (Hulbert and Hughes, 1987).

$$\ddot{D}_0 = M^{-1}(R_0^{ext} - K_t \cdot D_0)$$

3.7 A case of tip rotations

A case of large rotations is studied in order to verify the accuracy of the nonlinear unsteady finite element solver, which consists of a beam being rotated at its base from an angle of 0 radians to 1.5 radians in a span of 5 seconds. Following the initial rotation, the angle of 1.5 radians is maintained while the beam undergoes free vibration (Fotouhi, 2007).

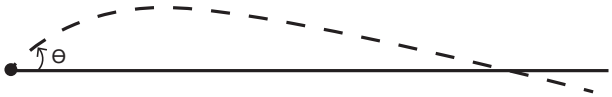

Figure 3.24 Forces to be applied onto the FEM for each column of vortex rings

The beam has a length L of $0.254m$, a Young modulus E of $0.276Gpa$, a cross sectional area A of $1.61e-4m^2$, a sectional second moment of inertia I of $1.04e-8m^4$ and a density ρ of $57.7Gg/m^3$.

It is necessary to demonstrate convergence both in time and space in order to establish the accuracy of the unsteady nonlinear finite element solver. In doing so, the computations are compared with the data published by Fotouhi (2007) who was making use of 50 BEAM3 elements within the commercial software ANSYS.

3.7.1 Space Discretization

The accuracy of the O-FEM solver in the time domain is first tested by performing a space discretization study, increasing the number of bar elements from 8 to 128, the latter being used as a reference to find relative errors. Furthermore, three variants of direct integration are utilized : the explicit scheme, a second order Newmark scheme and a fourth order Newmark scheme.

It is chosen to proceed with a timestep dt of $1.0e-5$ as this was found to be stable for the three schemes. The results obtained for times 5s, 7s and 9s are presented in tables 3.11, 3.12 and 3.13, where the relative error decreases quadratically for displacements for all three schemes that were utilized. The deflections that are obtained are presented in figures 3.25, 3.26 and 3.27, which demonstrate that large errors persist when only 8 elements are used, whereas a refinement of 16 elements produces qualitatively accurate results.

Table 3.11 Tip displacement using the Explicit scheme

t(s)	$n_{Elements}$	x_{tip}	Error (%)	z_{tip}	Error (%)
5.0	8	-0.27718316008192995	3.9247	0.95199370809367079	0.3942
5.0	16	-0.26825527351460471	0.5773	0.95572528404826662	0.0037
5.0	32	-0.26709445522061392	0.1421	0.95566580553509961	0.0100
5.0	64	-0.26689209938732555	0.0662	0.95571289167055906	0.0050
5.0	128	-0.26671535901981652	-	0.95576156621007835	-
7.0	8	-0.14580897354911240	46.0647	0.98227960412054638	1.2276
7.0	16	-0.11456867680877933	14.7696	0.99133763438448852	0.3168
7.0	32	-0.10402020772229863	4.2026	0.99377110128272783	0.0721
7.0	64	-0.10093345467031727	1.1105	0.99429512348906846	0.0194
7.0	128	-0.09982488293491601	-	0.99448833739173947	-
9.0	8	0.52006084666133645	4.3116	0.83581118603075544	1.8656
9.0	16	0.50152204099858133	0.5932	0.85121289813320611	0.0572
9.0	32	0.49921584223074372	0.1306	0.85194675603516345	0.0288
9.0	64	0.49893058319313593	0.0734	0.85163826924810271	0.0073
9.0	128	0.49856449765345606	-	0.85170068071483718	-

Table 3.12 Tip displacement using the Newark scheme with $\beta = 1/4$ and $\gamma = 1/2$

t(s)	$n_{Elements}$	x_{tip}	Error (%)	z_{tip}	Error (%)
5.0	8	-0.27718473390674520	3.9252	0.95199298227741636	0.3943
5.0	16	-0.26825659736937635	0.5778	0.95572483150572074	0.0038
5.0	32	-0.26709574268474900	0.1426	0.95566527013681424	0.0100
5.0	64	-0.26689370350561037	0.0668	0.95571218900881982	0.0051
7.0	8	-0.14581210270099271	46.0678	0.98227859971188347	1.2277
7.0	16	-0.11457196885885806	14.7729	0.99133683178808674	0.3168
7.0	32	-0.10402269437527337	4.2051	0.99377061703208602	0.0721
7.0	64	-0.10093602006921058	1.1130	0.99429465130386785	0.0194
9.0	8	0.52006486831794807	4.3124	0.83580801002978611	1.8659
9.0	16	0.50152504091248751	0.5938	0.85121099703447500	0.0574
9.0	32	0.49921886237876933	0.1312	0.85194504999746523	0.0286
9.0	64	0.49893381400740233	0.0740	0.85163650706242167	0.0075

Table 3.13 Tip displacement using the Newark scheme with $\beta = 1/12$ and $\gamma = 1/2$

t(s)	$n_{Elements}$	x_{tip}	Error (%)	z_{tip}	Error (%)
5.0	8	-0.27718473410097955	3.9252	0.95199298194652826	0.3943
5.0	16	-0.26825659824441089	0.5778	0.95572483081605075	0.0038
5.0	32	-0.26709575848679501	0.1426	0.95566526344529146	0.0100
5.0	64	-0.26689365472877347	0.0668	0.95571221738438994	0.0051
7.0	8	-0.14581210330162575	46.0678	0.98227860129243449	1.2277
7.0	16	-0.11457197034707925	14.7729	0.99133683184624821	0.3168
7.0	32	-0.10402271795910138	4.2051	0.99377061035302561	0.0721
7.0	64	-0.10093584723865122	1.1129	0.99429468110750818	0.0194
9.0	8	0.52006486816827857	4.3124	0.83580801038790631	1.8659
9.0	16	0.50152503993655306	0.5938	0.85121099666269329	0.0574
9.0	32	0.49921886194343307	0.1312	0.85194504890508449	0.0286
9.0	64	0.49893381982005586	0.0740	0.85163649376628514	0.0075

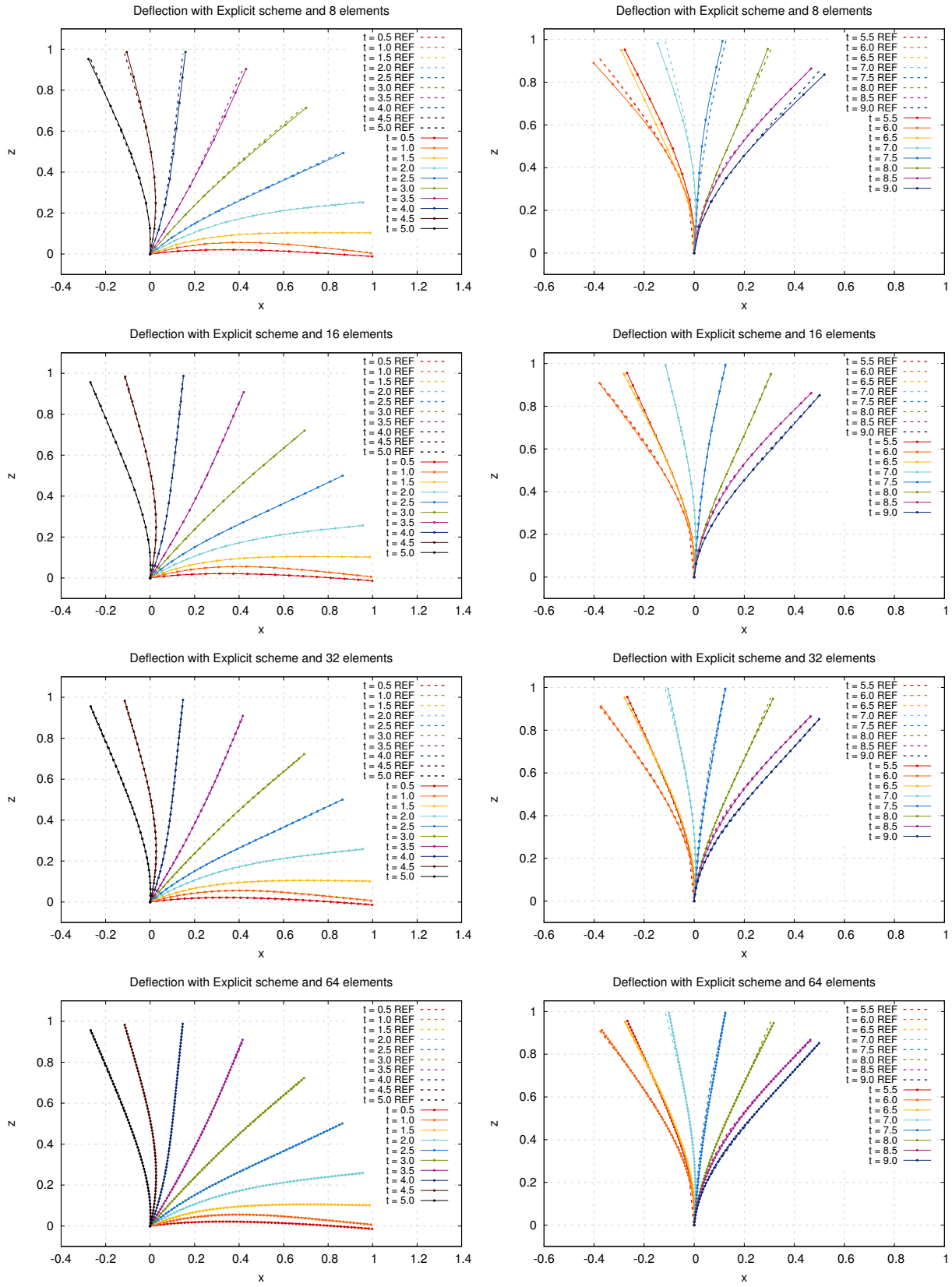

Figure 3.25 Deflections for an increasing number of elements using the Explicit scheme, and dt = 1e-5

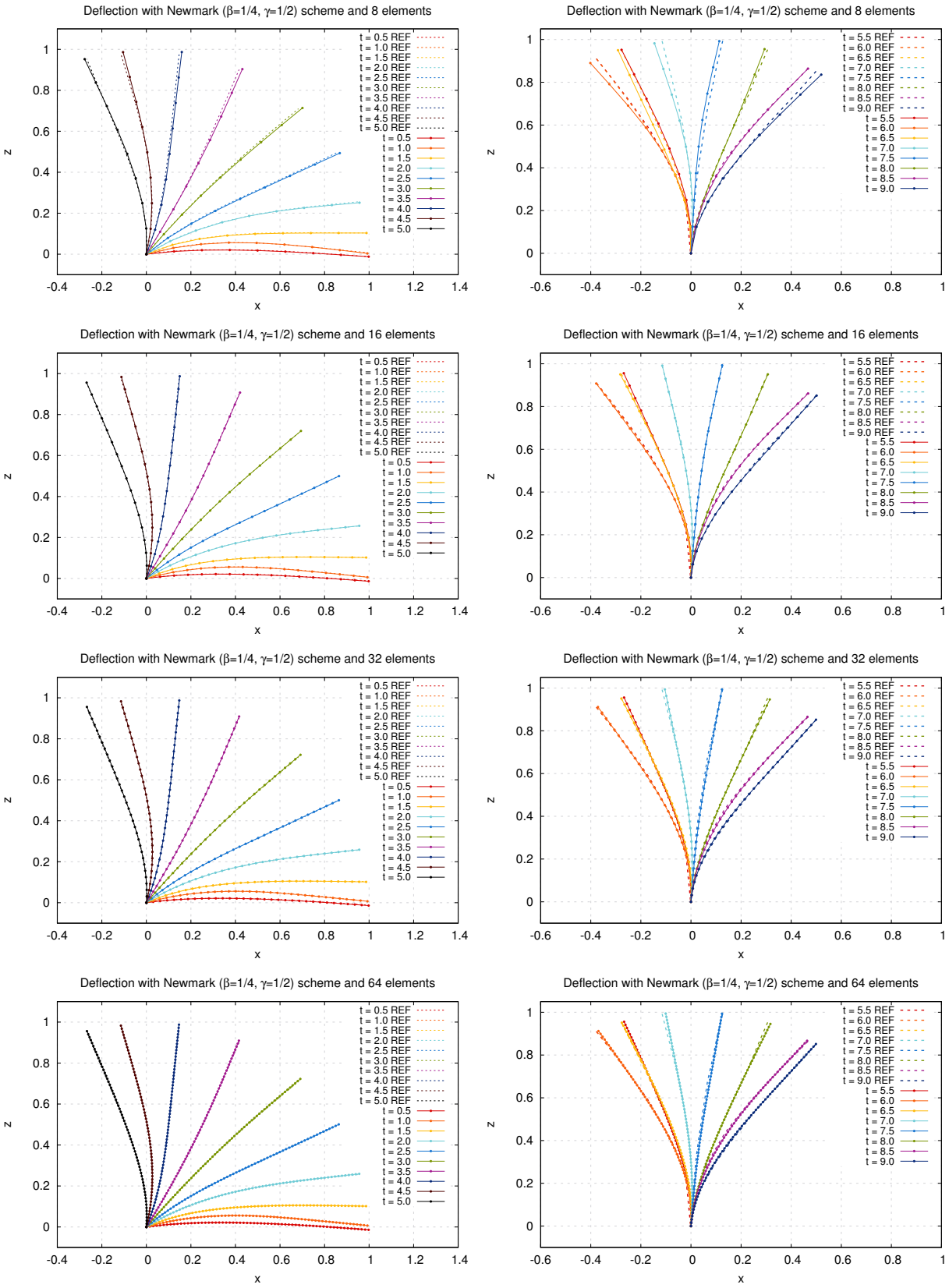

Figure 3.26 Deflections for an increasing number of elements using the Newark scheme with $\beta = 1/4$ and $\gamma = 1/2$, and dt = 1e-5

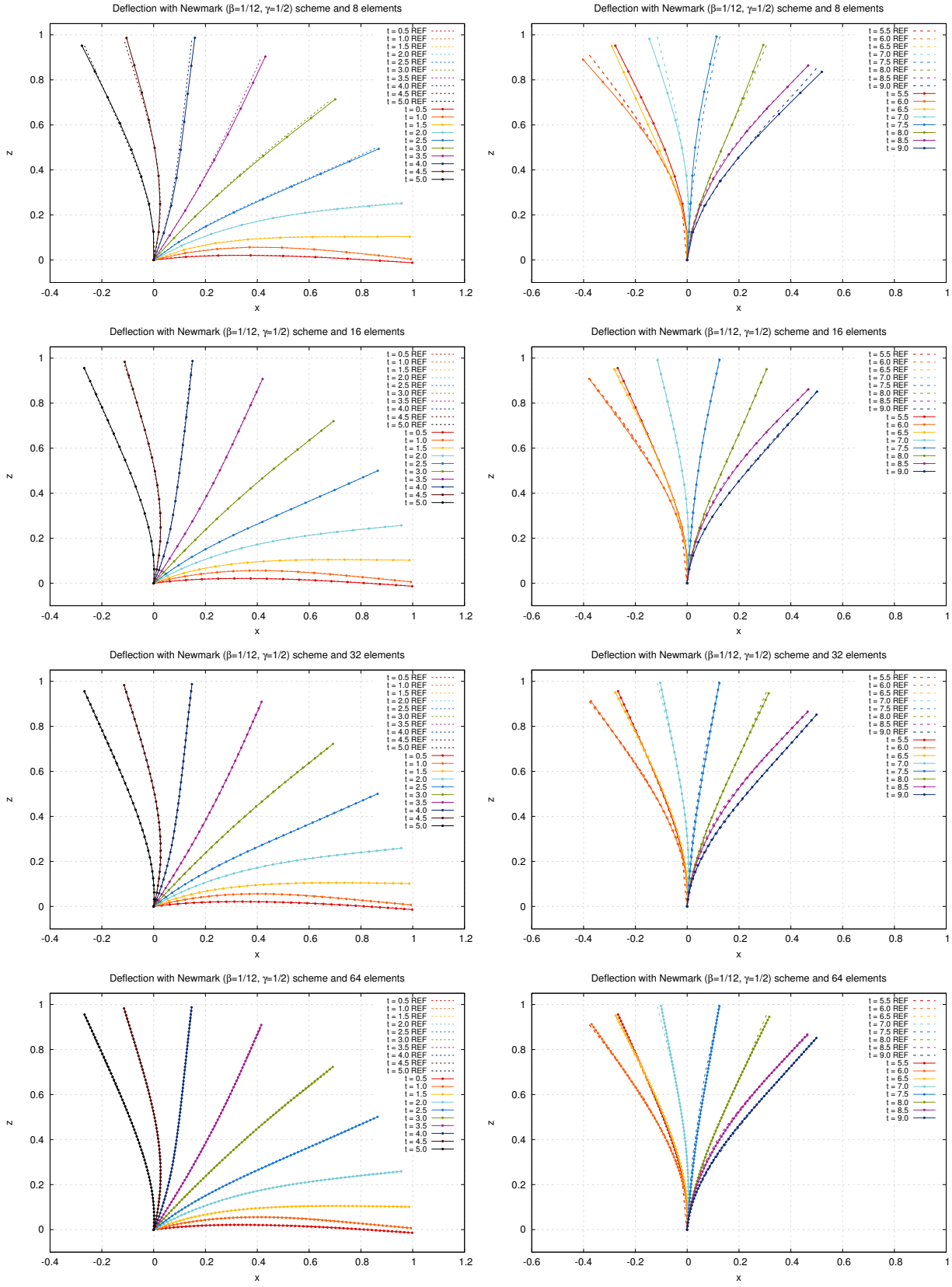

Figure 3.27 Deflections for an increasing number of elements using the Newark scheme with $\beta = 1/12$ and $\gamma = 1/2$, and dt = 1e-5

3.7.2 Time Discretization

Following the spacial discretization, the case is investigated in temporal discretization for the same three schemes. The time steps are decreased by a factor of two, while the error of the computations is measured with the following L_2 norm to provide a comparison basis.

$$L_2 = \sqrt{\sum_{i=0}^{n_{elements}} (u(x_i,t) - u(x_i,t)_{ref})^2} \tag{3.36}$$

The results of this investigation are presented in figure 3.28 and tables 3.14 , 3.15 and 3.16. It can be seen that the explicit and fourth order Newmark schemes required much smaller timesteps than the unconditionally stable second order Newmark scheme in order to meet their stability requirements, as is expected of them. Furthermore, it can be observed in figures 3.29, 3.30 and 3.31, that while the second order Newmark scheme is unconditionally stable, it is not necessarily accurate, as there appear to be large discrepancies when the timestep sizes are too large. On the other hand, the explicit scheme and fourth order scheme provide qualitatively accurate results as soon as their stability requirements are met. The explicit scheme appears to be first order accurate, while the second and fourth order Newmark methods measurably provide their second and fourth orders respectively.

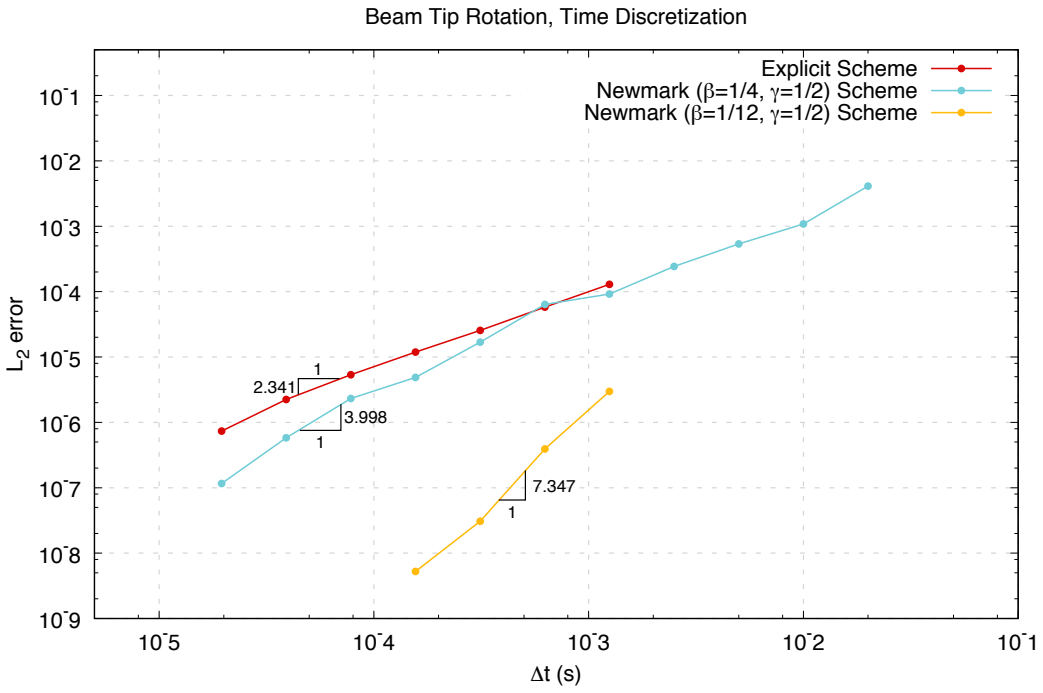

Figure 3.28 Time discretization convergence using the L_2 norm

Table 3.14 Tip displacement using the Explicit scheme

dt	L_2 Error
0.00125000000	0.00012899760578113
0.00062500000	0.00005776864955051
0.00031250000	0.00002548486188188
0.00015625000	0.00001186925320972
0.00007812500	0.00000535843340910
0.00003906250	0.00000223687675003
0.00001953125	0.00000073642956750

Table 3.15 Tip displacement using the Newark scheme with $\beta = 1/4$ and $\gamma = 1/2$

dt	L_2 Error
0.02000000000	0.00410840901065054
0.01000000000	0.00108476005771987
0.00500000000	0.00053541108043441
0.00250000000	0.00024212039642960
0.00125000000	0.00009204453857401
0.00062500000	0.00006370845304287
0.00031250000	0.00001689094111408
0.00015625000	0.00000485610751359
0.00007812500	0.00000231945512644
0.00003906250	0.00000058031655117
0.00001953125	0.00000011596007550

Table 3.16 Tip displacement using the Newark scheme with $\beta = 1/12$ and $\gamma = 1/2$

dt	L_2 Error
0.00125000000	0.00000298067341186
0.00062500000	0.00000039221293469
0.00031250000	0.00000003073879348
0.00015625000	0.00000000523093384

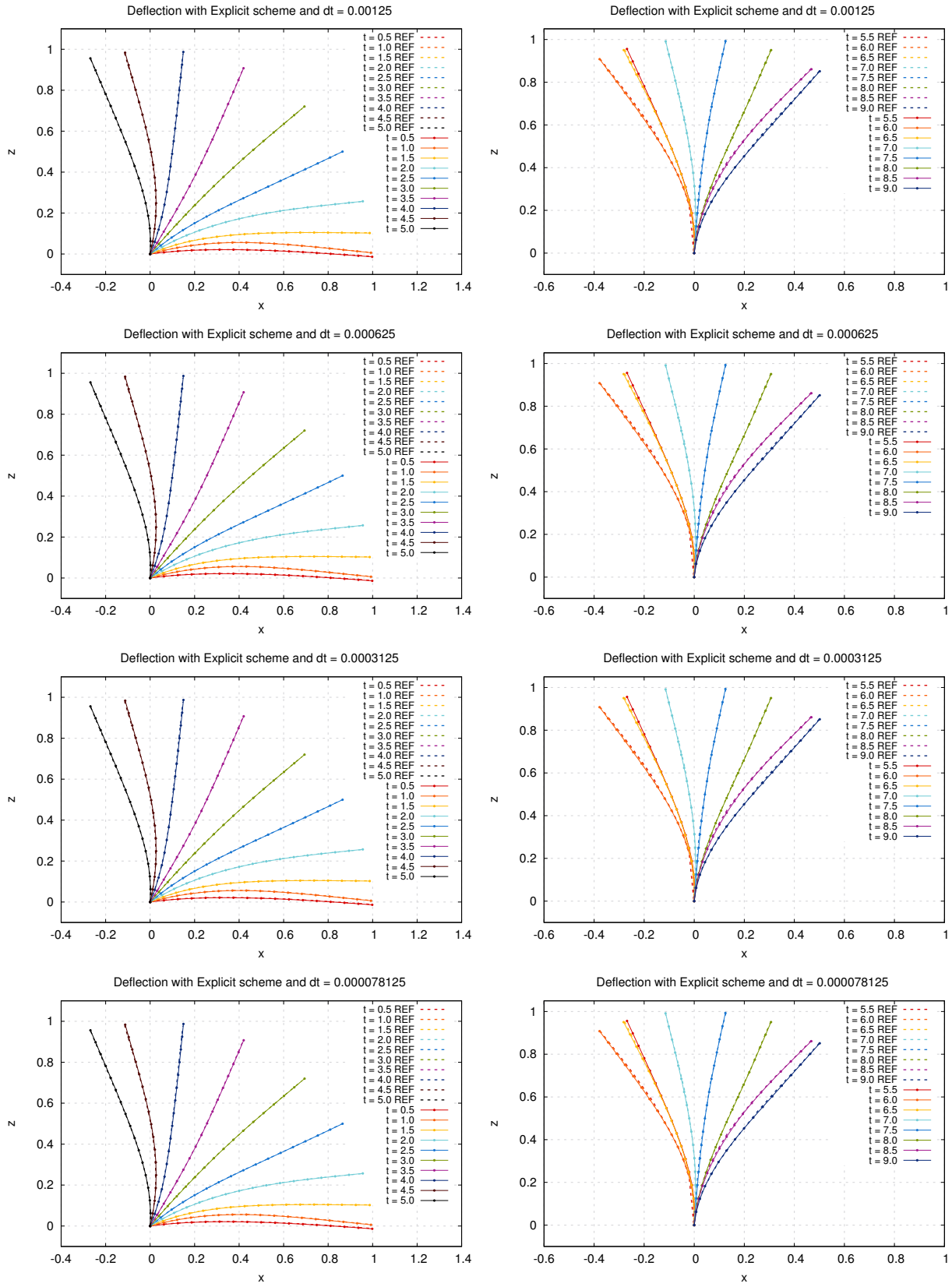

Figure 3.29 Deflections for decreasing timesteps using the Explicit scheme and 16 elements

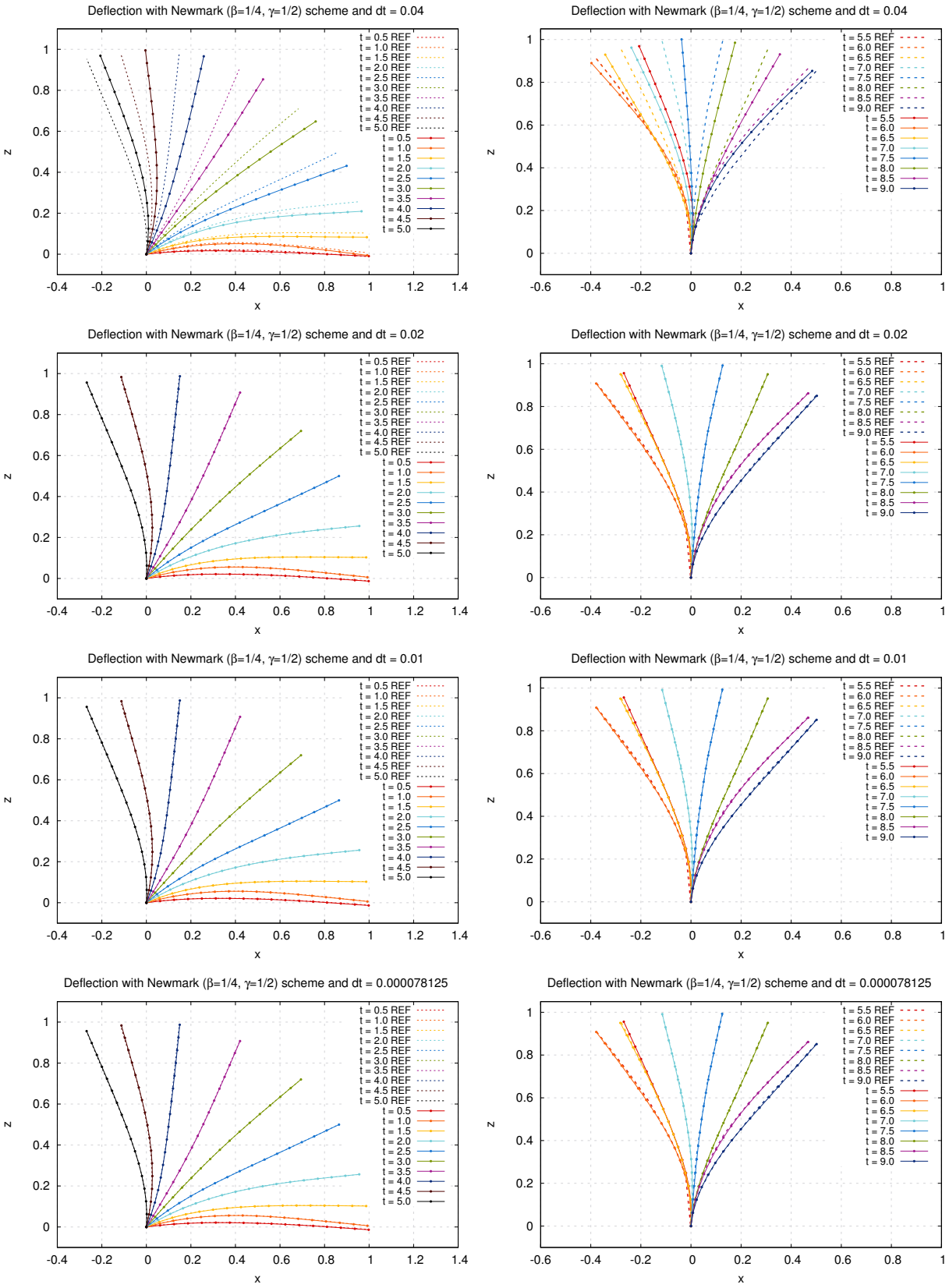

Figure 3.30 Deflections for decreasing timesteps using the Newark scheme with $\beta = 1/4$ and $\gamma = 1/2$ and 16 elements

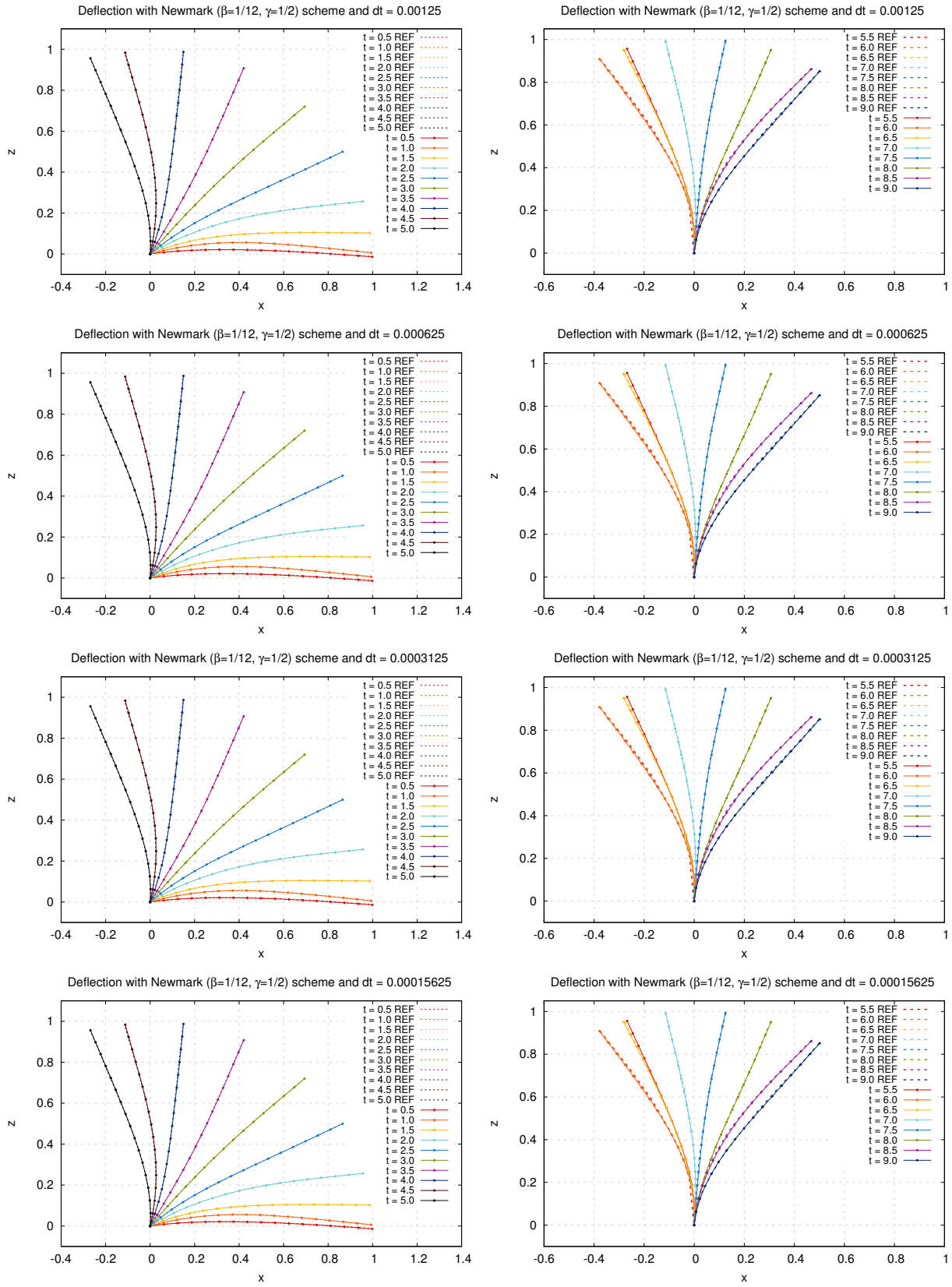

Figure 3.31 Deflections for decreasing timesteps using the Newark scheme with $\beta = 1/12$ and $\gamma = 1/2$ and 16 elements

CHAPTER 4 INVISCID PARTITIONED COUPLING OF FEM AND VLM

In this chapter, the linear Vortex-Lattice method previously presented is combined with a beam model using a partitioned coupling algorithm that was described by Farhat *et al.* (1998) which utilizes the finite element shape functions to perform the coupling interpolations. This interpolation procedure uses a search algorithm and a projection onto the nearest element, the computational cost of which is low in this case because the number of FEM elements remains low during conceptual and preliminary design phases (Figure 1.9).

4.1 Boundary Conditions and Interpolation

The VLM requires that the wing's midplane be discretized as a surface, whereas the FEM beam model produces a topology that is linear. Therefore, a significant mesh mismatch is produced and an interpolation scheme is required to transfer the aerodynamic forces and the structural displacements.

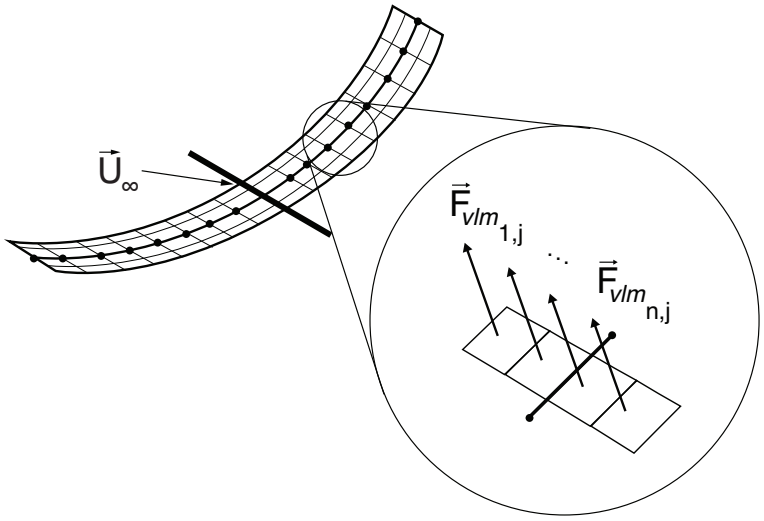

Figure 4.1 Forces to be applied onto the FEM for each column of fluid panels

Furthermore, the fluid forces $\vec{\mathbf{F}}_{vlm_{i,j}}$ are generated at the frontal bound vortex of each vortex ring, itself offset with respect to its panel by a quarter of the panel's chordwise length (figure 4.1), while the displacements of the fluid grid are instead expressed at the four corners of each vortex ring, meaning that two separate interpolation procedures are necessary.

The boundary conditions used on the wet surface Γ to couple the fluid and structure specify that the stresses on the structure σ_s are in equilibrium with the fluid stresses σ_f and the fluid pressure p along the boundary's normal $\vec{\mathbf{n}}$ (equation 4.1), and that the displacements of the structure u_s and fluid u_f must be compatible (equation 4.2). Furthermore, conservation of energy and conservation of loads at the interface is required of the interpolation procedure.

$$\sigma_s \cdot \vec{\mathbf{n}} = -p \cdot \vec{\mathbf{n}} + \sigma_f \vec{\mathbf{n}} \qquad \text{on} \qquad \Gamma \tag{4.1}$$

$$u_s = u_f \qquad \text{on} \qquad \Gamma \tag{4.2}$$

Any interpolation procedure coupling the fluid displacements to the structure displacements can be expressed in the following manner

$$\delta \vec{\mathbf{u}}_f = H \; \delta \vec{\mathbf{u}}_s \tag{4.3}$$

where $\delta \vec{\mathbf{u}}_f$ are the fluid virtual displacements, $\delta \vec{\mathbf{u}}_s$ are the structural virtual displacements and H is an interpolation matrix. The virtual work of the fluid can be expressed as

$$\delta W_f = \vec{\mathbf{F}}_f^{\top} \cdot \delta \vec{\mathbf{u}}_f \tag{4.4}$$

and the structural virtual work as

$$\delta W_s = \vec{\mathbf{F}}_s^{\top} \cdot \delta \vec{\mathbf{u}}_s \tag{4.5}$$

where $\vec{\mathbf{F}}_f$ and $\vec{\mathbf{F}}_s$ are the fluid and structure forces respectively.

Energy is conserved if $\delta W_f = \delta W_s$, which implies through equations 4.3, 4.4 and 4.5 that the following must be satisfied by the interpolation procedure.

$$\vec{\mathbf{F}}_s = H^{\top} \vec{\mathbf{F}}_f \tag{4.6}$$

The displacement at any given point of the wet surface is given by the finite element model as

$$\vec{\mathbf{u}}_s = \sum_{i=1}^{i=n_s} N_i \, \vec{\mathbf{u}}_{s_i} \tag{4.7}$$

where N_i are the shape functions of the individual element nodes, $\vec{\mathbf{u}}_{s_i}$ are the displacement values at the nodes and n_s is the number nodes.

If a set of natural coordinates $\vec{\xi_j}$ is found for a fluid point $\vec{p_{f_j}}$, then the structural displacement can be obtained at that point using the shape functions for that set of natural coordinates on the wet structure Γ_s and the fluid in contact with the structure Γ_f.

$$\vec{\mathbf{u}}_{f_j} = (\vec{p_{f_j}}) = \sum_{i=1}^{i=n_s} N_i(\vec{\xi_\mathbf{j}}) \, \vec{\mathbf{u}}_{s_i} \qquad j \in \Gamma_f, i \in \Gamma_s \tag{4.8}$$

Thus, for this interpolation method, the interpolation matrix terms of equation (4.3) are the structure shape function values for the natural coordinates of each fluid point.

$$H_{i,j} = N_i(\vec{\xi_j}) \qquad j \in \Gamma_f, i \in \Gamma_s \tag{4.9}$$

Similarly, the forces applied onto the structure by the fluid are obtained using the same shape functions for each of the n_f fluid forces.

$$\vec{\mathbf{F}}_{s_i} = \sum_{j=1}^{j=n_f} \vec{\mathbf{F}}_{f_j} N_i(\vec{\xi_j}) \qquad j \in \Gamma_f, i \in \Gamma_s \tag{4.10}$$

The conservative nature of this method is verified in the following manner remembering that the sum of an element's shape functions is 1, thereby demonstrating that the forces acting on the structure are an exact integration of the fluid forces.

$$\sum_{i=1}^{i=n_s} \vec{\mathbf{F}}_{s_i} = \sum_{i=1}^{i=n_s} \sum_{j=1}^{j=n_f} \vec{\mathbf{F}}_{f_j} N_i(\vec{\xi_j}) = \sum_{j=1}^{j=n_f} \vec{\mathbf{F}}_{f_j} \tag{4.11}$$

4.2 Lift Generation

It was previously asserted that Kutta (1902) and Joukowsky (1910) expressed the lift due to circulation as

$$L' = \rho_\infty U_\infty \Gamma \tag{4.12}$$

which in the case of the vortex lattice method having a grid of n_{span} by n_{chord} panels is related to the local circulation $\Gamma_{i,j}$ for each vortex ring (i, j) where $1 \leq i \leq n_{chord}, 1 \leq j \leq n_{span}$ as

$$L = \rho_\infty U_\infty \Gamma_{i,j} \|\vec{\mathbf{dl}}_{i,j}\| \tag{4.13}$$

where the spanwise integration is provided by the magnitude of the bound vortex vector $\vec{\mathbf{dl}}_{i,j}$ formed by the first corner point $\vec{\mathbf{p}_{4_{i,j}}}$ and fourth corner point $\vec{\mathbf{p}_{1_{i,j}}}$ of the vortex ring, with the source of the lift positioned between these two points as shown in figure 4.2.

$$\vec{\mathbf{dl}}_{i,j} = \vec{\mathbf{p}_{4_{i,j}}} - \vec{\mathbf{p}_{1_{i,j}}} \tag{4.14}$$

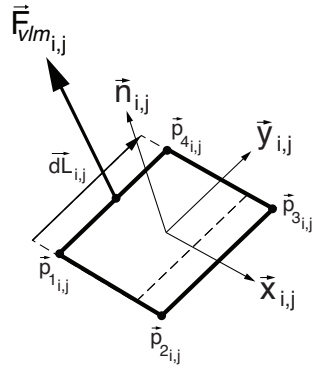

Figure 4.2 Vortex ring topology

By the definition of lift and circulation, the lift vector has to be perpendicular to the far field flow velocity $\vec{\mathbf{U}}_\infty$ and the plane of circulation which has as a normal the vortex panel's $\vec{\mathbf{y}}_{i,j}$ coordinate, which can be approximated by the bound vortex vector to obtain the following expression for the lift vector positioned at the ring's bound vortex center (figure 4.2).

$$\vec{\mathbf{L}}_{i,j} = \rho_\infty \Gamma_{i,j} (\vec{\mathbf{U}}_\infty \times \vec{\mathbf{dl}}_{i,j}) \tag{4.15}$$

4.3 Coupling Algorithm

Projection of the fluid points onto the finite elements provides the natural coordinate ξ for the nearest beam which is used as an interpolation weight to produce a fraction of the loading for the FEM nodes attached to the beam. As shown in figure 4.3, the orthogonal projection of the loading source point p_f onto the beam produces a radius vectors $\vec{\mathbf{r}}_{k,i,j}$ and $\vec{\mathbf{r}}_{k+1,i,j}$ for the two nodes $\vec{\mathbf{n}}_k$ and $\vec{\mathbf{n}}_{k+1}$ of the bar.

$$w_k = N_k(\xi_{i,j}) = \xi_{i,j} \qquad w_{k+1} = N_{k+1}(\xi_{i,j}) = 1 - \xi_{i,j} \tag{4.16}$$

This interpolation weight is used to transmit kinematically equivalent loads to the nearest element nodes, which in the case of a linear VLM means transforming the force produced by each panel between its two frontal nodes into an equivalent pair of forces ($\vec{\mathbf{F}}_{fem_k}$ and $\vec{\mathbf{F}}_{fem_{k+1}}$) and moments ($\vec{\mathbf{M}}_{fem_k}$ and $\vec{\mathbf{M}}_{fem_{k+1}}$) at the extremities of the nearest beam element. The same interpolation method is used to transmit the displacements of the FEM model to the individual nodes of the VLM model. The load and displacement interpolation processes are detailed in algorithms 5 and 6.

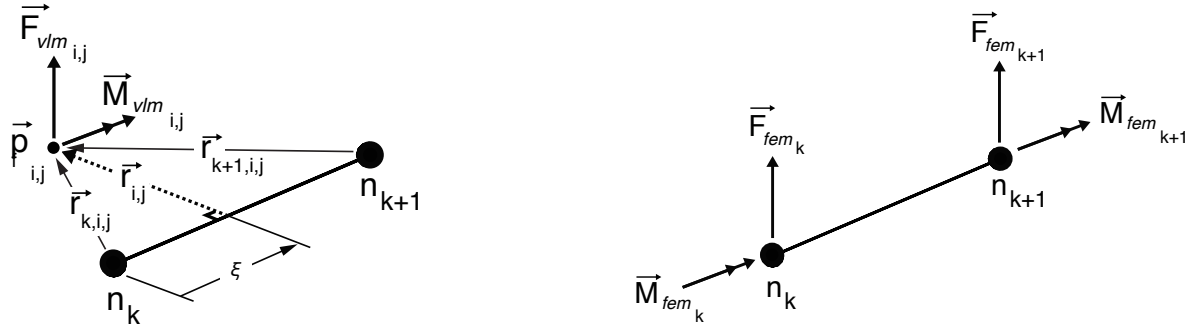

Figure 4.3 Projection onto beam element (left) and loads applied onto the beam (right)

The partitioned methodology requires that the individual models converge to a solution and that the boundary conditions they share converge as well. This is achieved by iterations with the forces being provided by the aerodynamic model, while the displacements are provided by the structure. This procedure is interrupted when either the relative error on the lift coefficient or the relative error on the potential energy has met a predetermined tolerance criterion. If the Cauchy number is too high and thus the aerodynamic stiffness significantly

greater than the structural stiffness, stability issues appear that prevent the convergence of the coupling. This is remedied by adding two relaxation factors α_{forces} and α_{disp}, one for the displacements and one for the forces. The flowchart of the coupling procedure is presented in figure 4.4 where the variation of the potential energy of the structure E_p is used as a criteria to end the iteration loop.

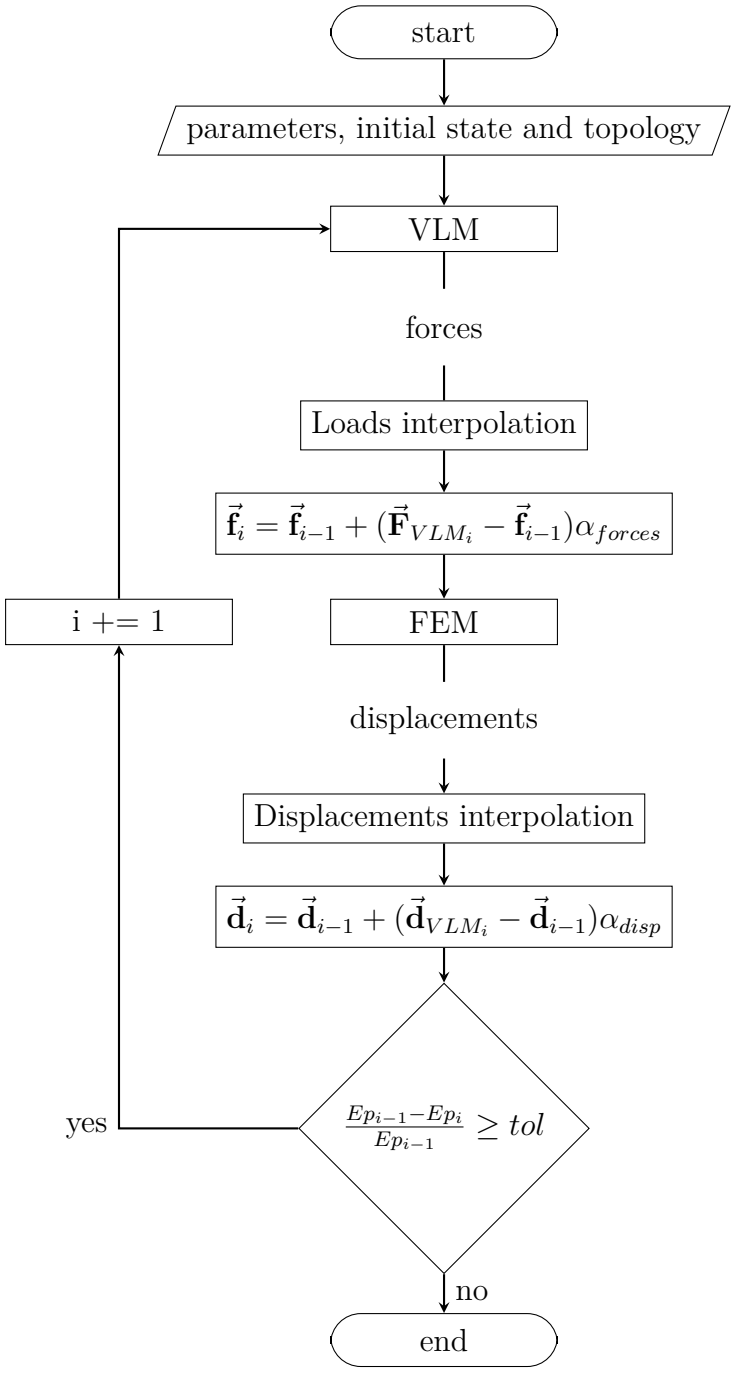

Figure 4.4 Inviscid Coupling

Algorithm 5 Inviscid Coupling Algorithm - Load Interpolation

1: **for** every span-wise column of vortex rings j **do**

2: **for** every chord-wise row of vortex rings i **do**

3: Obtain the vortex-ring's force vector and load application point

$$\vec{\mathbf{Ff}}_{i,j} = \vec{\mathbf{F}}_{vlm_{i,j}} = \vec{\mathbf{L}}_{i,j} \qquad \vec{\mathbf{p}_{f_{i,j}}} = (\vec{\mathbf{p}_{4_{i,j}}} + \vec{\mathbf{p}_{1_{i,j}}})/2$$

4: Find the closest finite element

5: Obtain the rotation matrices between the deformed and undeformed nodes

$$\mathbf{R_{n_k}} = R(\overset{\circlearrowleft}{q_k}') \qquad \mathbf{R_{n_{k+1}}} = R(\overset{\circlearrowleft}{q_{k+1}}')$$

6: Project the fluid point $\vec{\mathbf{p}_{f_{i,j}}}$ onto the finite element

$$\vec{\mathbf{d}}_k = \vec{\mathbf{n_{k+1}}} - \vec{\mathbf{n_k}} \qquad \vec{\mathbf{p}_{f_{i,j}}}' = \frac{\vec{\mathbf{d}}_k}{\|\vec{\mathbf{d}}_k\|}(\vec{\mathbf{p}_{f_{i,j}}} \cdot \frac{\vec{\mathbf{d}}_k}{\|\vec{\mathbf{d}}_k\|}) \tag{4.17}$$

7: Find the fluid point's natural coordinates $\vec{\xi_{\mathbf{i,j}}}$ in that finite element

$$\xi_{i,j} = \frac{\|\vec{\mathbf{p}_{f_{i,j}}}'\|}{\|\vec{\mathbf{d}}_k\|} \tag{4.18}$$

8: Obtain the interpolation weight from the element's shape functions

$$w_{k,i,j} = N_k(\xi_{i,j}) = \xi_{i,j} \qquad w_{k+1,i,j} = N_{k+1}(\xi_{i,j}) = 1 - \xi_{i,j} \tag{4.19}$$

9: Obtain a weighed equivalent load at each receiving node that is rotated to remove deformation

$$\vec{\mathbf{r}}_{k,i,j} = \vec{\mathbf{p}_{f_{i,j}}} - \vec{\mathbf{n}}_k \tag{4.20}$$

$$\vec{\mathbf{r}}_{k+1,i,j} = \vec{\mathbf{p}_{f_{i,j}}} - \vec{\mathbf{n}}_{k+1} \tag{4.21}$$

$$\vec{\mathbf{Fs}}_{k,i,j} = w_{k,i,j} * \mathbf{R_{n_k}}\vec{\mathbf{Ff}}_{i,j} \tag{4.22}$$

$$\vec{\mathbf{Fs}}_{k+1,i,j} = w_{k+1,i,j} * \mathbf{R_{n_{k+1}}}\vec{\mathbf{Ff}}_{i,j} \tag{4.23}$$

$$\vec{\mathbf{Ms}}_{k,i,j} = w_{k,i,j} * \mathbf{R_{n_k}}(\vec{\mathbf{r}}_{k,i,j} \times \vec{\mathbf{Ff}}_{i,j}) \tag{4.24}$$

$$\vec{\mathbf{Ms}}_{k+1,i,j} = w_{k+1,i,j} * \mathbf{R_{n_{k+1}}}(\vec{\mathbf{r}}_{k+1,i,j} \times \vec{\mathbf{Ff}}_{i,j}) \tag{4.25}$$

10: **end for**

11: **end for**

Algorithm 6 Inviscid Coupling Algorithm - Displacement Interpolation

1: **for** every span-wise column of vortex rings j **do**

2: **for** every chord-wise row of vortex rings i **do**

3: Find the closest finite element

4: Project the fluid point $\vec{\mathbf{p}_{f_{i,j}}}$ onto the finite element

$$\vec{\mathbf{d}}_k = \vec{\mathbf{n_{k+1}}} - \vec{\mathbf{n_k}} \tag{4.26}$$

$$\vec{\mathbf{p}_{f_{i,j}}}' = \frac{\vec{\mathbf{d}}_k}{\|\vec{\mathbf{d}}_k\|}(\vec{\mathbf{p}_{f_{i,j}}} \cdot \frac{\vec{\mathbf{d}}_k}{\|\vec{\mathbf{d}}_k\|}) \tag{4.27}$$

5: Find the fluid point's natural coordinates $\vec{\xi_{\mathbf{i,j}}}$ in that finite element

$$\xi_{i,j} = \frac{\|\vec{\mathbf{p}_{f_{i,j}}}'\|}{\|\vec{\mathbf{d}}_k\|} \tag{4.28}$$

6: Obtain the interpolation weight from the element's shape functions

$$w_{k,i,j} = N_k(\xi_{i,j}) = \xi_{i,j} \qquad w_{k+1,i,j} = N_{k+1}(\xi_{i,j}) = 1 - \xi_{i,j} \tag{4.29}$$

7: Obtain the displacement and rotation at the fluid point's natural coordinate using equation 3.10

$$\vec{\mathbf{u}}_{i,j} = \vec{\mathbf{u}}_k(1-\xi) + \vec{\mathbf{u}}_{k+1}\xi$$

$$\overset{\circlearrowleft}{q}_{i,j} = \overset{\circlearrowleft}{q}_k \frac{sin(1-\xi)\theta}{sin\theta} + \overset{\circlearrowleft}{q}_{k+1} \frac{sin\xi\theta}{sin\theta} \qquad \text{where} \qquad \theta = \frac{\overset{\circlearrowleft}{q}_k \cdot \overset{\circlearrowleft}{q}_{k+1}}{|\overset{\circlearrowleft}{q}_k||\overset{\circlearrowleft}{q}_{k+1}|}$$

8: Turn the structure's displacement and rotation into a single displacement

$$\vec{\mathbf{r}} = \vec{\mathbf{p}_{f_{i,j}}} - (\vec{\mathbf{n_{k+1}}}(1-\xi) + \vec{\mathbf{n_{k+1}}}\xi) \tag{4.30}$$

$$\vec{\mathbf{dr}} = R(\overset{\circlearrowleft}{q}_{i,j})\ \vec{\mathbf{r}} - \vec{\mathbf{r}} \tag{4.31}$$

$$\vec{\mathbf{d}} = \vec{\mathbf{u}} + \vec{\mathbf{dr}} \tag{4.32}$$

9: **end for**

10: **end for**

4.4 Investigation of Smith's Wing

Smith *et al.* (2001) made a comparative study on a wing in the subsonic regime to compare three aeroelastic solution methods using geometrically exact beam elements. The first was a panel method combined with a nonlinear structural model, the second and third combine a higher fidelity Euler solver (ENS3DAE) in three-dimensions with a linear or nonlinear structural model. This provides a fair comparison basis for a subsonic method applied to wings experiencing large deflections.

The wing is straight, untapered and untwisted and is an extrusion of a NACA0012 airfoil flying at 25 m/s at 20000m of altitude with the following geometric and mechanical properties.

Property	Value
Span	32 m
Chord	1 m
Spanwise elastic axis	0.5c
Bending Rigidity	$2 \cdot 10^4 Nm^2$
Torsional Rigidity	$5 \cdot 10^6 Nm^2$

4.4.1 Modeling

This rectangular wing is modeled by a rectangular VLM grid consisting of 100x12 vortex-ring panels with bar elements positioned at the elastic axis, which is considered to be midchord. The FEM node which is positioned at the root of the wing is fixed. The VLM panel grid and the FEM model is shown schematically in figure 4.5.

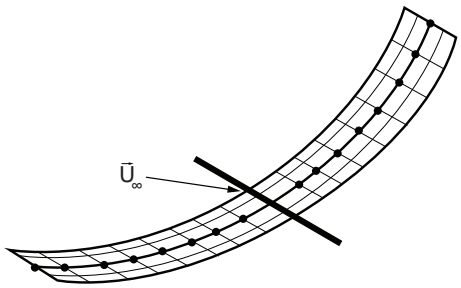

Figure 4.5 VLM panel grid with FEM beam model positioned at midchord

4.4.2 Numerical Results

The computational results published by Smith *et al.* (2001) are shown in figures 4.6 through 4.8 with the lift nondimensionalized using the two-dimensional lift curve slope. There appears to be a discrepancy between the results of Eulerian solver and the Panel Method, whereas it is expected that in this subsonic regime both would produce very similar results. The source of this discrepancy is not further investigated and the verification is done against the Eulerian curves, as is also done by Murua *et al.* (2012).

Linear Solutions

An initial estimate of the deflected geometry is obtained by considering linear deflections of the wing, the results for which are presented in figures 4.6 using 100 bar elements. It is apparent that the deflections along the z axis are exaggerated, as they are 16% and 18% above the Euler nonlinear solution found by Smith for angles of attack of 2 and 4 degrees respectively. This is produced by the linearly deforming wing because the beam structure is not constrained to maintain its length causing the area of the lifting surface to increase. The effect of this elongation on the lift distribution can be noted in figures 4.6 where it can be seen that the lift is significantly increased at the tip of the wing when compared with Smith's computations. These results disagree with Smith's linear results, which suggests that his coupling maintains lifting surface area. Finally, it can be seen that for an angle of attack of 2 degrees the linear results match very well with the nonlinear results obtained by Smith *et al.* (2001) using a panel method, which is unexpected.

Nonlinear Solutions

Figures 4.7 and 4.8 present the nonlinear aeroelastic solutions using 50 bar elements obtained with combinations of force following (FF) and geometric stiffening (GS) to study their impact on the aeroelastic solution. Both the deflections and lift distributions agree very well with Smith's Euler nonlinear computations, whereas this is not the case for the twist. It is notable that the deflections are very large, as they are over 30% for an angle of attack of 4 degrees, whereas even Smith's twist values are smaller in magnitude, suggesting that the majority of the work done by the aerodynamic forces is directed towards the deflection. For both an angle of attack of 2 degrees and 4 degrees, geometric stiffening appears to have a negligible effect on the solutions that are found. However, there is a difference of 3.1% to 5.0 % between the deflections found with force following and without, with force following having a slightly beneficial impact on the aeroelastic solution.

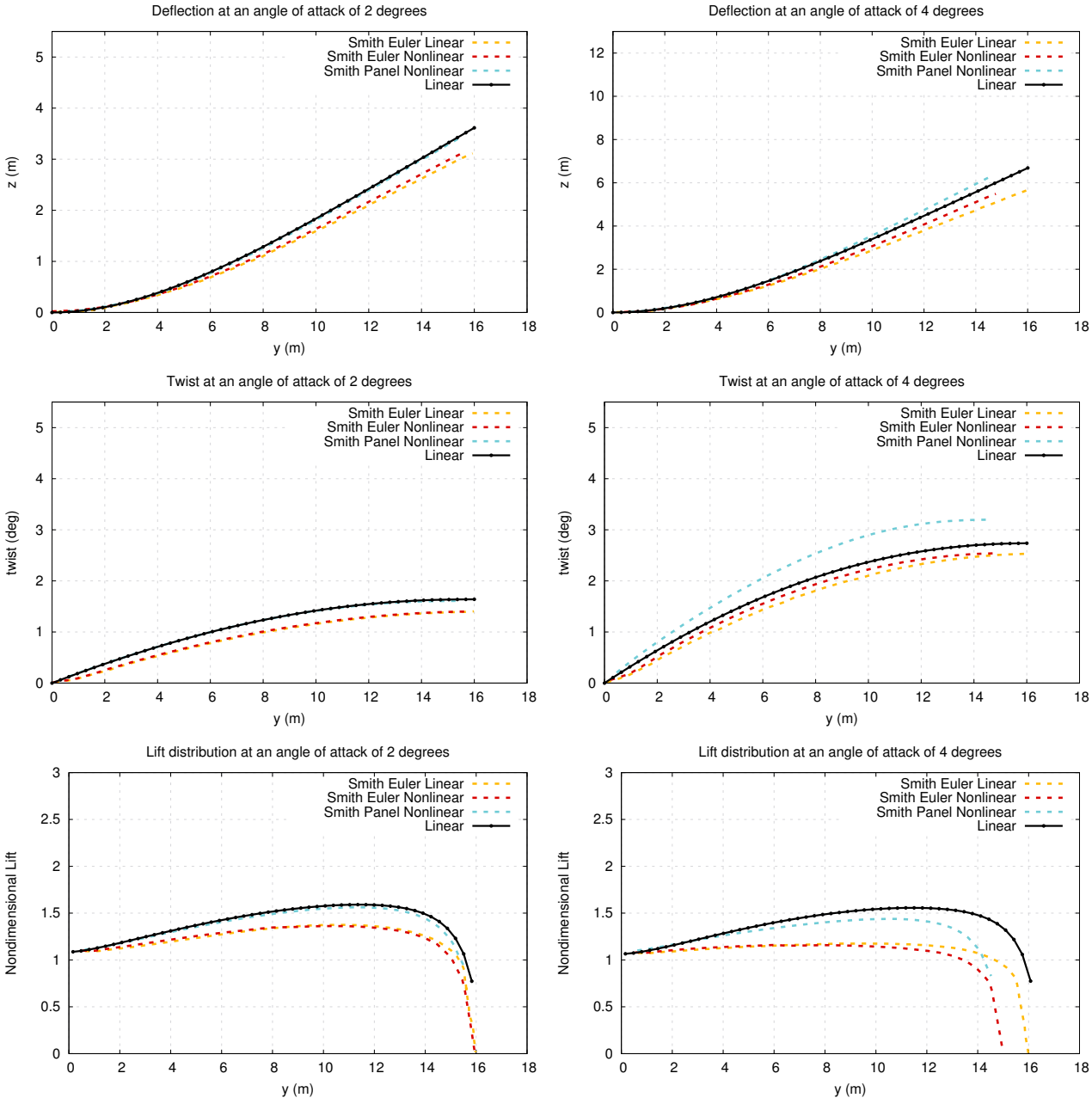

Figure 4.6 Smith wing linear aeroelastic solution for angles of attack of 2 and 4 degrees

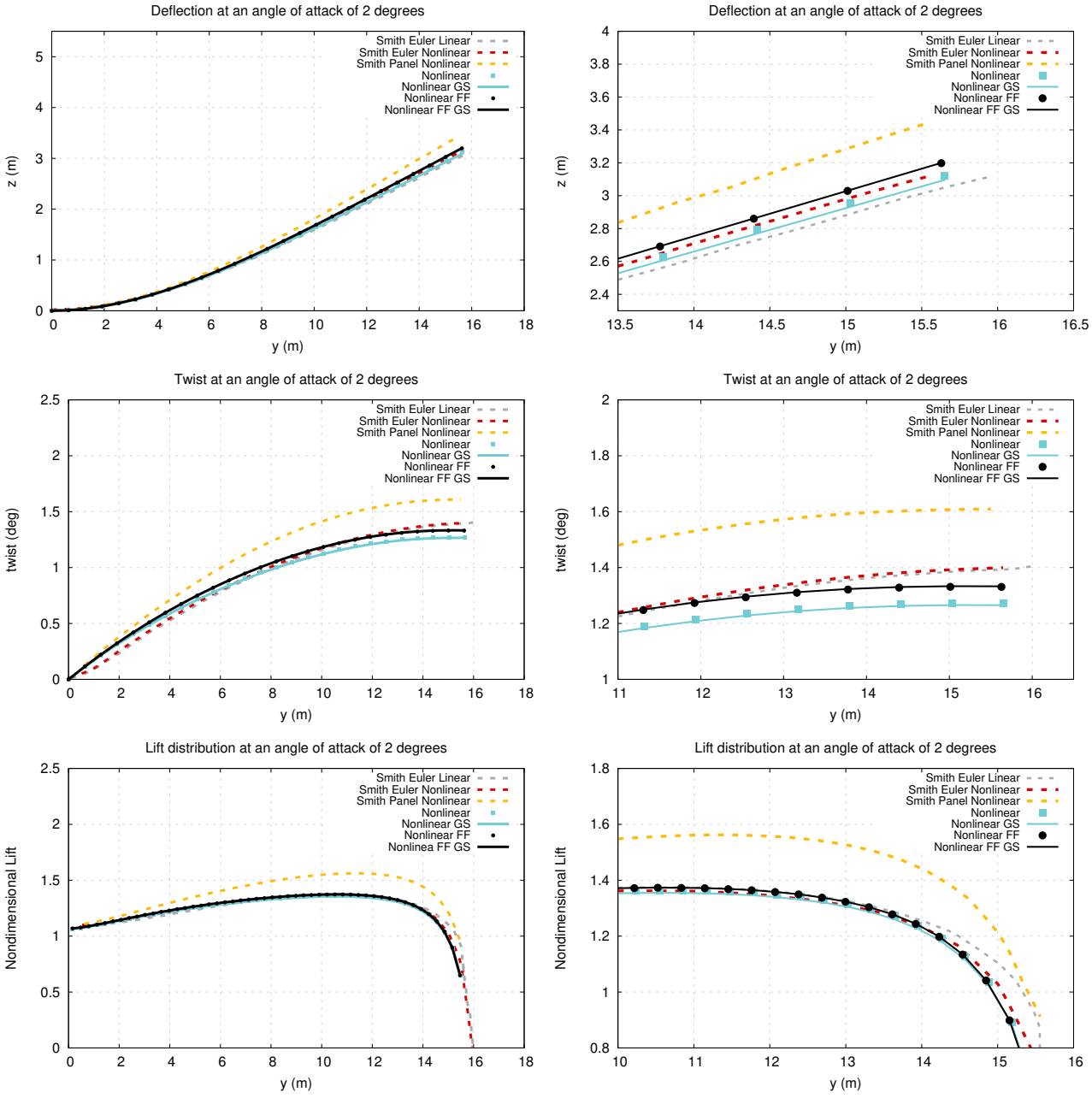

Figure 4.7 Smith wing nonlinear aeroelastic solution for an angle of attack of 2 degrees

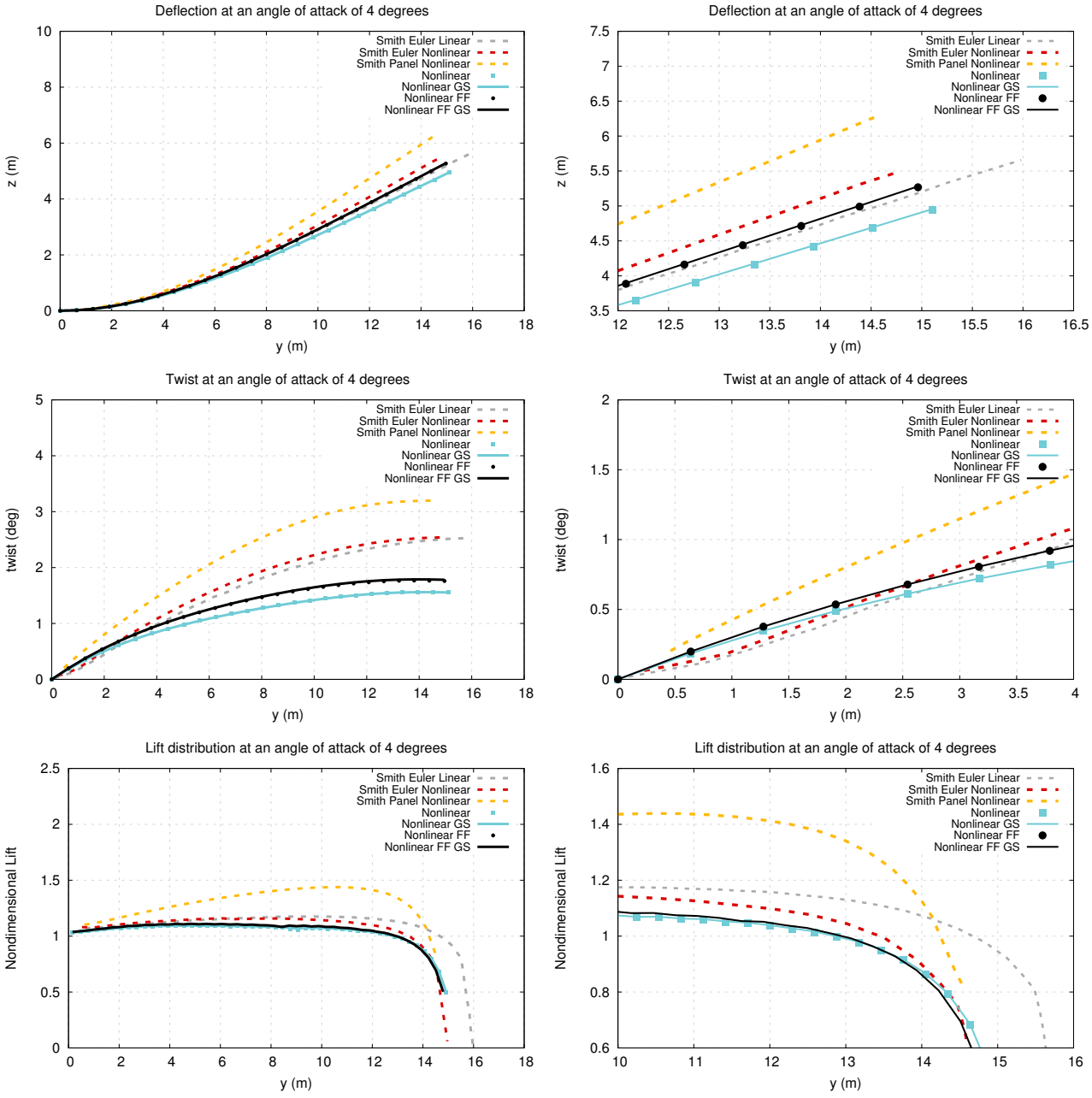

Figure 4.8 Smith wing nonlinear aeroelastic solution for an angle of attack of 4 degrees

Load stepping

In order to verify the accuracy of the integration of the loads, a discretization study was conducted by varying the number of loading steps from 2 to 64, using the latter as a reference to measure relative error. The results of this study are presented in table 4.1 and convey that increasing the number of loading steps has an effect and in fact, improves the accuracy of the converged solution superlinearly.

Table 4.1 Nonlinear tip displacement against load steps at alpha 2 using 50 bars

steps	dx (m)	Error (%)	dz (m)	Error (%)
2	-0.16696837838432191	2.9748	3.16988931788582295	2.21934
4	-0.16960037690171159	1.4454	3.20701974062128281	1.07399
8	-0.17092425253414939	0.6761	3.22558291677609388	0.50137
16	-0.17158883650185361	0.2899	3.23487421198424219	0.21477
32	-0.17192223464828790	0.0962	3.23953033689622583	0.07114
64	-0.17208781562422559	-	3.24183681328277506	-

Space Discretization

Additionally, a space discretization study was conducted by increasing the number of bar elements from 2 to 64, using the latter as a reference to compute relative error. The results are presented in table 4.2 and figures 4.9. While the partitioned scheme is loosely coupled, it provides in effect a strongly coupled solution due to the many fluid and structure iterations, which end once a stable aeroelastic solution is found using conservative interpolation. Despite this and the use of a second order interpolation algorithm, the results demonstrate that the accuracy in space is of order 1. This can potentially be due to the order of the Vortex Lattice Method, which may reduce the order of the coupled system.

Table 4.2 Nonlinear tip displacement at alpha 2 using an increasing number of bars

nelements	dx (m)	Error (%)	ry (rad)	Error (%)
2	-0.12878129972759919	20.1826	0.02515537085252012	14.1404
4	-0.16907375585794110	4.7901	0.02481338131050547	12.5887
8	-0.17034414741743720	5.5775	0.02334094666205492	5.9076
16	-0.16623761198504819	3.0323	0.02256808929213915	2.4008
32	-0.16313823003539499	1.1113	0.02220828986390578	0.7683
64	-0.16134507167267059	-	0.02203896087771123	-

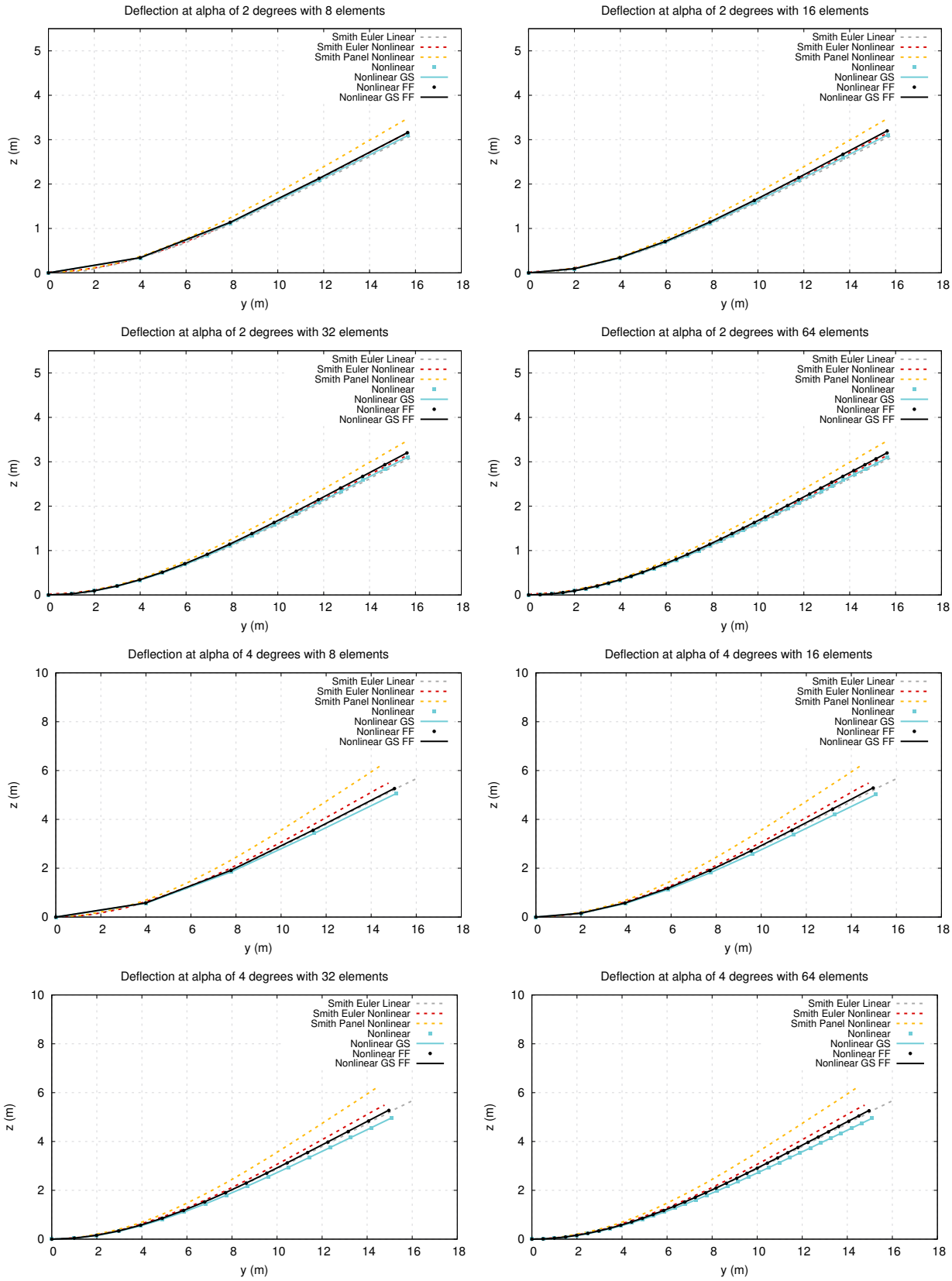

Figure 4.9 Smith wing nonlinear aeroelastic solution for angles of attack of 2 and 4 degrees for a varying number of bar elements

4.4.3 Discussion

The results convincingly convey that the aeroelastic framework produces reliable static aeroelastic deflections in the subsonic regime when compared with established tools and that the vortex-lattice method compares very well to Eulerian three-dimensional computational fluid dynamics at this subsonic airspeed, whilst having a computational cost that is several orders of magnitude lower.

For structural considerations, the results demonstrate that it is imperative to use a nonlinear structural model, as linear models stretch the aerodynamic surface producing additional unphysical lift. Additionally, force following and load stepping are beneficial for such highly deflected high aspect ratio wings, while there is not enough compression or tension in the bars to produce any geometric stiffening.

Once these conditions are factored in, the coupled aeroelastic solutions produce deflections and lift distributions that compare very well with the literature, while the twist that is obtained shows a discrepancy for an angle of attack of four degrees, but compares well at an angle of attack of two degrees.

As far as the coupling procedure is concerned, it was found that roughly 30 to 50 iterations were needed to get below an error tolerance of $1e^{-8}$ on the potential energy of the structure when using a relaxation factor of 0.2 on the displacements and the forces to guarantee the stability of the solution procedure. Furthermore, despite the use of a strongly coupled second order methodology, it was found that the coupled system has first order accuracy in space, which may be explained by the use of the low fidelity vortex-lattice method reducing the overall order of the system.

CHAPTER 5 VISCOUS PARTITIONED COUPLING OF FEM AND 2.5D NLVLM

In this chapter, the method used in the previous chapter is extended to include viscous effects through an additional coupling with 2.5D RANS sectional data that is performed using a modified version of the alpha coupling presented by Parenteau (2016) to take into account deflections.

It is assumed that the structure's dominant modes are adequately represented by two-noded beams having bending, torsion and traction degree of freedoms. Due to the low number of elements that this approach requires, the wing deformations are obtained at a similar computational cost as the loads provided by the VLM method.

5.1 Interpolation and Boundary Conditions

The interpolation procedure and shared boundary operate in the same way as in chapter 4 apart from the forces that are extracted from the aerodynamic model. The 2.5D NL-VLM has the ability to provide the flow field around the vortex rings. Rather than to integrate the flow field in the coupling procedure, it is chosen to integrate the sectional data in the RANS solver in order to obtain the lift, drag and moment coefficients. These are expressed then as a force and a moment at the quarter chord of each spanwise column of vortex rings and are in effect replacing the forces obtained by the linear VLM, as shown in figure 5.1.

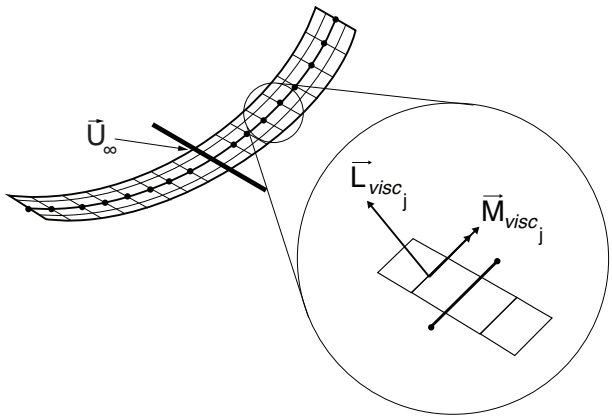

Figure 5.1 Viscous loads to be applied onto the FEM for each column of vortex rings

Having obtained the sectional aerodynamic coefficients C_l, C_d and C_m for a vortex column, it is necessary to dimensionalize them to the parameters of the problem and to provide the loads with appropriate directions. Considering that the dynamic pressure is $\frac{q_\infty}{2}\|\vec{\mathbf{U}}_\infty\|$, the viscous lift, viscous moment and viscous drag are expressed as

$$\vec{\mathbf{L}}_{visc_j} = C_{l_{visc}} q_\infty C_j (\vec{\mathbf{U}}_\infty \times \vec{\mathbf{dl}}_{0,j}) \tag{5.1}$$

$$\vec{\mathbf{D}}_{visc_j} = C_{d_{visc}} q_\infty C_j \, \|\vec{\mathbf{dl}}_{0,j}\| \, \vec{\mathbf{U}}_\infty \tag{5.2}$$

$$\vec{\mathbf{M}}_{visc_j} = C_{m_{visc}} q_\infty C_j^2 \, \vec{\mathbf{dl}}_{0,j} \tag{5.3}$$

where C_j is the chord of the wing at that station, q_∞ the density and $\vec{\mathbf{U}}_\infty$ the freestream velocity.

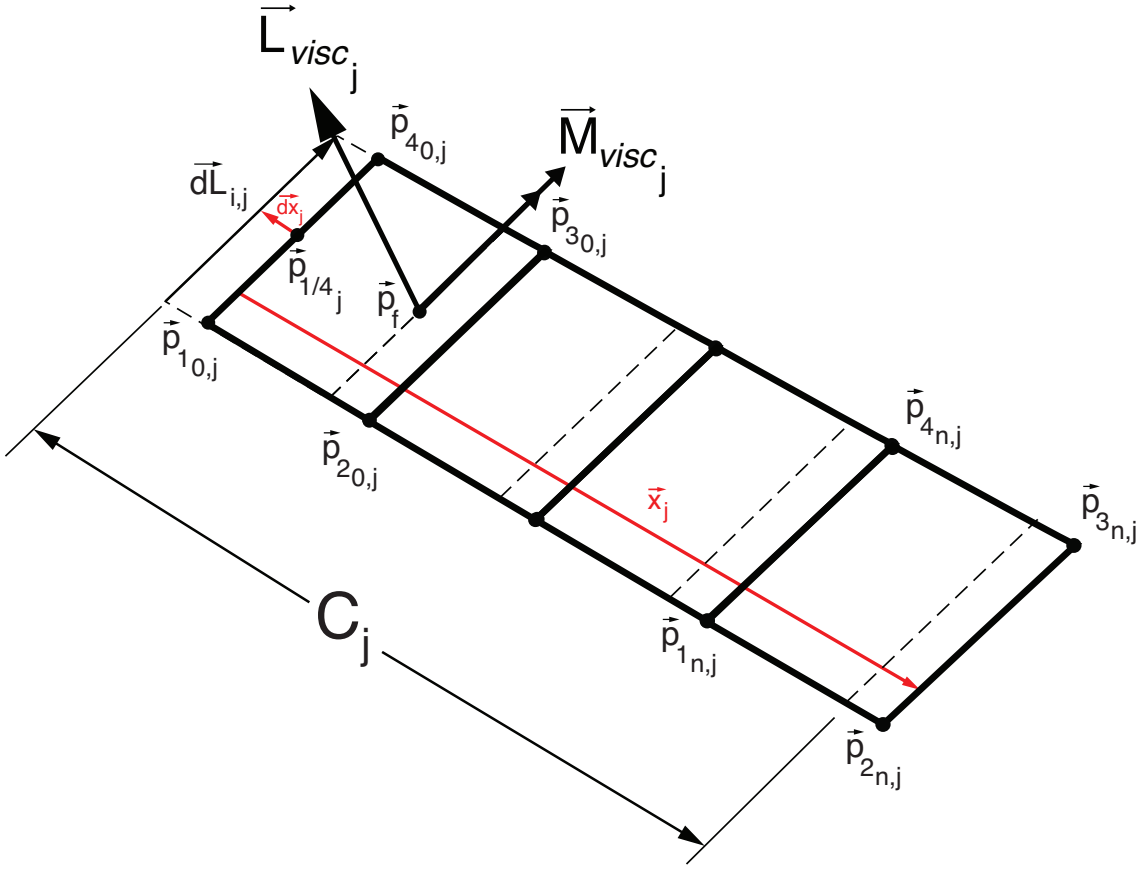

Figure 5.2 Vortex column topology

The point of application of these viscous forces has to be aligned with the viscous airfoil quarter chord, which is computed by first finding the middle point of the bound vortex ring $\vec{\mathbf{p}}_{1/4_j}$, then removing a quarter of a vortex panel chordwise length $\vec{\mathbf{dx}}_j$ and adding a quarter of the chord along a direction going from the leading edge to the trailing edge of the vortex rings $\vec{\mathbf{x}}_j$. These are computed according to equations 5.4 through 5.7.

$$\vec{\mathbf{p}}_{1/4_j} = (\vec{\mathbf{p}}_{1_{0,j}} + \vec{\mathbf{p}}_{4_{0,j}})/2 \tag{5.4}$$

$$\vec{\mathbf{dx}}_j = (\vec{\mathbf{p}}_{2_{0,j}} - \vec{\mathbf{p}}_{1_{0,j}})/8 + (\vec{\mathbf{p}}_{3_{0,j}} - \vec{\mathbf{p}}_{4_{0,j}})/8 \tag{5.5}$$

$$\vec{\mathbf{x}}_j = (\vec{\mathbf{p}}_{2_{n,j}} - \vec{\mathbf{p}}_{1_{0,j}})/2 + (\vec{\mathbf{p}}_{3_{n,j}} - \vec{\mathbf{p}}_{4_{0,j}})/2 \tag{5.6}$$

$$\vec{\mathbf{p}_{f_j}} = \vec{\mathbf{p}}_{1/4} - \vec{\mathbf{dx}} + \frac{C_j \vec{\mathbf{x}}_j}{\|\vec{\mathbf{x}}_j\|} \tag{5.7}$$

5.2 Coupling Algorithm

Starting with the partitioned coupling algorithm that was developed in chapter 4, an additional coupling is provided by modifying the alpha coupling developed by Parenteau (2016) which implicitly assumed that the VLM mesh will remain planar by using the angle of attack of the aircraft in the sectional coupling procedure. As the wing deforms, the local angle of attack will deviate from this value. As an example to consider, if the angle of attack is 0, but the sideslip is not 0, then the undeflected inboard panels should generate no lift, while deflected outboard panels should generate lift due to the presence of a local angle of attack stemming from the sideslip.

Using the vertex numbering used by Katz and Plotkin (1991), a local panel coordinate x can be obtained.

$$\vec{\mathbf{x}}_{panel} = \frac{1}{2}((\vec{\mathbf{p}_3} - \vec{\mathbf{p}_4}) + (\vec{\mathbf{p}_2} - \vec{\mathbf{p}_1})) \tag{5.8}$$

Using this coordinate that can be computed and stored for each panel, the local angle of attack of each panel $\alpha_{3D_{local}(i,j))}$ can be computed using the panel's normal vector $\vec{n}$ and the airflow vector $\vec{U_\infty}$.

$$\alpha_{3D_{local}}(i,j) = tan^{-1}(\frac{\vec{\mathbf{U}_\infty} \cdot \vec{\mathbf{n}}(i,j)}{\vec{\mathbf{U}_\infty} \cdot \vec{\mathbf{x}}(i,j)}) \tag{5.9}$$

The sectional local angle of attack can then obtained by using the average of the chordwise

local angles of attack as follows

$$\alpha_{3D_{local}}(i) = \sum_{j=1}^{n_{chord}} \alpha_{3D_{local}(i,j))} \tag{5.10}$$

The term α_{3D} can then be replaced by the local angle of attack $\alpha_{3D_{local}}(i)$ to form the following algorithm that generalizes the method to swept flexible wings.

Algorithm 7 Coupling algorithm for flexible swept 2.5D RANS CFD data

1: Solve the VLM to find the $Cl_{inviscid}$ of each section.
2: **for** Every Span-Wise Section i **do**
3: Compute the section's effective angle of attack α_e, taking into account the wing's angle of attack α_{3D} and the section's angle of attack correction α_{2D}:

$$\alpha_e(i) = \frac{Cl_{inviscid}(i)}{2\pi} - \alpha_{2D}(i)cos(\phi) + \alpha_{3D_{local}}(i) \tag{5.11}$$

4: Obtain the viscous lift at the effective angle of attack by interpolating the sectional viscous data:
$\alpha_e(i) \Rightarrow Cl_{visc}(\alpha_e(i))$
5: Obtain the section's angle of attack correction α_{2D}:
$\alpha_{2D}(i) = \alpha_{2D}(i) + \frac{Cl_{visc}(\alpha_e(i)) - Cl_{inviscid}(i)}{Cl_\alpha}$
6: **end for**
7: Repeat Steps 1-6 until $|Cl_{visc} - Cl_{inviscid}| < \epsilon$

The modified load interpolation algorithm for the use of viscous forces obtained from this additional coupling procedure is detailed in algorithm 8, while the flowchart of the viscous coupling step by step procedure is presented in figure 5.3.

Algorithm 8 Viscous Coupling Algorithm - Load Interpolation

1: **for** every span-wise column of vortex rings j **do**

2: Obtain the vortex-column's viscous force, viscous moment and load application point

$$\vec{\mathbf{Ff}}_j = \vec{\mathbf{L}}_{\mathbf{visc}j} + \vec{\mathbf{D}}_{\mathbf{visc}j} \qquad \vec{\mathbf{Mf}}_j = \vec{\mathbf{M}}_{\mathbf{visc}j} \qquad \vec{\mathbf{p}}_{f_j} = \vec{\mathbf{p}}_{1/4} - \vec{\mathbf{dx}} + \frac{C_j \vec{\mathbf{x}}_j}{\|\vec{\mathbf{x}}_j\|}$$

3: Find the closest finite element

4: Obtain the rotation matrices between the deformed and undeformed nodes

$$\mathbf{R}_{\mathbf{n_k}} = R(\overset{\circlearrowleft}{q_k}') \qquad \mathbf{R}_{\mathbf{n_{k+1}}} = R(\overset{\circlearrowleft}{q_{k+1}}')$$

5: Project the fluid point $\vec{\mathbf{p}}_{f_{i,j}}$ onto the finite element

$$\vec{\mathbf{d}}_k = \vec{\mathbf{n_{k+1}}} - \vec{\mathbf{n_k}} \qquad \vec{\mathbf{p}_{f_{i,j}}}' = \frac{\vec{\mathbf{d}}_k}{\|\vec{\mathbf{d}}_k\|}(\vec{\mathbf{p}_{f_{i,j}}} \cdot \frac{\vec{\mathbf{d}}_k}{\|\vec{\mathbf{d}}_k\|}) \tag{5.12}$$

6: Find the fluid point's natural coordinates $\vec{\xi}_{\mathbf{i,j}}$ in that finite element

$$\xi_{i,j} = \frac{\|\vec{\mathbf{p}_{f_{i,j}}}'\|}{\|\vec{\mathbf{d}}_k\|} \tag{5.13}$$

7: Obtain the interpolation weight from the element's shape functions

$$w_{k,i,j} = N_k(\xi_{i,j}) = \xi_{i,j} \qquad w_{k+1,i,j} = N_{k+1}(\xi_{i,j}) = 1 - \xi_{i,j} \tag{5.14}$$

8: Obtain a weighed equivalent load at each receiving node that is rotated to remove deformation

$$\vec{\mathbf{r}}_{k,i,j} = \vec{\mathbf{p}_{f_{i,j}}} - \vec{\mathbf{n}}_k \tag{5.15}$$

$$\vec{\mathbf{r}}_{k+1,i,j} = \vec{\mathbf{p}_{f_{i,j}}} - \vec{\mathbf{n}}_{k+1} \tag{5.16}$$

$$\vec{\mathbf{Fs}}_{k,i,j} = w_{k,i,j} * \mathbf{R}_{\mathbf{n_k}}[\vec{\mathbf{Ff}}_{i,j} + (\vec{\mathbf{Mf}}_{i,j} \times \vec{\mathbf{r}}_{k,i,j})] \tag{5.17}$$

$$\vec{\mathbf{Fs}}_{k+1,i,j} = w_{k+1,i,j} * \mathbf{R}_{\mathbf{n_{k+1}}}[\vec{\mathbf{Ff}}_{i,j} + (\vec{\mathbf{Mf}}_{i,j} \times \vec{\mathbf{r}}_{k+1,i,j})] \tag{5.18}$$

$$\vec{\mathbf{Ms}}_{k,i,j} = w_{k,i,j} * \mathbf{R}_{\mathbf{n_k}}[(\vec{\mathbf{r}}_{k,i,j} \times \vec{\mathbf{Ff}}_{i,j}) + \vec{\mathbf{Mf}}_{i,j} - \vec{\mathbf{r}}_{k,i,j} \times (\vec{\mathbf{Mf}}_{i,j} \times \vec{\mathbf{r}}_{k,i,j})] \tag{5.19}$$

$$\vec{\mathbf{Ms}}_{k+1,i,j} = w_{k+1,i,j} * \mathbf{R}_{\mathbf{n_{k+1}}}[(\vec{\mathbf{r}}_{k+1,i,j} \times \vec{\mathbf{Ff}}_{i,j}) + \vec{\mathbf{Mf}}_{i,j} - \vec{\mathbf{r}}_{k+1,i,j} \times (\vec{\mathbf{Mf}}_{i,j} \times \vec{\mathbf{r}}_{k+1,i,j})] \tag{5.20}$$

9: **end for**

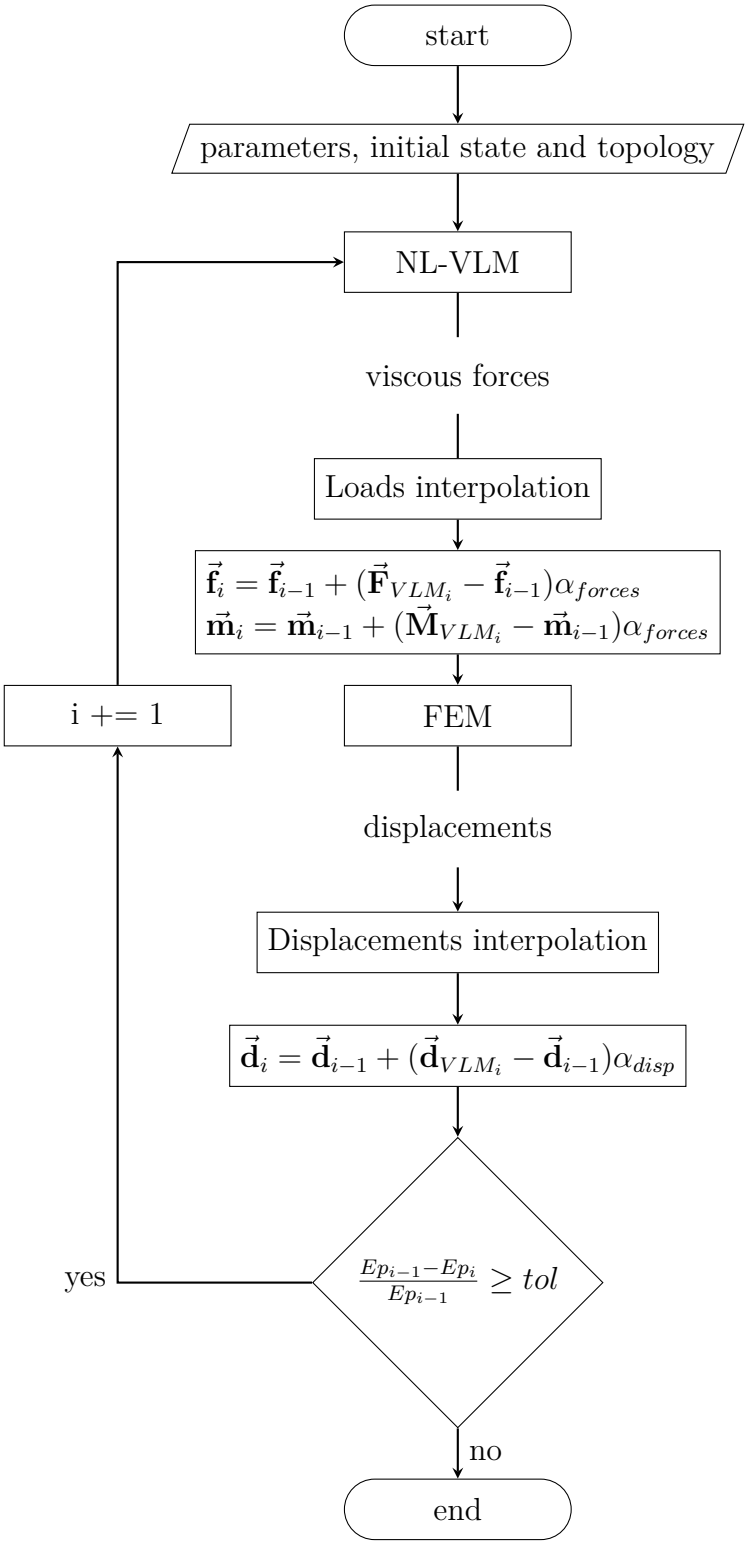

Figure 5.3 Viscous Coupling

5.3 Investigation of Smith's Wing

This case is repeated from the inviscid coupling with identical modeling, as a viscous, but subsonic verification case, providing an understanding of how the viscous computations impact the aeroelastic solution.

5.3.1 RANS Database

In order to use the viscous coupling algorithm, a single mesh was produced with NSGrid around a NACA0012 airfoil and ran within NSCode with a Reynolds number of 156920 and a Mach number of 0.084 with the Spalart-Allmaras turbulence model enabled. The computations ranging from an angle of attack of -5 to +10 degrees produce the two following Cl and Cm curves.

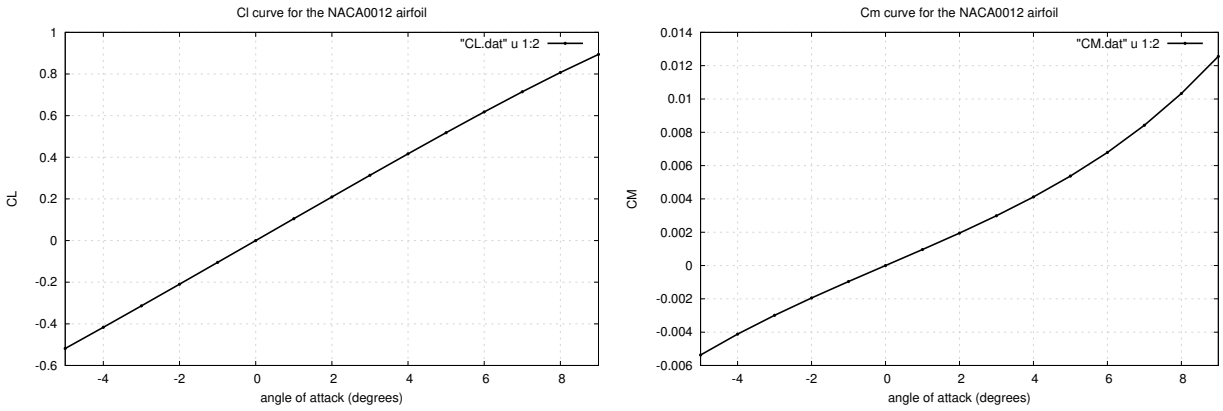

Figure 5.4 Viscous lift coefficient curve (left) and viscous moment coefficient curve (right)

5.3.2 Numerical Results

Viscous aeroelastic solutions were found using the coupling with the 2.5D NL-VLM with force following for both 2 and 4 degrees of alpha, the results of which can be seen in figures 5.5

It is apparent that the local angle of attack used for the coupling is modified by the deflection and twist of the wing, where the twist is almost entirely replicated in the local angle of attack increase.

For the angle of attack of 2 degrees, the deflections are overestimated by 4.7 %, while for 4 degrees, they are indistinguishable from the deflections obtained by Smith. However, the important factor is that the deflections have not changed dramatically from viscous to inviscid

computations, which is expected in the subsonic regime and demonstrates that the additional coupling methodology introduces no negative bias.

Once more, there are only significant discrepancies between the twist values obtained, which are of a small magnitude compared with the deflection.

5.3.3 Discussion

This analysis relays convincingly that the modification of the viscous coupling algorithm supports flexible wings and enables the use of the 2.5D NL-VLM in viscous cases. The modification of the local angle of attack is captured and taken into account during the viscous coupling phase of the NL-VLM, producing accurate results for this subsonic case.

It is important to note that the accuracy of the viscous computation is comparable to the inviscid computations, which do not share the additional computational cost of the viscous coupling. This suggests that the inviscid coupling is more attractive in the subsonic regime, whereas the viscous coupling can provide a more detailed pressure distribution.

Finally, the viscous data curves for this case are linear for these angles of attack and this case does not verify the robustness of the methodology with regards to nonlinearities in the viscous data.

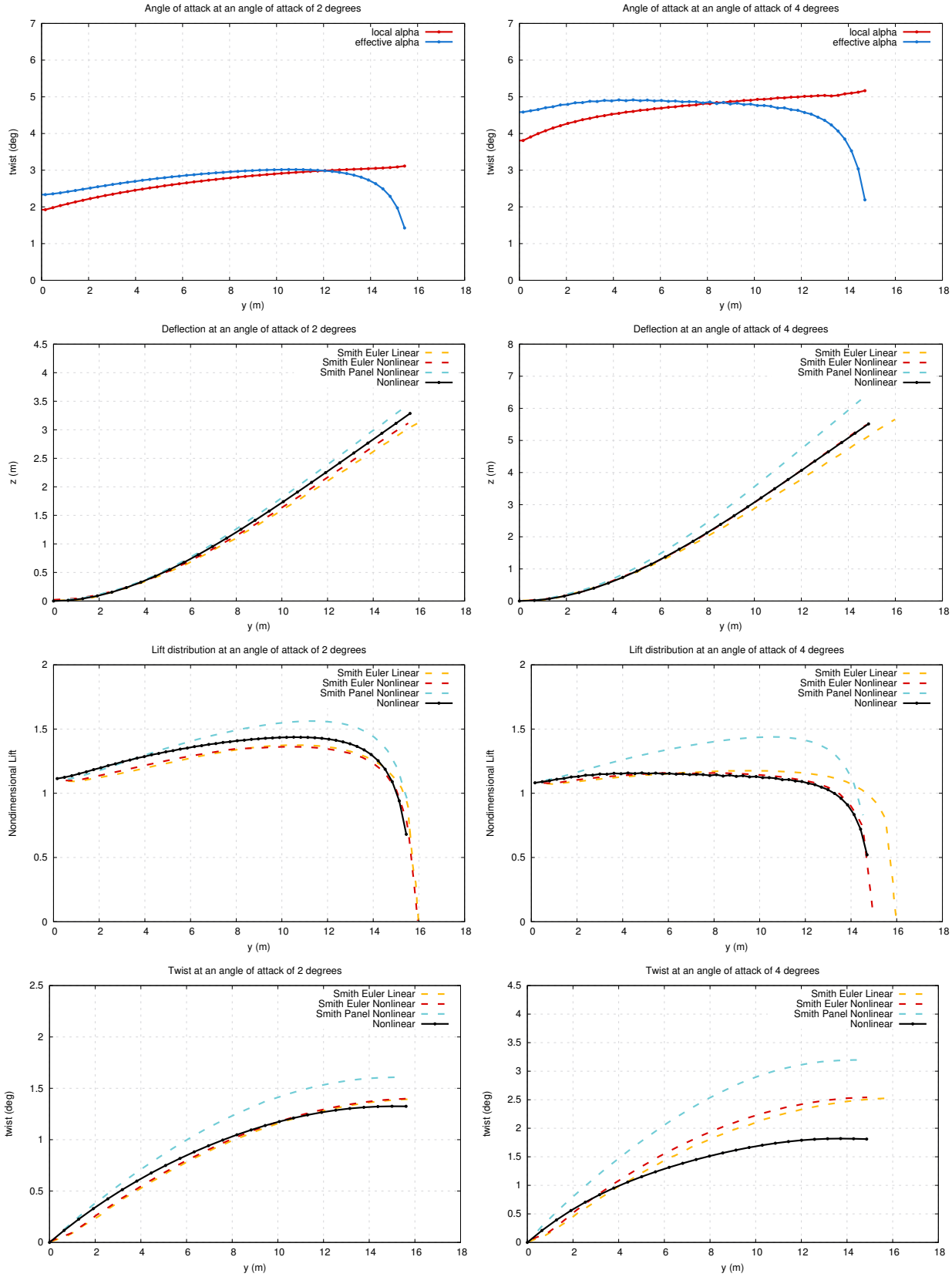

Figure 5.5 Smith wing viscous nonlinear aeroelastic solution for angles of attack of 2 and 4 degrees with 50 bar elements

5.4 Common Research Model Wind Tunnel Model Correction

The Common Research Model (figure 5.6) is a fictitious aircraft used to benchmark computational fluid mechanics software that has been studied in wind tunnels to provide experimental data (Vassberg *et al.*, 2008). An aeroelastic investigation was made by Keye and Brodersen (2014) to correct the wind tunnel data that was obtained for static aeroelastic effects.

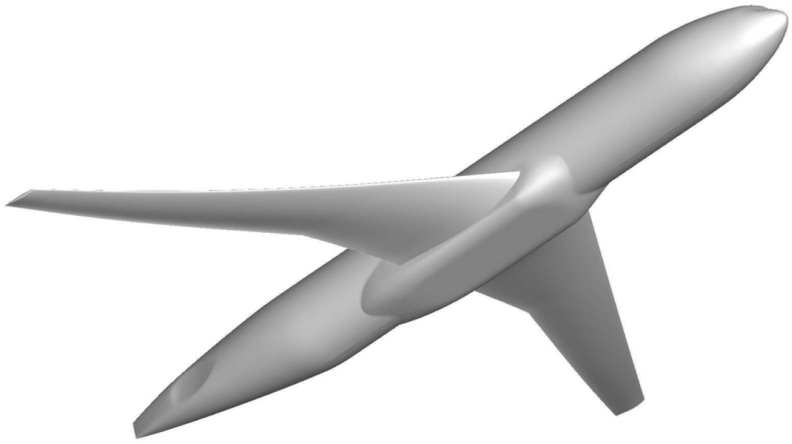

Figure 5.6 NASA Common Research Model without horizontal tail (Source: Vassberg *et al.* (2008))

It is of particular interest as it is designed to operate in the transonic regime, rendering it an approriate validation case for a static transonic aeroelastic solver.

The accuracy of the method is verified by comparing with 3D RANS results that were obtained by Keye and Brodersen (2014); Keye *et al.* (2013), and coupled with a volumetric FEM model to correct the Common Research Model Wind-Tunnel Model (CRM-WT) for the deflections that were experienced.

5.4.1 Numerical Results

The FEM beams are positioned at the elastic axis of the wings with appropriate section properties which are computed by taking spanwise cuts of the wing's structure perpendicular to the elastic axis. The polygons that are thus produced are fed into the following equations (Singer, 1993) to obtain the area A and first moments of inertia Q_y and Q_z, with material being added counter-clockwise and voids being added clockwise to produce the correct signs.

$$A = \frac{1}{2} \sum_{i=0}^{npts-1} (y_i + y_{i+1})(z_{i+1} - z_i) \tag{5.21}$$

$$Q_y = \frac{1}{2} \sum_{i=0}^{npts-1} (y_i - y_{i+1})(z_i z_{i+1} + \frac{1}{3}(z_i - z_{i+1})^2) \tag{5.22}$$

$$Q_z = \frac{1}{2} \sum_{i=0}^{npts-1} (z_{i+1} - z_i)(y_i y_{i+1} + \frac{1}{3}(y_i - y_{i+1})^2) \tag{5.23}$$

The first moments and the area are used to obtain the position of the section's centroid ($y_{centroid}$ and $z_{centroid}$), which is thereafter the origin from which the second moments of inertia I_{zz} and I_{yy} are computed, and serves as the position of the beam's elastic axis at the corresponding spanwise station.

$$y_{centroid} = \frac{Q_z}{A} \tag{5.24}$$

$$z_{centroid} = \frac{Q_y}{A} \tag{5.25}$$

$$I_{zz} = \frac{1}{12} \sum_{i=0}^{npts-1} (y_{i+1}^2 + y_{i+1} y_i + y_i^2)(y_i z_{i+1} - y_{i+1} z_i) \tag{5.26}$$

$$I_{yy} = \frac{1}{12} \sum_{i=0}^{npts-1} (z_{i+1}^2 + z_{i+1} z_i + z_i^2)(y_i z_{i+1} - y_{i+1} z_i) \tag{5.27}$$

This procedure automates the computation of section properties at as many span-stations as is desired. One of these sections is presented in figure 5.7 and the variation of the second moments of inertia for this wing are presented in figures 5.8 and 5.9.

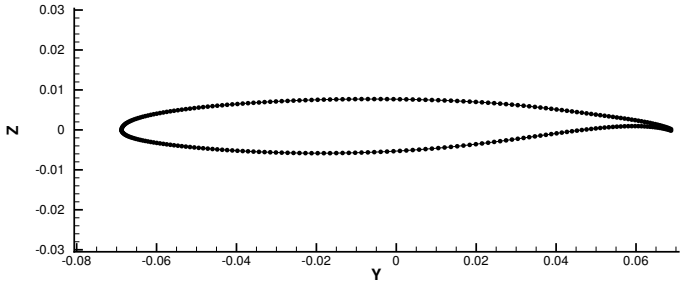

Figure 5.7 CRM-WT wing, beam section at $\eta = 0.53$ perpendicular to the elastic axis

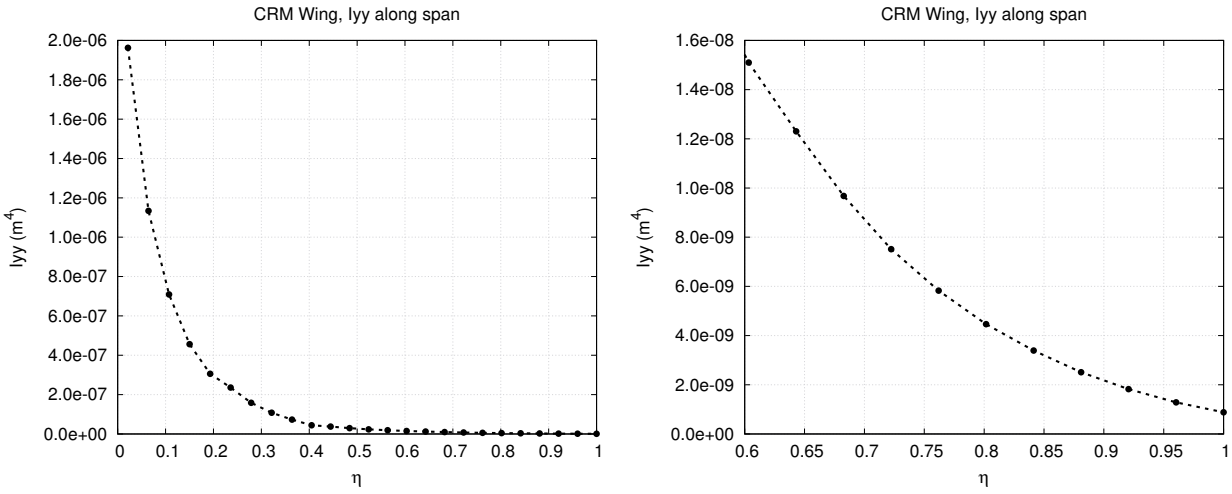

Figure 5.8 CRM-WT wing, I_{yy} of beam elements along the span (left) and close to tip (right)

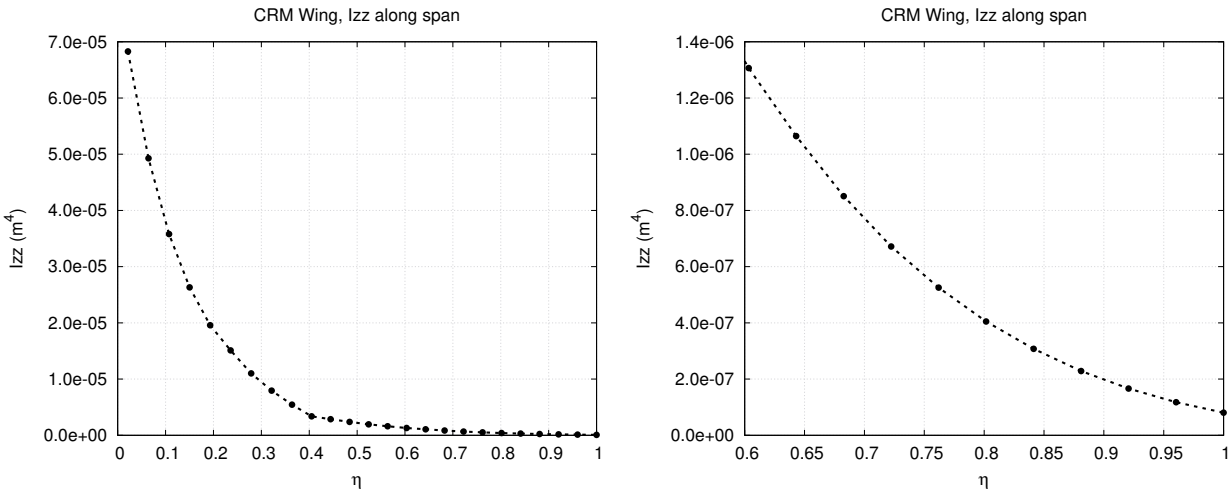

Figure 5.9 CRM-WT wing, I_{zz} of beam elements along the span (left) and close to tip (right)

The airflow is at a Mach number of 0.85, has a Reynolds number of 5e6 and the angle of attack used to compare deflections is 3 degrees. The database for this wing was computed using 9 individual spanwise stations and using the Spalart-Allmaras turbulence model. It was chosen to neglect cable routes, as they were positioned near the neutral axis and would have a small effect on the section structural properties.

A grid of panels of 44 by 4 was used for the VLM (figure 5.10) coupled with a FEM model consisting of 50 bars (figure 5.11) and the FEM node which is positioned at the root of the wing is fixed. The portion of the wing which is normally inside the fuselage is modeled in the VLM grid, but only the forces from wet panels are sent to the FEM model in the coupling procedure.

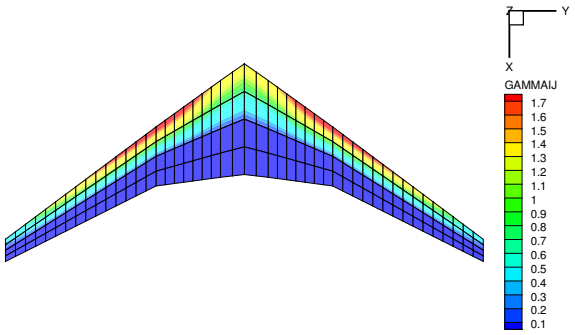

Figure 5.10 44x4 VLM mesh overlayed with the Γ distribution at $\alpha = 3.0$ °

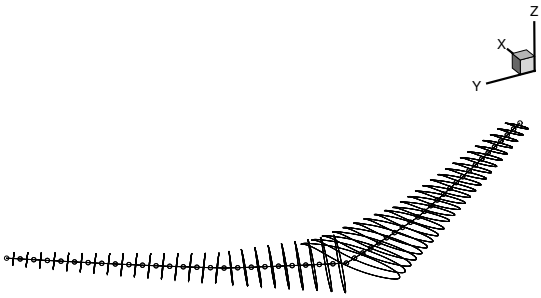

Figure 5.11 FEM model consisting of 50 beams with sections overlayed mid-beam

Lift versus angle of attack is presented in figure 5.12, the corresponding lift distributions in figure 5.13, the deformation in figures 5.14 and 5.15, and the pressure distributions in figures 5.16 for nondimensional spanwise positions η of 0.502, 0.727 and 0.950.

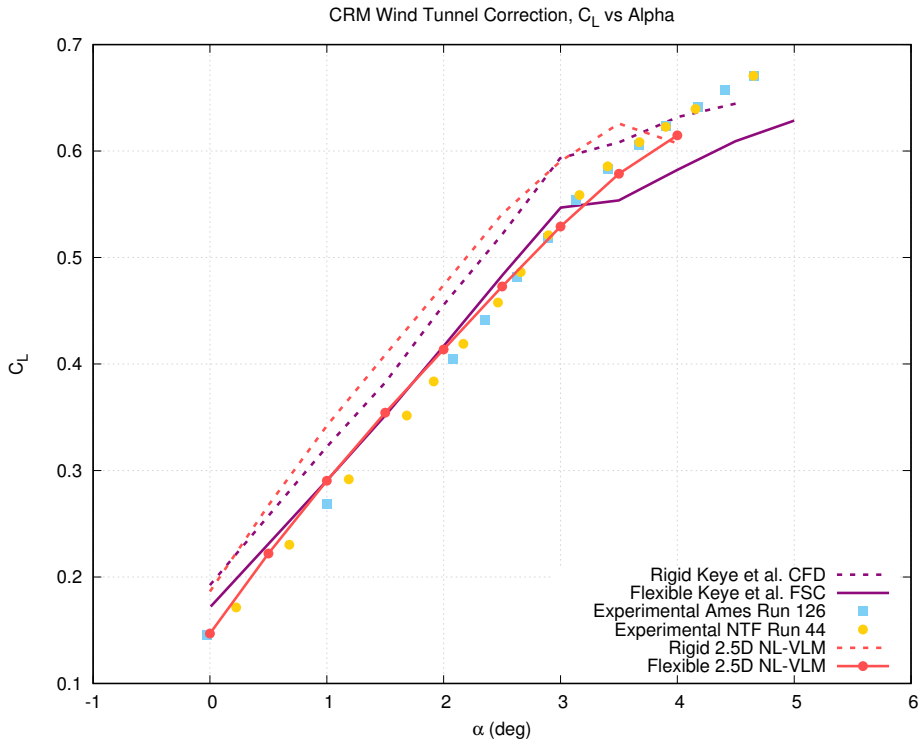

Figure 5.12 Lift coefficient vs angle of attack for the CRM-WT wing

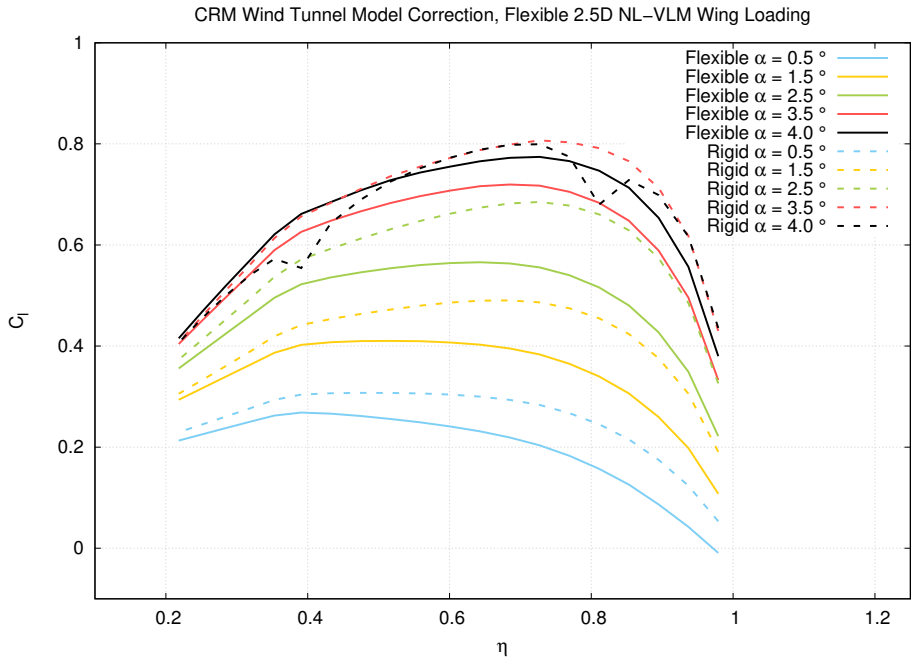

Figure 5.13 Wing loading vs angle of attack for the CRM-WT wing

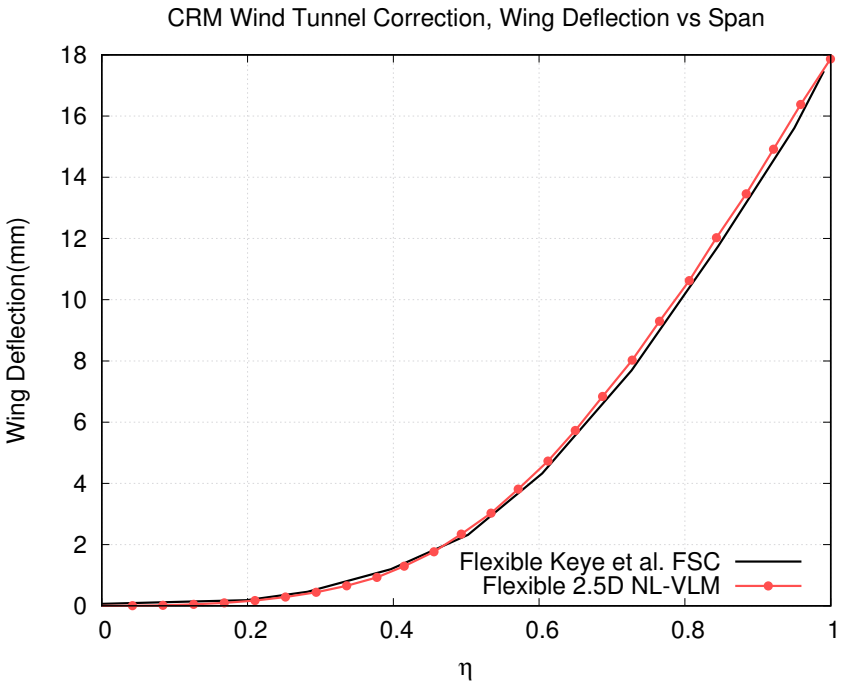

Figure 5.14 Deflections vs span for the CRM-WT wing at $\alpha = 3.0$ °

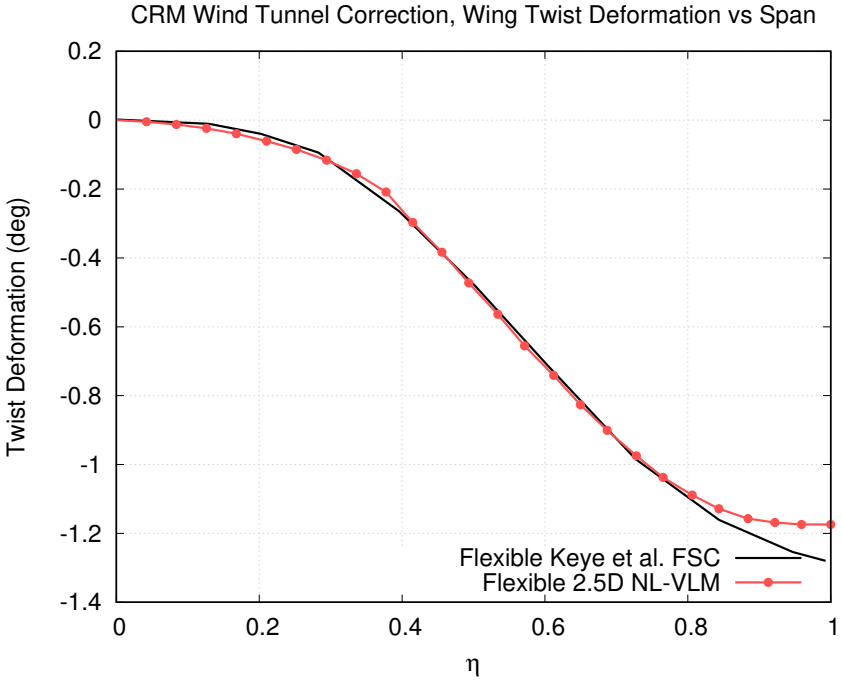

Figure 5.15 Twist deformation vs span for the CRM-WT wing at $\alpha = 3.0$ °

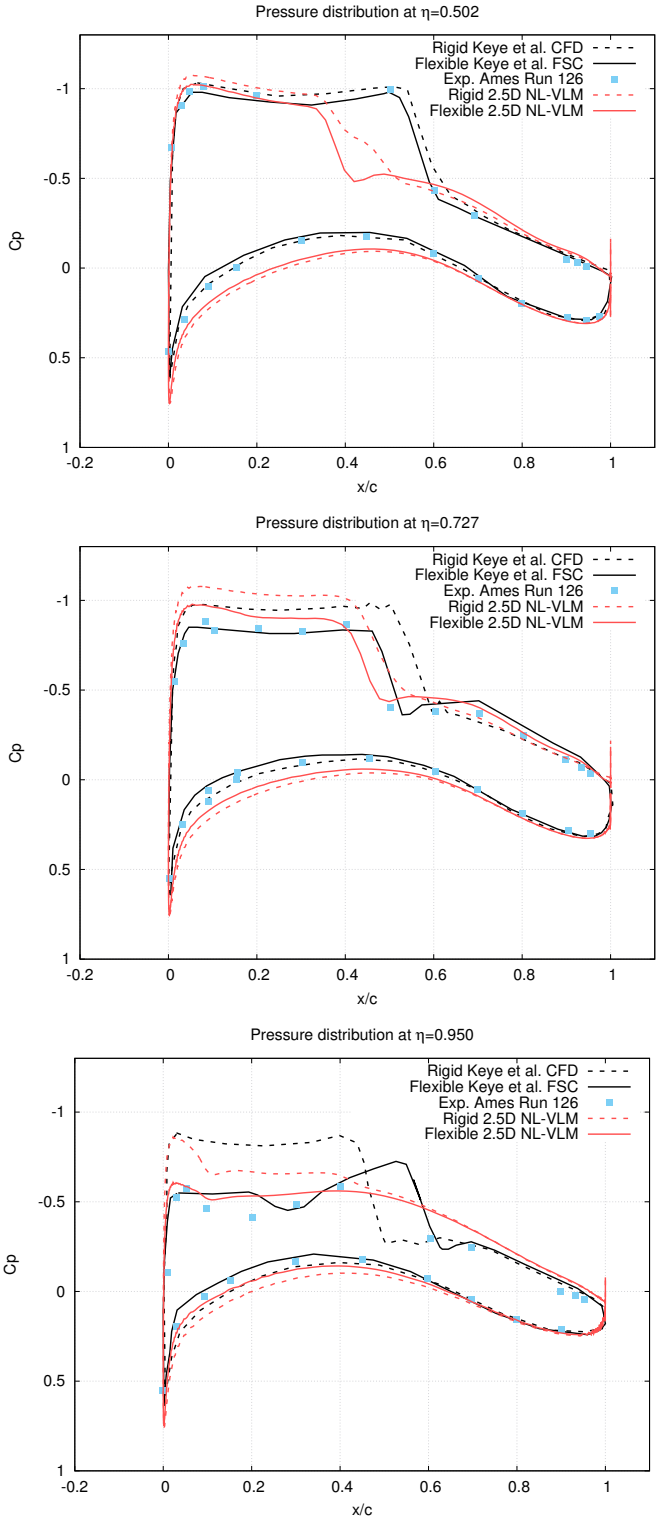

Figure 5.16 CRM-WT, Pressure distribution at $\eta = 0.502$ (top), $\eta = 0.727$ (middle) and $\eta = 0.950$ (bottom) at $\alpha = 3.0$ °

5.4.2 Discussion

To validate the inclusion of the viscous coupling, a comparison of the C_L vs α curve for the wind tunnel model of the Common Research Model is presented (Keye and Brodersen, 2014; Keye *et al.*, 2013). It demonstrates that the deflection and twist experienced by the wing in the transonic flight regime reduce the overall lift that is generated for a given angle of attack.

It can be observed in figure 5.12, that the deviation of the lift coefficient provided by the NL-VLM is in good agreement with the more computationally expensive 3D CFD method used by Keye and Brodersen (2014); Keye *et al.* (2013) for angles of attack lower than three degrees. We note the capability of the NL-VLM procedure to capture near-$C_{L_{max}}$ effects via the 2.5D CFD solutions. As anticipated, the $C_{L_{max}}$ is influenced by turbulence modeling Rumsey *et al.* (2011), and several other factors, including transitional effects can account for the discrepancies observed in this region of the curve.

At an angle of attack of 3.5 degrees, it can be observed that the rigid NL-VLM has attained its $C_{L_{max}}$, while the flexible NL-VLM hasn't yet, which suggests that the wing's flexibility has delayed the onset of stall to a higher angle of attack due to the negative twist that is incurred. This is corroborated by figures 5.15 and 5.13 where it can be observed that the flexibility of the wing causes significant washout. As a result, the wing loading is reduced and shifted inboard. These results are consistent with typical aeroelastic effects on flexible aircraft wings.

Figures 5.14 and 5.15 show good agreement with the higher fidelity methods used by Keye and Brodersen (2014); Keye *et al.* (2013) for up to 80% of the span, whereas there is a significant discrepancy for the twist at the tip of the wing, which is indicative of differences with the wing loading experienced by the two methods near the wing tip. It is interesting to note that while both rigid methods experience a dip in C_L when nearing 3 degrees, the 2.5D NL-VLM does not experience any stall in the flexible case, which can be potentially explained by differences in turbulence modeling. Figure 5.16 presents the pressure distribution at three spanwise stations and compares them with the results obtained by Keye and Brodersen (2014); Keye *et al.* (2013), as well as experimental data. It can be observed that the difference in amplitude between rigid and flexible 2.5D NL-VLM is similar to the difference in amplitude observed by Keye and Brodersen (2014); Keye *et al.* (2013). However, the presence and position of the shock differs, a discrepancy that was observed by Gallay and Laurendeau (2016) for the CRM. Furthermore, at span station $\eta = 0.727$, where the loading is roughly maximum according to figure 5.13, the pressure distribution obtained by the present method is in good agreement with the experimental data.

CHAPTER 6 CONCLUSION

6.1 Synthesis of Work

The goal of this research project was to develop a static aeroelastic methodology suitable for the conceptual and preliminary design of aircraft having low or high structural flexibility and operating in both subsonic and transonic flight regimes.

An aeroelastic framework was developed that combines the vortex lattice method with the finite element method. The accuracy of the finite element solver for high deflection cases was demonstrated for both steady and unsteady cases comprising large deflections.

A segregated static aeroelastic solver was developed in C++ and Python that couples the vortex lattice method with a nonlinear finite element method. The aerodynamic forces of the VLM and the displacements of the FEM were transferred using interpolation algorithms and the procedure obtained an equilibrium static solution through iteration of this procedure until the fluid, solid and boundary all attained convergence, thereby eliminating any further exchange of energy between the fluid and the solid.

The accuracy of the method was assessed in the subsonic regime by comparing it with established tools. It was found that the deflections and span loads compared very well with previously published material (Smith *et al.*, 2001).

A segregated static aeroelastic solver was developed in C++ and Python that couples the vortex lattice method with a nonlinear finite element method and with 2.5D RANS sectional data. The aerodynamic forces transfered to the structure were obtained from the 2.5D RANS flow field instead of the vortex lattice model itself in order to transfer the correct loads in the transonic regime. This additional viscous coupling procedure occurs within the VLM C++ code and does not affect the rest of the aeroelastic coupling procedure.

The accuracy of the method was assessed in the subsonic and transonic regimes by comparing it with established tools. The addition of the viscous coupling did not alter the deflections significantly for the subsonic case. The transonic case that was studied was the wind tunnel model correction for the Common Research Model that was done by Keye and Brodersen (2014) using 3D RANS with a 3D volumetric FEM. It was found that despite the use of a stick model, the methodology produced very accurate deflection results and the pressure distributions that were obtained were competitive with those obtained by Keye.

6.2 Limitations of the Proposed Solution

An important assumption that has held for the entirety of the work is that airfoil shape is maintained. This assumption enables the use of a pre-computed 2.5D RANS database for sectional data and makes the use of a beam model appropriate. If that assumption doesn't hold, a significant inconvenience arises in having to compute the 2.5D RANS data in real time.

A limitation that was encountered in the transonic case that was studied is the difference of wing tip effects between the VLM and the 3D RANS. This was found to produce very different wing tip twist and the ambiguity that this provides is potentially inappropriate for the preliminary design phase, but possibly still acceptable for conceptual design phase.

The most important limitation of the method is the lack of fuselage interaction effects. This might not be an obstacle for aeroelasticity, since the load produced near the fuselage was found to have little effect on the overall deflections of the wing in the case of the CRM.

6.3 Future Work

Three ideas are proposed for future research :

1. An unsteady variant of the 2.5D nonlinear vortex-lattice method could be coupled with the unsteady or nonlinear unsteady finite element method in order to study dynamic aeroelasticity, which could possibly provide insight into the effects of viscosity on dynamic aeroelasticity, especially in the transonic regime.

2. The assumption of rigid airfoils could possibly be removed if the 2.5D RANS database is recomputed at each iteration of the aeroelastic coupling algorithm. However, one would have to couple it with a panel method instead of using a VLM in order to couple volumetric or shell FEM surface deformations with the aerodynamic model.

3. The limitations imposed by the lack of fuselage interaction could possibly be overcome by using a panel method to model the fuselage as was done by Mauermann (2010). The coupling algorithm that augments the linear potential method with 2.5D RANS sectional data would have to be altered in order to accommodate the use of a panel method instead of a VLM.

REFERENCES

ABDO, M., PIPERNI, P., and KAFYEKE, F., "Optimization of a business jet," in *Annual General Meeting, Aircraft Design and Development Symposium*, Toronto, Ontario, April 2005.

ACAR, P. and NIKBAY, M., "Steady and unsteady aeroelastic computations of hirenasd wing for low and high reynolds numbers," in *Proceedings of the 54th AIAA/ASME/ASCE/AHS/ASC structures, structural dynamics, and materials conference*, 2013, pp. 8–11.

ALBANO, E. and RODDEN, W. P., "A doublet-lattice method for calculating lift distributions on oscillating surfaces in subsonic flows," *AIAA journal*, vol. 7, no. 2, pp. 279–285, 1969.

ANDERSON, J., *Fundamentals of Aerodynamics*. McGraw-Hill Higher Education, 2001.

BECKERT, A. and WENDLAND, H., "Multivariate interpolation for fluid-structure-interaction problems using radial basis functions," *Aerospace Science and Technology*, vol. 5, no. 2, 2001.

BIJL, H., VAN ZUIJLEN, A., and BOSSCHER, S., "Two level algorithms for partitioned fluid-structure interaction computations," in *European Conference on Computational Fluid Dynamics*, 2006.

BISPLINGHOFF, R., ASHLEY, H., and HALFMAN, R., *Aeroelasticity*. Dover Publications inc., 1996.

BOURGAULT-CÔTÉ, S., GHASEMI, S., MOSAHEBI, A., and LAURENDEAU, É., "Extension of a two-dimensional navier–stokes solver for infinite swept flow," *AIAA Journal*, 2017.

BRUHN, E., *Analysis and Design of Flight Vehicle Structures*. S.R. Jacobs and Associates inc., 1973.

CATTARIUS, J., "Numerical wing/store interaction analysis of a parametric f16 wing," Ph.D. dissertation, 1999.

CESNIK, C., SENATORE, P., WEIHUA, S., and ATKINS, E., "X-hale: A very flexible uav for nonlinear aeroelastic tests," in *51st AIAA/ASME/ASCE/AHS/ASC Structures, Structural Dynamics, and Materials Conference
*, Orlando, Florida, April 2010.

CHWALOWSKI, P., FLORANCE, J., HEEG, J., WIESEMAN, C., and PERRY, B., "Preliminary computational analysis of the hirenasd configuration in preparation for the aeroelastic prediction workshop," in *IFASD-2011-International Forum of Aeroelasticity*, Paris, France, June 2011.

CLOUGH, R. W., "The finite element method in plane stress analysis," 1960.

COLLAR, A., "The expanding domain of aeroelasticity," *The Royal Aeronautical Society*, vol. 50, no. 428, pp. 613–636, 1946.

COOK, R., MALKUS, D., PLESHA, M., and WITT, R., *Concepts and Applications of Finite Element Analysis*. McGraw-Hill, 2002.

COURANT, R., "Variational methods for the solution of problems of equilibrium and vibrations," *Bulletin of the American mathematical Society*, vol. 49, no. 1, pp. 1–23, 1943.

DE BOER, A., VAN ZUIJLEN, A., and BIJL, H., "Comparison of the conservative and a consistent approach for the coupling of non-matching meshes," in *European Conference on Computational Fluid Dynamics*, 2006.

DE BOER, A., VAN ZUIJLEN, A., and BIJL, H., "Review of coupling methods for non-matching meshes," *Computer Methods in Applied Mechanics and Engineering*, vol. 196, no. 1, 2007.

DEBLOIS, A. and ABDO, M., "Multi-fidelity multidisciplinary design optimization of metallic composite regional and business jets," in *13th AIAA/ISSMO Multidisciplinary Analysis Optimization Conference*, Fort Worth, Texas, September 2010.

DRELA, M., "Integrated simulation model for preliminary aerodynamic, structural, and control-law design of aircraft," *AIAA Paper*, vol. 99, p. 1394, 1999.

DUBOIS, H., *The magnetic circuit in theory and practice*. Longmans, 1896.

FARHAT, C. and LESOINNE, M., "Two efficient staggered algorithms for the serial and parallel solution of three-dimensional nonlinear transient aeroelastic problems," *Computer Methods in Applied Mechanics and Engineering*, vol. 182, no. 3, 2000.

FARHAT, C., LESOINNE, M., and LETALLEC, P., "Load and motion transfer algorithms for fluid structure interaction problems with non-matching discrete interfaces," *Computer Methods in Applied Mechanics and Engineering*, vol. 95, no. 114, 1998.

FARHAT, C., PIERSON, K., and DEGAND, C., "Multidisciplinary simulation of the maneuvering of an aircraft," *Engineering with Computers*, vol. 17, no. 1, pp. 16–27, 2001.

FOTOUHI, R., "Dynamic analysis of very flexible beams," *Journal of Sound and Vibration*, vol. 305, no. 3, pp. 521–533, 2007.

FUNG, Y., *An Introduction to the Theory of Aeroelasticity*. Dover Publications inc., 1993.

GALERKIN, B. G., "Series solution of some problems of elastic equilibrium of rods and plates," *Vestn. Inzh. Tekh*, vol. 19, pp. 897–908, 1915.

GALLAY, S. and LAURENDEAU, E., "Preliminary design aerodynamic model for complex configurations using lifting line coupling algorithm," *Journal Aircraftl*, vol. 53, no. 4, 2016.

GALLAY, S., GHASEMI, S., and LAURENDEAU, E., "Sweep effects on non-linear lifting line theory near stall," in *52nd Aerospace Sciences Meeting*. National Harbor, Maryland: AIAA, 2014, pp. 1105–1124.

GARCIA, J. A., "Numerical investigation of nonlinear aeroelastic effects on flexible high-aspect-ratio wings," *Journal of Aircraft*, vol. 42, no. 4, pp. 1025–1036, 2005.

GERADIN, M. and CARDONA, A., "Kinematics and dynamics of rigid and flexible mechanisms using finite elements and quaternion algebra," *Computational Mechanics*, vol. 4, no. 2, pp. 115–135, 1988.

GEUZAINE, P., BROWN, G., HARRIS, C., and FARHAT, C., "Aeroelastic dynamic analysis of a full f-16 configuration for various flight conditions," *AIAA journal*, vol. 41, no. 3, pp. 363–371, 2003.

GROZDANOV, A. and LAURENDEAU, E., "Transonic aeroelasticity using the 2.5D nonlinear vortex-lattice method," in *IFASD 2017*, 2017.

HALL, B. D., "Numerical simulations of the aeroelastic response of an actively controlled flexible wing," 1999.

HASANZADEH, K., LAURENDEAU, E., and PARASCHIVOIU, I., "Grid-generation algorithms for complex glaze-ice shapes reynolds-averaged navier–stokes simulations," *AIAA Journal*, vol. 54, no. 3, pp. 847–860, 2016.

HOOKE, R., *Lectures de potentia restitutiva, or of spring explaining the power of springing bodies*. Royal Society at the Bell in Saint-Paul's Church-Yard, 1678.

HOUNJET, M. and MEIJER, J., "Evaluation of elastomechanical and aerodynamic data transfer methods for non- planar configurations in computational aeroelastic analysis," in *the International Forum on Aeroelasticity and Structural Dynamics 1995*, Manchester, United Kingdom, June 1995.

HSIAO, K., "Corotational total lagrangian formulation for three-dimensional beam element," *AIAA Journal*, vol. 30, 1992.

HSIAO, K. and TSAY, C., "A motion process for large displacement analysis of spatial frames," *International Journal of Space Structures*, vol. 6, 1990.

HSIAO, K., HORNG, H.-J., and CHEN, Y.-R., "A corotational procedure that handles large rotations of spatial beam structures," *Computers and Structures*, vol. 27, 1987.

HSIAO, K., LIN, J., and LIN, W., "A consistent co-rotational finite element formulation for geometrically nonlinear dynamic analysis of 3-d beams," *Computer Methods in applied Mechanics and engineering*, vol. 169, pp. 1–18, 1999.

HUBNER, B., WALHORN, E., and DINKLER, D., "A monolithic approach to fluid–structure interaction using space–time finite elements," *Computer Methods in Applied Mechanics and Engineering*, vol. 193, no. 23, 2004.

HUGHES, T. J., "Analysis of transient algorithms with particular reference to stability behavior," *Computational methods for transient analysis(A 84-29160 12-64). Amsterdam, North-Holland, 1983,*, pp. 67–155, 1983.

HULBERT, G. and HUGHES, T., "An error analysis of truncated starting conditions in step-by-step time integration: Consequences for structural dynamics," *Earthquake engineering & structural dynamics*, vol. 15, no. 7, pp. 901–910, 1987.

JAMESON, A., *Encyclopedia of Computational Mechanics*. John Wiley & Sons Ltd., 2004, vol. 3.

JOUKOWSKY, N., "Über die konturen der tragflächen der drachenflieger," *Zeit. für Flugtechnik und Motorluftschiffahrt*, vol. 1, pp. 281–284, 1910.

KATZ, J. and PLOTKIN, A., *Low-Speed aerodynamics*. Cambridge University Press, 1991.

KEYE, S. and BRODERSEN, O., "Investigation of aeroelastic effects on the nasa common research model," *Journal of Aircraft*, vol. 51, no. 4, pp. 1323–1330, 2014.

KEYE, S., TOGITI, V., EISFELD, B., BRODERSEN, O., and RIVERS, M. B., "Investigation of fluid-structure-coupling and turbulence model effects on the dlr results of the fifth aiaa cfd drag prediction workshop," *AIAA Paper*, vol. 2509, p. 2013, 2013.

KUNDU, A., *Aircraft Design*. Cambridge University Press, 2010.

KUTTA, W., "Auftriebskräfte in strömenden flüssigkeiten," *Illustrierte Aeronautische Mitteilungen*, vol. 6, no. 133, pp. 133–135, 1902.

LEVESQUE, A. T., PIGEON, A., DELOZE, T., and LAURENDEAU, E., "An overset grid 2d/infinite swept wing urans solver using recursive cartesian virtual grid method," in *53RD AIAA AEROSPACE SCIENCES MEETING*, 2015, aIAA Paper 2015–0912.

MAMAN, N. and FARHAT, C., "Matching fluid and structure meshes for aeroelastic computations: a parallel approach," *Computers & Structures*, vol. 54, no. 4, pp. 779–785, 1995.

MAUERMANN, T., "Flexible aircraft modelling for flight loads analysis of wake vortex encounters," Deutsches Zentrum fur Luft-und-Raumfahrt, Tech. Rep., 2010.

MAUTE, K., NIKBAY, M., and FARHAT, C., "Coupled analytical sensitivity analysis and optimization of three-dimensional nonlinear aeroelastic systems," *AIAA journal*, vol. 39, no. 11, pp. 2051–2061, 2001.

MSC, *Getting Started with MD Nastran User's Guide*. MacNeal-Schwendler Corporation, 2010.

MURUA, J., PALACIOS, R., and GRAHAM, J., "Applications of the unsteady vortex-lattice method in aircraft aeroelasticity and flight dynamics," *Progress in Aerospace Sciences*, vol. 46, no. 72, 2012.

NEWMARK, N. M., "A method of computation for structural dynamics," *Journal of the engineering mechanics division*, vol. 85, no. 3, pp. 67–94, 1959.

NIU, M., *Airframe Stress Analysis and Sizing*. Hong Kong Conmilit Press ltd., 1997.

PACHECO, P., *An introduction to parallel Programming*. Elsevier Inc., 2011.

PARENTEAU, M., "Aerodynamic optimization of aircraft wings using a coupled vlm-2.5d rans approach," Master's thesis, Polytechnique Montreal, QC, CANADA, 2016.

PATIL, M. J. and HODGES, D. H., "On the importance of aerodynamic and structural geometrical nonlinearities in aeroelastic behavior of high-aspect-ratio wings," *Journal of Fluids and Structures*, vol. 19, no. 7, pp. 905–915, 2004.

PIPERNI, P. and DEBLOIS, A., "Development of a multilevel multidisciplinary- optimization capability for an industrial environment," *AIAA Journal*, vol. 51, no. 10, October 2013.

PIPERNO, S. and FARHAT, C., "Partitioned procedures for the transient solution of coupled aeroelastic problems," *Computer Methods in Applied Mechanics and Engineering*, vol. 190, no. 24, 2001.

PRAGER, W. and SYNGE, J. L., "Approximations in elasticity based on the concept of function space," *Quarterly of Applied Mathematics*, vol. 5, no. 3, pp. 241–269, 1947.

PRANANTA, B. *et al.*, "Transonic unsteady aerodynamic analysis of hirenasd wing oscillating in flexible modes," *Contribution to AIAA Aeroelastic Workshop I*, 2012.

PRANDTL, L., "Applications of modern hydrodynamics to aeronautics," 1923.

RAVEH, D., KARPEL, M., and YANIV, S., "Nonlinear design loads for maneuvering elastic aircraft," *Journal of aircraft*, vol. 37, no. 2, pp. 313–318, 2000.

RAYLEIGH, J. W. S. B. and SPOTTISWOODE, W., *On the theory of resonance*, 1871.

REDDY, J. N., *An Introduction to the Finite Element Method*. McGraw-Hill, 2006.

REDDY, J. N., *An Introduction to Nonlinear Finite Element Analysis*. Oxford University Press, 2014.

RITZ, W., "Über eine neue methode zur lösung gewisser variationsprobleme der mathematischen physik." *Journal für die reine und angewandte Mathematik*, vol. 135, pp. 1–61, 1909.

RIZZI, A., "Modeling and simulating aircraft stability and control—the simsac project," *Progress in Aerospace Sciences*, vol. 47, no. 8, pp. 573–588, 2011.

RUMSEY, C. L., LONG, M., STUEVER, R. A., and WAYMAN, T. R., "Summary of the first aiaa cfd high-lift prediction workshop," *Journal of Aircraft*, vol. 48, no. 6, pp. 2068–2082, 2011.

SCHUSTER, D. M., CHWALOWSKI, P., HEEG, J., and WIESEMAN, C. D., "A summary of data and findings from the first aeroelastic prediction workshop," in *Seventh International Conference on Computational Fluid Dynamics (ICCFD7)*, Big island, Hawaii, July 2012.

SCHUSTER, D. M., HEEG, J., WIESEMAN, C. D., and CHWALOWSKI, P., "Analysis of test case computations and experiments for the first aeroelastic prediction workshop," 2013.

SIEMENS, *NX Nastran Handbook of Nonlinear Analysis*. Siemens, 2014.

SINGER, M., "A general approach to moment calculation for polygons and line segments," *Pattern Recognition*, vol. 26, no. 7, pp. 1019–1028, 1993.

SMITH, M. J., PATIL, M. J., and HODGES, D. H., "Cfd-based analysis of nonlinear aeroelastic behavior of high-aspect ratio wings," *AIAA Paper*, vol. 1582, p. 2001, 2001.

SOUTHWELL, R. V., "Stress-calculation in frameworks by the method of" systematic relaxation of constraints". i and ii," *Proceedings of the Royal Society of London. Series A, Mathematical and Physical Sciences*, vol. 151, no. 872, pp. 56–95, 1935.

TIMOSHENKO, S., *Theory of Elasticity*. McGraw-Hill Book Company Inc., 1951.

TING, E., NGUYEN, N., and TRINH, K., "Static aeroelastic and longitudinal trim model of flexible wing aircraft using finite-element vortex-lattice coupled solution," *AIAA Paper*, vol. 837, 2014.

TURNER, M. J., "Stiffness and deflection analysis of complex structures," *journal of the Aeronautical Sciences*, 1956.

VAN DAM, C., "The aerodynamic design of multi-element high-lift systems for transport airplanes," *Progress in Aerospace Sciences*, vol. 38, no. 2, pp. 1775–1779, 2002.

VAN SCHOOR, M. C. and VON FLOTOW, A. H., "Aeroelastic characteristics of a highly flexible aircraft," *Journal of Aircraft*, vol. 27, no. 10, pp. 901–908, 1990.

VAN ZUIJLEN, A. and BIJL, H., "Implicit and explicit higher order time integration schemes for structural dynamics and fluid-structure interaction computations," *Computers and Structures*, vol. 83, no. 2, 2005.

VASSBERG, J. C., DEHAAN, M. A., RIVERS, S. M., and WAHLS, R. A., "Development of a common research model for applied cfd validation studies," *AIAA paper*, vol. 6919, p. 2008, 2008.

VERSTEEG, H. K. and MALALASEKERA, W., *An introduction to computational fluid dynamics: the finite volume method*. Pearson Education, 2007.

VINCE, J., *Quaternions for Computer Graphics*. Springer Verlag, 2011.

WALHORNE., H. B. and DINKLER, D., "Fluid–structure coupling within a monolithic model involving free surface flows," *Computers and Structures*, vol. 83, no. 25, 2005.

WANG, Z., CHEN, P., LIU, D., MOOK, D., and PATIL, M., "Time domain nonlinear aeroelastic analysis for hale wings," *AIAA paper*, vol. 1640, p. 2006, 2006.

WRIGHT, J. and COOPER, J., *Introduction to Aircraft Aeroelasticity and Loads*. John Wiley & Sons Ltd., 2007.

YOUNG, W. and BUDYNAS, R., *Roark's Formuas for Stress and Strain*. S.R. Jacobs and Associates inc., 1989.

ZIENKIEWICZ, O. and TAYLOR, R., *The Finite Element Method*. McGraw-Hill, 2000.

ZIENKIEWICZ, O. C. and CHEUNG, Y. K., "The finite element method for analysis of elastic isotropic and orthotropic slabs." *Proceedings of the Institution of Civil Engineers*, vol. 28, no. 4, pp. 471–488, 1964.